

General Disclaimer

One or more of the Following Statements may affect this Document

- This document has been reproduced from the best copy furnished by the organizational source. It is being released in the interest of making available as much information as possible.
- This document may contain data, which exceeds the sheet parameters. It was furnished in this condition by the organizational source and is the best copy available.
- This document may contain tone-on-tone or color graphs, charts and/or pictures, which have been reproduced in black and white.
- This document is paginated as submitted by the original source.
- Portions of this document are not fully legible due to the historical nature of some of the material. However, it is the best reproduction available from the original submission.

Tmx-71353

REMOTE SENSING OF THE ATMOSPHERE FROM ENVIRONMENTAL SATELLITES

LEWIS J. ALLISON
RAYMOND WEXLER
CHARLES R. LAUGHLIN
WILLIAM R. BANDEEN

JUNE 1977

(NASA-TM-X-71353) REMOTE SENSING OF THE
ATMOSPHERE FROM ENVIRONMENTAL SATELLITES
(NASA) 124 p HC A06/MF A01 CSCL 04A

N77-27484

G3/43 Unclass
39022

GSFC

— GODDARD SPACE FLIGHT CENTER —
GREENBELT, MARYLAND

REMOTE SENSING OF THE ATMOSPHERE FROM
ENVIRONMENTAL SATELLITES

Lewis J. Allison
Raymond Wexler
Charles R. Laughlin
William R. Bandeen

GODDARD SPACE FLIGHT CENTER
Greenbelt, Maryland 20771


REMOTE SENSING OF THE ATMOSPHERE FROM ENVIRONMENTAL SATELLITES

Lewis J. Allison
Raymond Wexler
Charles R. Laughlin
William R. Bandeen

Goddard Space Flight Center
Greenbelt, Maryland 20771

ABSTRACT

The use of satellites for the remote sensing of the earth and its atmosphere is reviewed. Meteorological satellites have been in use since 1960. The polar orbiting satellites at 650 to 1500 km make 12 to 14 orbits daily with near full earth coverage. The geosynchronous satellites at 36,000 km remain approximately fixed in space relative to the earth and view the same area continuously.

 Cameras obtaining earth images in the visible, detect clouds and monitor storm systems. Infrared radiometers measure temperatures of the surface or cloud tops and also determine amounts of ozone and water vapor in the atmosphere. Radiometers sensitive to different spectral regions in absorption bands (such as CO₂ at

15 μm and 4.3 μm) are used to determine atmospheric vertical temperatures profiles.

The earth's radiation budget is determined from satellite measurements of the reflected solar radiation and the emitted long wave terrestrial radiation.

Atmospheric winds are obtained by cloud tracking from geosynchronous satellites. A major problem is height determination. Infrared "window" measurements of the brightness temperature from clouds provide some information on cloud top heights but cloud emissivity and sensor resolution are still sources of error.

Microwave imagery has been used to determine rainfall intensities over the ocean, snow and ice cover. It has also been possible to distinguish between first and multiyear ice. There is a potential capability of measuring soil moisture using long wavelength radiometers, i. e., 21 cm. Landsat visual and near-infrared measurements allow flood monitoring and observations of crop growth.

The Nimbus 4 Backscatter Ultraviolet (BUV) instrument has provided seven years of measurements from which total ozone and the vertical ozone distribution can be determined.

Future missions include TIROS N satellites with improved capabilities for measuring sea surface temperatures, mapping snow and ice fields, monitoring global ozone and continued measurements

of the earth's radiation budget. SEASAT A will be devoted to oceanographic measurements.

Nimbus G sensors will observe certain atmospheric pollutants, oceanic parameters, and weather and climate variables. The Shuttle, in addition to serving as a launch vehicle for free flying satellites, will make periodic calibration checks of instruments on the free flyers and provide facilities for developing, testing, and demonstrating new remote sensors.

CONTENTS

	<u>Page</u>
ABSTRACT	iii
I. INTRODUCTION	1
II. BASIS OF REMOTE SENSING	2
III. EVOLUTION OF ENVIRONMENTAL SATELLITE INSTRUMENTATION	5
A) Cameras.	7
B) Scanners.	8
C) Atmospheric Sounders.	11
IV. SOME RECENT APPLICATIONS OF ENVIRONMENTAL SATELLITE DATA	15
A) Forecasting	15
B) Observations	16
V. FUTURE ENVIRONMENTAL SATELLITE PROGRAMS	31
VI. CONCLUSION	41
VII. ACKNOWLEDGMENT.	43
VIII. REFERENCES	44

71
PAGE INTENTIONALLY BLANK

ILLUSTRATIONS

<u>Figure</u>		<u>Page</u>
1	A schematic illustration of earth-sun-satellite radiative interactions	59
2	Electromagnetic spectrum, types of physical processes involved and instrumentation associated with specific emr intervals.	60
3	Spectral Irradiance (HX) of direct sunlight before and after it passes through the earth's atmosphere. The stippled portion gives the atmospheric absorption; the sun is at zenith (Valley, 1965)	61
4	Electromagnetic spectra of solar and terrestrial radiation (Sellers, 1965)	62
5	Measured transmittances through the atmosphere for the 5 to 25 μ m region (Kunde, 1976)	63
6	Atmospheric transmission characteristics showing major absorption bands	64
7	An artist's conception of the U. S. meteorological satellite program from 1960 to 1976	65
8	Evolution of U. S. meteorological satellite camera systems from 1960 to 1970	66
9	Examples of early TIROS 1 (1960) television pictures.	67

ILLUSTRATIONS (Continued)

<u>Figure</u>		<u>Page</u>
10	Evolution of U. S. meteorological satellite scanner systems from 1960 to 1978	68
11	Nimbus 5 THIR (11 μ m) scan sequence	69
12	Development of a Pacific storm using NOAA 2 visible scanning radiometer data	70
13	A global montage of nighttime infrared data from NOAA-2 SR (10.5 to 12.5 μ m) for the Northern Hemisphere 8/25/74 to 8/26/74	71
14	SMS-1 visible image, 1 n mile resolution, June 30, 1975 with sector of the United States, Caribbean and Hurricane Amy off the U. S. east coast	72
15	Evolution of meteorological atmospheric sounders from 1966 to 1978	73
16	(Left) Average temperature difference (RMS, $^{\circ}$ C) between Nimbus 6 HIRS-SCAMS and radiosondes taken within 2 hrs. of satellite overflight. (Right) Weighting functions for Nimbus 6 HIRS-SCAMS	74
17	Comparison of Nimbus 6 HIRS and radiosonde temperature profile on 29 June 1975	75

ILLUSTRATIONS (Continued)

<u>Figure</u>	<u>Page</u>
18 Comparison of Nimbus 6 HIRS and radiosonde water vapor profile on 26 June 1975	76
19 An overview of the present NOAA-NESS, Dept. of Commerce operational satellite data flow diagram, the end product of which is weather forecasts.	77
20 SMS-1, VISSR infrared surface and cloud (T_B) temperature map of Florida, on 10 January 1976 (4 n mile resolution)	78
21 Cloud heights (km) derived stereographically from SMS-1 and -2 on February 17, 1975 over the U.S., Gulf of Mexico and Caribbean Sea	79
22 The Local User Terminal, developed by NASA for high reso- lution APT-type operation	80
23 Components of the Atmospheric and Oceanographic Information Processing System (AOIPS) at Goddard Space Flight Center, Greenbelt, Md. 20771	81
24 An example of low level winds derived from cloud motion on the AOIPS from 3-minute visible GOES-1 pictures recorded over Tropical Storm Holly, 26 October 1973, 1300 GMT.	82

ILLUSTRATIONS (Continued)

<u>Figure</u>	<u>Page</u>
25 An example of low level winds derived from cloud motion on the McIDAS, at the University of Wisconsin, Madison, Wisconsin, from visible SMS-1, -2 pictures, -30 minute data	83
26 NOAA-4 global infrared SR mean monthly sea surface tempera- ture charts for March 1975	84
27 A simplified Gulf Stream infrared sea surface temperature analysis derived from NOAA-2 VHRR data from 27-30 April 1974	85
28 A NOAA-NESS Great Lakes ice analyses for 7 February 1977 and 21 February 1975 derived from VHRR and VISSR data. . . .	86
29 Seasonal ice boundary changes in the Greenland area from December 1972 to July 1973 as recorded by Nimbus 5 ESMR (19.35 GHz). Open water and old snow appears white (cold), while new ice and snow appear black (warm).	87
30 Seasonal ice boundary changes in the Antarctic area from January to August 1973 as recorded by Nimbus 5 ESMR (19.35 GHz)	88
31 Monthly ice cover changes, in percent over the Antarctic from July 1973 to October 1974, as derived from Nimbus 5 ESMR (19.35 GHz) imagery	89

ILLUSTRATIONS (Continued)

<u>Figure</u>	<u>Page</u>
32 Nimbus 5 ESMR (19.35 GHz) and THIR (11 μ m) facsimile pictures over Hurricane Fifi, on 18 September 1974.	90
33 Global annual oceanic rainfall rate (averaged in mm/hr) from Nimbus 5 ESMR (19.35 GHz) data from January 1974 to December 1974.	91
34 Nimbus 5 ESMR (1.55 cm) facsimile picture over the eastern U. S. on 22 January 1973 and a grid print map analysis (T_B) in $^{\circ}$ K over the Mississippi Valley and Gulf coast, indicating high soil moisture (cold T_B , $<240^{\circ}$ K), in grey tone	92
35 Aircraft thermal infrared (10 to 12 μ m) and microwave (21 cm) brightness temperature versus flight distance at the north end of the Imperial Valley, Calif. The 21-cm brightness temperature and measured soil moisture for several vegetated fields the Salton Sea and desert land are indicated	93
36 Pre-flood (Oct. 2, 1972) and flood (March 31, 1973) stage for the Mississippi River shown by Landsat MSS, Band 7 (0.8 to 11 μ m). A indicates St. Louis, Mo., C and B indicate the confluence of the Missouri and the Mississippi River and the Illinois and Mississippi River respectively; D indicates areas of significant flooding	94

ILLUSTRATIONS (Continued)

<u>Figure</u>		<u>Page</u>
37	Western Negev (vegetated-dark) and Sinai desert non-vegetated (light) on the Israel-Egypt border as shown by LANDSAT 1, MSS, Band 7 picture, 24 August 1973 (80 m resolution)	95
38	Snow cover difference in the Sierra Nevada Mts., near Lake Tahoe, Calif. (left) 25 February 1975 (normal year) and (right) 14 February 1977 (drought year) LANDSAT 2 MSS, Band 5, (0.6 to 0.7 μ m) pictures	96
39	An example of weather modification due to man's industrial activities shown in a LANDSAT 1, (MSS 5) picture recorded on 24 November 1972 over Lake Michigan. SW to NE wind arrows and barbs point to smoke stack plume trajectory over the lake which leads to cloud sheet and snow fall development further downwind. Air temperature visibility and dew point numbers are plotted to left of weather station circle	97
40	Variation in global albedo as measured by Nimbus 6 ERB from July through November 1975, using solar and wide angle channels.	98

ILLUSTRATIONS (Continued)

<u>Figure</u>	<u>Page</u>
41 A) Computed global net radiation balance using 2-channel NOAA-4 SR data. B) Comparison of global mean annual meridional transport of energy by different satellite techniques	99
42 Schematic of Nimbus 4 Backscatter Ultraviolet (BUV) instrument which determines total ozone content and vertical ozone distribution by measuring the backscattered ultraviolet solar energy at the satellite nadir at 12 wavelengths from 2557 to 3398 Angstroms in the ozone absorption band	100
43 Global total ozone content maps (units; milli atm-cm) derived from Nimbus-4 BUV data on April 28-29, 1970 and April 30-May 1, 1970	101
44 Weather satellites to be in orbit during the First GARP Global Experiment (FGGE) 1978-1979	102
45 A schematic of the global data flow and planned data utilization for FGGE program	103
46 Proposed weather satellites and supporting research systems for the U.S. Climate Program	104
47 Climatic cause-and-effect (feedback) linkages (Kellogg and Schneider, 1974)	105
48 SEASAT-A with associated experiments	106

ILLUSTRATIONS (Continued)

<u>Figure</u>	<u>Page</u>
49 A schematic of SEASAT-A ocean data distribution plan	107
50 Nimbus-G with associated experiments	108
51 Conceptual STORMSAT spacecraft with associated experiments	109
52 Chronological development of geostationary meteorological satel- lites leading to the STORMSAT and later SEOS concept	110
53 Instrument development proposed for Shuttle-Spacelab use . . .	111

I. INTRODUCTION

Imaging systems that respond to electromagnetic radiation (emr) within the spectral response range of the human eye have had a long and productive history of development since Daguerre and Niepce reported on their first photographs in 1839. Aerial photography was utilized as early as 1920 by petroleum geologists and 1944 for mineral exploration. Today, aerial and satellite color photography is used in almost all the earth sciences including geology, soils, forestry, agriculture, hydrology, geography and range and wildlife management. The existence of emr adjacent to the blue-violet region of the visible spectrum was demonstrated by J. W. Ritter in 1801, by showing that this invisible emr was even more effective than visible light in blackening silver chloride. The existence of the IR spectral region was demonstrated as early as 1800 by Sir Frederick Herschel and initial work in IR observations of celestial bodies was done by S. P. Langley in the late 1800's.

Although the existence of these regions of the emr spectrum beyond the range of human vision and photographic sensitivity has been known to the scientific world for over 170 years, nearly all useful applications have taken place over only the past 40 years. The term "remote sensing" has become a commonly accepted term and is used in the present context to refer to the whole realm of possibilities afforded by the entire emr spectrum for observations of the Earth's surface and atmosphere from satellites. As sunlight filters down from the top of the atmosphere, it interacts with all particles in any thin

slab of the atmosphere--atomic, molecular and larger--and each slab scatters and absorbs radiation (as does the surface, that is, the lower boundary of the atmosphere). All photons scattered in the direction of the satellite from all intervening slabs of the atmosphere (as well as the surface) have the same energy as the incident photons. The solar energy absorbed throughout the atmosphere (and by the surface) is ultimately reemitted at different wavelengths so that atmospheric interactions throughout the emr spectrum are important to remote sensing.

Any physical interaction between the radiation field and the atmosphere offers a potential means for probing that part of the environment involved in the interaction. It is only necessary to find interactions that are strong enough to be observable, sensitive enough to allow detection of variations and isolated enough from other interactions to permit unambiguous interpretations.

In the following section, the basis for remote sensing will be outlined and in the sequel, the evolution of remote sensors will be illustrated along with examples of practical applications and a prospectus of future developments. Many volumes already exist on just single topics covered here so that completeness has been curtailed in the interest of presenting a broad overview.

II. BASIS OF REMOTE SENSING

The prime source of energy that produces and maintains the atmospheric motions and the spatial and temporal variations of weather is the solar radiation

intercepted by the Earth. The rate at which this energy is received at the Earth's distance from the sun is nearly 1400 Wm^{-2} , but on the average approximately 30 percent of this is reflected back to space by the cloud surfaces, the clear atmosphere, the dust and ice crystals suspended in the atmosphere and by the Earth's surface. Fig. 1 illustrates schematically how the flux from the sun can arrive at an Earth-viewing satellite detector. The radiation may have been scattered, reflected, absorbed and re-emitted several times and each time in a way that is characteristic of the composition, temperature and pressure of the atmospheric gases and the physical properties of the various scatterers. A more complete description of light scattering in planetary atmospheres can be found in Hansen and Travis, 1974.

Fig. 2 shows the extent of the emr spectrum and indicates the kinds of physical processes involved at different wavelengths, along with the names associated with the various intervals. Generic types of instrumentation commonly associated with these intervals are also indicated.

Fig. 3 shows the spectral characteristics of sunlight. The upper solid curve is for above the Earth's atmosphere where the maximum occurs at a wavelength of about $0.47 \mu\text{m}$. About 20% of the total energy is in the region below $0.47 \mu\text{m}$, 44% is in the visible band between 0.4 and $0.76 \mu\text{m}$ and 99% is at the so-called short wavelengths between 0.15 and $4.0 \mu\text{m}$. The lower solid curve is typical of sunlight for cloud-free areas at the surface so that the difference represents that which is scattered or absorbed. The atmosphere is

essentially transparent in the visible and near-infrared portions of the spectrum and these bands of least (but not insignificant) attenuation are called "windows." The windows of importance to remote sensing are shown in Table 1. Atmospheric absorption at wavelengths below $0.3\ \mu\text{m}$ is so intense that little energy reaches the surface. The lower solid curve of Figure 3 is typical of the diffuse short-wave radiation that reaches the surface after absorption by the indicated atmospheric gases with the remainder being scattered by water vapor, dust and other atmospheric molecules.

Fig. 4 is an expansion of Figure 3 with the addition of typical thermal infrared radiation emitted from the surface. In this band, from about 4 to $20\ \mu\text{m}$, strong absorption bands occur that are caused by vibrational-rotational changes due to water vapor and carbon dioxide. These absorption bands break up both the near-infrared and thermal infrared regions into a series of windows of modest transparency interspersed with regions shuttered by absorption. Figure 5 shows the transmittance of the atmosphere within this band and illustrates the complex and pervasive nature of the emr spectrum that must be dealt with in remote sensing. (Kunde et al., 1976.)

At wavelengths larger than $22\ \mu\text{m}$, a whole set of rotational transitions due to water vapor out to $1\ \text{mm}$ and beyond, effectively close the long-wavelength infrared and millimeter regions to remote sensing. No important molecular transitions occur for wavelengths longer than a few centimeters.

Fig. 6 shows a further expansion to include the microwave region where the indicated atmospheric absorption bands are between the windows as given in Table 1 while the rest is very transparent. The effects of clouds are relatively minor over most of the microwave region but for such measurements as the sea surface temperature, their effects must be taken into account. Rainfall interacts with emr in ways that are strongly wavelength and drop-size dependent in the 1 to 10 cm region. Only the most intense rainfall can be detected by microwave at wavelengths beyond 10 cm because rain echoes are proportional to the inverse fourth power of the wavelength.

III. EVOLUTION OF ENVIRONMENTAL SATELLITE INSTRUMENTATION

The development of the first meteorological satellite was a final result of man's determination to increase his perspective of the world in which he lives. An early experiment in satellite meteorology began in 1959 with the U.S. launching of the Vanguard 2 and Explorer 6 and 7. The first two spacecraft were equipped with two photocells and primitive television scanning devices respectively, which were designed to observe large-scale cloud patterns. Explorer 7 was fitted with a low resolution omnidirectional radiometer to measure incoming reflected solar radiation and outgoing thermal radiation emitted by the Earth's atmospheric system, in order to determine the heat budget. These early flights, while not entirely successful, provided U.S. scientists with valuable in-house experience and encouraged the development of the first experimental

spin-stabilized TIROS satellite (Stoldt and Havanac, 1973). Figure 7 shows an artist's conception of the wide variety of U.S. meteorological satellites which were launched into polar and geostationary orbits from 1960 to 1976.

Polar-orbiting environmental satellites circle the earth at altitudes which vary from 650 to 1500 km. Near-to global data are recorded by tape recorder from 12 to 14 orbits daily; each orbit being 90 to 110 minutes in duration. By command, ground stations receive the data and further process it for interested user agencies. Satellites in this category are the TIROS, ESSA, ITOS, NOAA, NIMBUS, and LANDSAT series. With successive launches, it became increasingly apparent that the polar orbiter had a distinct advantage for many users by repetitively viewing large areas with high, medium and low resolution sensors, under similar solar illumination and orbital operating conditions.

Geostationary satellites were positioned into orbits approximately 36,000 km above the equator at predetermined longitudes. Since the satellite has a period equal to the sidereal rotation of the earth (23 hr. 56 min.), it remained fixed in space relative to the earth and thus observed the same area continuously with visible and later infrared instruments. Satellites in this category are the ATS and SMS/GOES series. Table 2 lists in chronological order, the basic scientific-instrumental accomplishments of the U.S. environmental satellite program from 1960 to 1976.

In the subsequent sections, the development of three major instrument classifications, i.e.; cameras, scanners and atmospheric sounders will be briefly discussed.

A) Cameras

The evolution of meteorological satellite cameras is shown in Figure 8. TIROS 1, 2, 3, 4 and 7 carried shuttered television cameras. The photosensitive vidicon tube face 1.27 cm in diameter which viewed the earth scene below was internally scanned (500 times per image) and converted to a recorded analog signal which later was transmitted to the earth upon command.

An example of early TIROS 1 television pictures is shown in Figure 9 (Allison and Neil, 1962). The Advanced Vidicon Camera System (AVCS) and the Automatic Picture Transmission system (APT) were tested on the Nimbus 1 and 2 satellites. The 3-camera AVCS was intended to provide fairly high resolution cloud cover (800 TV lines, 0.5 n.mi) over the full earth and was later flown on ESSA, ITOS and NOAA operational satellites. A more complete description of the degradation and other limitations of the vidicon tube was given by Schwalb and Gross, 1969. The Nimbus 1 and 2 APT cameras used special long-storage vidicon tubes whose dielectric surfaces were capable of holding the earth image for the required 200 second slow-scan readout period. The APT vidicon system (800 TV lines, 2 n. mile resolution) was designed for medium resolution cloud cover imaging for direct readout and was flown on ESSA, ITOS and NOAA satellites. The APT data from three successive orbits

covers 1860 n. mi and is received daily by 600 to 800 ground stations including 78 stations in 43 foreign countries.

The Image Dissector Camera (IDCS), an electrically scanning photocathode was flown on ATS 1, 3, Nimbus 3 and 4 and the ESSA-NOAA series and had a higher dynamic range (1300 TV lines) than the AVCS system. But due to its complexity, the IDCS was replaced by the simpler Spin Scan Cloud Cover Camera on the geostationary ATS satellites (Ostrow and Weinstein, 1968, Minzner and Oberholtzer, 1972).

B) Scanners

The evolution of meteorological satellite scanner is shown in Figure 10. The Medium Resolution Infrared Radiometer (MRIR) was the first 5-channel scanning radiometer to be flown on the TIROS-Nimbus series. It recorded the visible and infrared radiation emitted and reflected back from the earth, clouds and oceans with a ground resolution of 35 n. miles. For the first time, estimates were made of cloud heights, sea surface and ground temperatures, and radiation budget on a quasi-global scale. This instrument, which suffered from a lack of inflight calibration was the forerunner of the High Resolution Infrared Radiometer (HRIR), (Press and Huston, 1968), the Temperature-Humidity Infrared Radiometer (THIR) on the Nimbus series and the operational Scanning Radiometer (SR), the Very High Resolution Radiometer (VHRR) on the NOAA series, the Very High Resolution Radiometer (VHR) on the Defense

Meteorological Satellite Program (DMSP) and the Advanced Very High Resolution Radiometer (AVHRR) on the planned TIROS-N series (1978).

A typical scan sequence of the two-channel THIR on Nimbus 5 is shown in Figure 11. The two detectors ($11\text{ }\mu\text{m}$ and $6.7\text{ }\mu\text{m}$, 8 and 23 km ground resolution at nadir respectively) simultaneously view the spacecraft housing, A at zenith (zero seconds). Seven synchronous pulses start at C, followed by six-1 volt calibration steps. A space scan starts at D to G, followed by an earth scan (117° wide) to I, a space scan to K, a housing scan to M and then back to zenith. The entire sequence lasts 1.23 seconds. The space and housing scan serve as part of the in-flight calibration check. Note the small noise ripple on the housing and space scans (McCulloch, 1972). The NE Δ t for the $11\text{ }\mu\text{m}$ channel is approximately 1.5°K at 185°K and 0.28°K at 300°K . Corrections of 1° , (dry desert areas), to 10°K (moist tropics), must be added to equivalent black-body temperatures of the earth's surface and clouds for losses due to atmospheric water vapor. An example of SR imagery is shown in Figure 12, which depicts the development of a Pacific storm as recorded by the visible channel of NOAA-2 from March 12 to 14, 1974 at approximately 22-2300 GMT. While Figure 13 shows a global montage of nighttime infrared data from NOAA-2 SR for August 25-26, 1974. The arrows indicate the locations of several eastern and western Pacific typhoons, the Asian Monsoon cloudiness and the Intertropical Zone of Convergence over Central Africa.

The ATS-1 and -3 (Figure 10) were equipped with a Spin Scan Cloud Cover Camera (SSCC) that provided full disc (day-time only) pictures of the earth's

cloud cover on a 20-minute basis. Film loops of these early pictures were used to provide winds daily at two levels over the Atlantic & Pacific Oceans. The SSCC and the Multi-color Spin Scan Cloud Cover Camera (MSSCC) on ATS-3 (Suomi and Vonder Haar, 1969) were the forerunners of the operational Visible and Infrared Spin Scan Radiometer (VISSR) flown on SMS-1 (1974) - -2 (1975), GOES (1975) and the Geosynchronous Very High Resolution Radiometer (GVHRR) on ATS-6 (1974). The latter two instruments permitted the first continuous full-disc cloud observation, both day and night.

The VISSR scans from west to east, due to spacecraft rotation, with eight identical visible and two redundant infrared channels. The ground resolution at nadir of the visible (0.55 to 0.70 μm) and infrared (10.5 to 12.6 μm) channels are 0.8 km (0.43 n. mi) and 8 km (4.3 n. mi), respectively. The SMS/GOES rotates at 100 rpm, the VISSR scan mirror views the earth for one-twentieth of each 360° rotation. The radiometer scans from north to south in 18.2 minutes in 1821 successive scan steps. Adding to this, the time needed for ground data acquisition and processing, the final VISSR picture is available to users every thirty minutes. The satellite can also be programmed to scan in a limited mode for R&D studies over severe storm areas (Corbell et al., 1976, Bristol, 1975). Figure 14 shows an example of a SMS-1 visible full-disc picture with a sector of the U.S. and Hurricane Amy off the U.S. east coast on June 30, 1975 (1 n. mi resolution).

C) Atmospheric Sounders

The theoretical basis for the determination of the vertical profile of temperature in the atmosphere was suggested by Kaplan (1959). Basically the concept utilizes measurements by a radiometer with channels sensitive to different spectral regions in and near an absorption band (CO_2 , O_2 and H_2O) such that the weighting functions peak in different parts of the atmosphere. The measured radiances are then "inverted" mathematically in order to derive the temperature structure of the atmosphere. However, there is no unique solution to the problem. For this reason it is necessary to start with a "first guess" vertical temperature profile which is obtained either from a forecast or climatological profile. Various techniques such as inverse matrices, regression methods and iteration are used to obtain a solution. The procedure generally involves knowledge of the transmission functions of the different channels. The transmission functions are derived by matching theoretical absorption based models with experimental measurements of absorption and then applying the models to the atmosphere. Errors arise due to imperfect models and to extrapolation from experimental measurements to different atmospheric pressures and temperatures. In some cases the transmission functions have been modified empirically by comparing measured radiances with computed radiances (Smith et al., 1974). Given the transmission functions, the measured radiances are compared with radiances computed from the first guess profile, which are then

modified by iteration until minimum differences between computed and measured radiances are obtained.

The evolution of atmospheric sounders is illustrated in Figure 15. A Medium Resolution Infrared Radiometer (MRIR) was originally flown on Nimbus 2 (1966). It contained a 14-16 μm (CO_2) radiometer which essentially measured stratospheric temperatures. Nimbus 3 carried a Satellite Infrared Spectrometer (SIRS) and an Infrared Interferometer Spectrometer (IRIS), both of which provided data allowing the first temperature soundings to be derived. Nimbus 4 carried improved versions of these instruments.

Another version of a sounder, the Infrared Temperature Profile Radiometer (ITPR) was flown on Nimbus 5. It had four channels in the CO_2 band between 13 and 15 μm , one channel near 20 μ for sensing atmospheric moisture and two "window" channels at 11 μm and 3.7 μm . The window channel measures the surface temperature minus a correction for atmospheric moisture. The purpose of the two window channels was to detect clouds. The 3.7 μm channel is much more sensitive to warmer temperatures than the 11 μm channel. Hence, if partial cloud cover is in the field of view, the 3.7 μm channel will measure a higher brightness temperature than the 11 μm channel.

A recent improved infrared sounder, flown on Nimbus 6 was the High Resolution Infrared Radiation Sounder (HIRS) which contained 7 channels in the 15 μm CO_2 band, four channels in the 4.3 μm CO_2 band (also sensitive to N_2O),

two water vapor channels at 6.7 and 8.2 μm , and two window channels 3.7 and 11 μm . The spatial resolution of HIRS was about 25 km.

Nimbus 5 also carried a nadir-viewing Microwave Spectrometer (NEMS) which contained 3 channels in the 5 mm O_2 band and two channels near 1.5 cm which are sensitive to water vapor and clouds over the ocean and to temperature and emissivity over land. Nimbus 6 contained a scanning version, the Scanning Microwave Spectrometer (SCAMS) which provides nearly full earth coverage every 12 hours. The weighting functions in the 5 mm O_2 band peaked near 200 mb, 500 mb and the surface. The advantage of the microwave spectrometer is its ability to sound the atmospheric temperature profile through clouds. The combinations of NEMS, ITPR, SCAMS and HIRS provide improved sounding capabilities as compared to the infrared sounders alone.

Nimbus 4 and 5 also contained the Selective Chopper Radiometer (SCR) with eight spectral channels in the 15 μm CO_2 band for measuring temperature profiles up to 50 km. An advanced version, the Pressure Modulator Radiometer (PMR) was flown on Nimbus 6. SCR and PMR have provided some stratospheric temperature profiles on a research basis.

Figure 16 (right) shows the weighting functions of the HIRS and SCAMS. On the left, is the average temperature difference between soundings derived from HIRS and raobs at 30-60° N. It can be seen that the combination of the 15 and 4.3 μm channels provides smaller temperature differences than the 15 or 4.3 μm channels alone. Between 800 and 300 mb, RMS temperature differences

are between 1.5 and 2°C. Differences are greater near the surface (about 2.5°C) and near the tropopause (3.5°C). It should be pointed out that raobs are not necessarily ground truth since two raobs obtained from the same site and time often have temperature differences of 1 to 2°C. Hence in the range between 800 to 300 mb the HIRS soundings may be considered as good as raobs. A very good agreement between HIRS derived temperature profile and raob was obtained on 29 June 1975 (Fig. 17). The inversion between 900 and 700 mb was not detected by HIRS but all other features agree well. The importance of the 4.3 μm CO₂ channels for low level temperature determination is evident since without those channels the derived temperatures differed by as much as 10°K from the raob temperatures. Fig. 18 shows a comparison of water vapor profiles derived from HIRS and raobs. Since there were only two water vapor channels the shape of the profile had to be assumed for the HIRS derivation. However, the results showed good agreement and indicates that useful information can be obtained from the water vapor channels.

An operational atmospheric sounder, the Vertical Temperature Profile Radiometer (VTPR) has been flown on NOAA satellites since October 1972. It contained five-15 μm CO₂ channels, one rotational H₂O channel at 18.7 μm and a window channel at 12 μm . In order to obtain satisfactory results, it was found necessary to use radiosondes for "tuning" the solution of the regression coefficients. Then a greater density of soundings were used which gave RMS

differences of 2° to 3°C at 850 to 200 mb, respectively from nearby radiosondes (Hayden, 1971).

The Geosynchronous Operational Environmental Satellite VISSR Atmospheric Sounder (GOES VAS) to be flown on GOES D, (1980) extends the SMS/GOES Visible and Infrared Spin-Scan Radiometer (VISSR) capability to include additional thermal channels for measurements of the vertical profiles of atmospheric temperature and water vapor. The VAS radiometric measurements consist of eight visible channels and two IR channels. The spatial resolution is 900 meters for the visible band, 7 km for the 11 μ m band and 14 km in the sounding bands. The VAS can operate in the normal VISSR mode, a Multispectral image scanning mode and a Dwell Sounding Mode. This latter mode provides the most accurate localized temperature soundings under clear sky conditions in the vicinity of severe storms. A VAS demonstration experiment sponsored by NASA and NOAA will examine the accuracy and utility of geosynchronous soundings at a prototype operational ground system at the University of Wisconsin and at a limited data facility at GSFC.

IV. SOME RECENT APPLICATIONS OF ENVIRONMENTAL

SATELLITE DATA

A) Forecasting

The Scanning Radiometer (SR) replaced the AVCS television cameras used earlier on the ESSA, ITOS and NOAA satellites thus giving user agencies a vital nighttime coverage (Fortuna and Hambrick, 1974). Fig. 19 shows an overview

of the present NOAA-NESS operational satellite data flow. Forecasters at 50 National Weather Service Field Offices use the satellite pictures to improve short-term forecasts and provide advisory services to the public, industry, i.e., aviation, agriculture and shipping (Hoppe and Ruiz, 1974).

An interesting application of SMS/GOES infrared data is its use in a numerical model to forecast nighttime minimum ground temperatures for the citrus industry in central Florida. Fig. 20 is a real-time surface temperature map of Florida (4 n. mile resolution) on January 10, 1976 which is one of a 30-minute series used to track the cold air as it moved southward across the state. Based upon this movement, frost-freeze forecasts are issued 4 times daily to the citrus growers who must decide whether or not to take protective action in their groves. An Application System Verification Test (ASVT) for this Frost-Freeze system will be run for 3 years to determine the economic value of the satellite system (Bartholic, 1976).

B) Observations

A system entitled GOES-TAP, provides the opportunity to receive SMS/GOES standard sector pictures every thirty minutes by television stations, local governments, Federal agencies, and universities. The SMS/GOES satellites are equipped with a Data Collection System (DCS) which relays environmental data sensed by surface platforms, e.g., rain and river tide gages, ships, buoys, and automatic weather stations. Each spacecraft can receive

data from 10,000 platforms every six hours and relay the data to a central facility for processing.

Simultaneous pairs of visible images from SMS-1 and -2 satellites have been analyzed stereographically to yield cloud heights ranging from 1 to 18 km with a 2-sigma repeatability of 0.4 km. These measurements were made from approximately 50° N to 50° S, in a large overlap area 80° of longitude wide, which is common to both satellites in the northern and southern hemisphere.

Fig. 21 indicates cloud heights derived stereographically from SMS-1, -2 on February 17, 1975 over the Gulf of Mexico and Caribbean Sea (Minzner, et al. 1976).

A new high resolution ground station for receiving pictures direct from weather satellites was recently demonstrated at Goddard Space Flight Center. The Local User Terminal (LUT) Fig. 22, is far superior to the APT system developed in the 1960's. It provides greater picture resolution from VHRR data by day, 0.9 km vs. 3.2 km, by night, 0.9 km vs. 7.2 km. The higher resolution provides meteorologists with better cloud and frontal system identification and delineates potentially severe storm clouds for early warning advisories.

After the launch of ATS-1 in 1966, it was recognized that winds could be determined by tracking clouds. Although individual clouds are affected by growth and dissipation processes, other clouds and gravity waves, it was found that clouds generally move with the wind fields with accuracies approximating operational rawinsonde data (Bauer, 1976).

In order to calculate winds from satellite imagery of clouds, careful geographical registration of succession photographs must be made. This is done by matching landmarks on the sides of the area in which cloud motions are measured. Then the displacements of clouds from successive pictures are measured and the winds calculated. In the SMS photographs, resolutions are 2 to 4 km (visible) and 8 km (infrared) so that often patches of clouds rather than individual clouds are tracked.

Operational determination of wind from SMS/GOES are made at 30 minute intervals. The lifetimes of individual cumulus clouds are also of the order of a half hour. Nevertheless mesoscale patterns of cumulus clouds generally have lifetimes of hours and the motion of these patterns are not greatly different from the rawinsonde measured air motion (Hubert and Whitney, 1974). Measurements at shorter intervals of 15 or 7 minutes or even less have been made and it has been found that the areal coverage has increased significantly. However, accuracy of measurement especially for low wind speeds is more critical at the lower time intervals.

A major problem is the assignment of heights to winds determined by cloud tracking. A skilled operator can distinguish between low, middle, and high clouds. Use of the infrared to determine cloud top temperatures may provide more accurate heights. For a thick cloud the emissivity of the top 100 m may be considered to have an emissivity of unity, so that heights can be determined by matching the measured equivalent black body temperature with a

temperature height profile determined by radiosonde. However, some clouds such as cirrus have emissivities appreciable lower than unity. In addition, other clouds such as cumulus may not uniformly fill the field of view of the sensor. For these reasons, heights determined from infrared measurements may be subject to considerable error. Low level clouds over the oceans are assigned to the 900 mb level which is statistically near the cloud base over oceans. Measurements by Hasler et al. (1976) indicate that low level clouds tend to move with the wind at the cloud base. The heights of middle and upper level clouds are determined by empirical methods using infrared measurements over the densest portions of the clouds and using estimated emissivities ranging upward from about 0.7.

Winds from cloud tracking are generally obtained by man-machine interactive devices such as McIDAS at the University of Wisconsin, the operational MMIPS at NOAA/NESS and AOIPS at Goddard Space Flight Center (Fig. 23). The man is necessary in order to determine which clouds are being tracked as a single layer and are being carried with the wind rather than being formed by gravity waves. The man also distinguishes between low, middle and upper clouds. The computer complex is necessary for speed and accuracy (Billingsley, 1976).

An example of low level winds of Tropical Storm Holly over the Atlantic obtained from 3 minute GOES - 1 pictures produced on the AOIPS is shown in Fig. 24. The wind data is quite dense over the southern sector. The wind

coverage for half hour intervals would be only a small fraction of the number. The map shows an asymmetric flow pattern with strongest wind speeds to the east and lightest speeds to the south of the storm center. (Gentry et al, 1976).

Another example of low level winds on a larger scale is shown in Fig. 25 which was produced by McIDAS during a Data Systems Test for FGGE. Prominent low level features are the anticyclonic circulations shown in the western North Atlantic and in the eastern South Pacific.

Sea surface temperature (SST) is presently determined from intake temperatures by ships of opportunity, drifting and moored buoys and from satellites by infrared radiometry (Szekiela, 1976). Ship and buoy SST measurements are accurate to about 1.5°C (RMS) when compared to oceanographic research vessel temperatures. Since 1970, NOAA meteorological satellites have carried the SR and where clouds were not in the field-of-view, horizontal sea surface temperatures have been obtained. For a nominal case when the SR calibration temperature was 25°C and the ocean scene temperature was 27°C , the NEAT is approximately 0.3°C . The NEAT increases to 1.4°C for the same instrument temperature when the scene is very cold, i.e., -88°C (cloud contaminated). A system noise can result in a NEAT of 1.2°C and 3.5°C for a scene temperature of 27°C and -68°C respectively. An example of a monthly NOAA-4 SST map of the northern hemisphere is shown in Fig. 26 (Brower et al., 1976). Corrections for water vapor absorption were applied to the SR SST data from coincident VTPR soundings. An updated tri-weekly Gulf Stream analysis (Fig. 27) derived

from the VHRR data has been used by the oil tanker industry to save on fuel shipping costs (Stumpf, 1974, Gulfstream Staff, 1977, Cogan and Willand, 1975).

Visible, infrared and microwave sensors are also capable of detecting ice over lakes and oceans. NOAA sensors (VHRR and VISSR) have been used to detect changes in ice cover over the Great Lakes and in the Arctic. In the Great Lakes, four scales in percent of ice cover are used to designate ice cover. Fig. 28 indicates the larger frozen area of the Great Lakes (black) in the winter of 1977 than in 1975.

LANDSAT visible imagery has been used to study ice floe morphology and dynamics in the Arctic on the scale of several days to months and lead and polynya dynamics of one to several days. Nimbus 4 IRLS (Interrogation, Recording and Location System) drifting buoys have permitted the mapping of gross ice drift in the Beaufort sea (Campbell et al., 1973).

With microwave imagery from ESMR-5 (19.35 GHz) and -6 (37 GHz), first and multiyear ice can be distinguished. The emissivity of first year ice is close to unity in the wavelength region 0.3 to 11 cm. Multiyear ice has a lower emissivity either because of the presence of empty brine pockets above sea level or the crystal structure of ice (Gloersen et al., 1972). The brightness temperature (T_b) of Greenland glacier ice showed variations of 50°C with the highest emittance corresponding roughly to the highest elevation. These variations in emissivity are not yet completely understood (Campbell et al., 1973).

The seasonal ice boundary in the Arctic and Antarctic can easily be detected by the sharply higher T_B of the ice as compared to the open water. (Figures 29 and 30). Fig. 31 shows the percentage of ice in 5 degree latitude belts in the Antarctic taken from ESMR-5 imagery between July 1973 and October 1974. In February the ice cover is 95% at 75 - 80°S and 35% at 65 - 70°S. Maximum ice cover is August and September with 95% at 65 - 60°S and about 24% at 55 - 60°S. The year to year variation in a belt is only a few percent as may be seen by comparing the curves for July to October of 1973 and 1974 (Curran and Wexler 1977, Zwally et al., 1976).

In an analysis of Arctic ice using visible imagery from ESSA satellites during 1966-1974, Sanderson (1975) showed that the total ice cover during the winter months has very little variation from year to year although regionally there may be wide variations. This is because excess ice in some regions is counteracted by less ice in other regions. The same appears to be true for Antarctic ice (Ackley and Keliher, 1976) and for winter snow cover in the northern hemisphere (Wiesnet and Matson, 1975).

Rainfall measurements and estimations have been made by conventional meteorological networks using ground, ship and aircraft observations, rain gages and weather radars. With the advent of the meteorological satellite new techniques have been developed to estimate average hourly, daily, and monthly rainfall from satellite cloud photography, using cloud categories and brightness, cloud top temperatures and monthly cloud nephanalyses (Follansbee, 1976,

Martin and Scherer, 1973, and Griffith and Woodley, 1974). The Nimbus 5 ESMR (19.35 GHz) was used to delineate rain areas and provide semi-quantitative rainfall rates within oceanic tropical cyclones on a 12-hr. basis, using a theoretical model for calibration (Allison et al., 1974, 1975). Figure 32 shows the "dark" rain bands of Hurricane Fifi (1974) in the photofacsimile image while the THIR image just shows the overall cloud cover and cloud height. A rainfall atlas depicting global oceanic rainfall rate based upon the Nimbus 5 ESMR brightness temperature was recently published. Fig. 33 shows the first satellite-derived annual distribution of rainfall over the oceans for Jan. 1974 to Dec. 1974 (Rao et al., 1976). The weekly and monthly maps permit the monitoring of the movement of the Intertropical Zone of Convergence, the advance of the Indian Monsoon and Pacific ocean rainfall associated with El Nino phenomenon.

Satellite microwave radiometers have an excellent potential capability to detect soil moisture. The brightness temperature (T_B) recorded by a microwave radiometer is equal to the product of the emissivity and temperature of the surface in the field of view. The emissivity of the soil is determined by the dielectric properties of the surface layer, a few tenths of a wavelength in thickness. The emissivity varies with the type of soil, percentage of moisture and vegetative cover (Yates and Bandeen, 1975).

A photofacsimile microwave image, recorded by Nimbus 5 ESMR on January 22, 1973 (Fig. 34), indicated a persistent soil moisture feature over

the lower Mississippi Valley. Abnormally heavy precipitation had occurred in October, November and December 1972, leaving the alluvial Mississippi Valley soils soaked with standing and subsurface water. Wet soils radiate as cold surfaces in the microwave imagery which shows as white in this figure. A grid print map analysis (b) show two major areas of T_B values of $<220^\circ\text{K}$ in the Mississippi Valley which lie within a large T_B 240°K envelope. This area overlaid the outwash aquifers in the drainage field (Allison et al., 1975).

Data from two radiometers, (21 cm and 2.2 cm) flown aboard Skylab were also compared with data obtained from ESMR-5 (1.55 cm) for a 300 km swath across north-central Texas in June 1973 (Schmugge et al., 1974). Soil moisture in the top 2.5 cm varied from 15 to 70% of field soil capacity. The T_B range was 45K for the 21 cm radiometer, 15K for 2.2 cm and only 5K for 1.55 cm. The small response of the 1.55 cm was ascribed to the presence of vegetation canopy which inhibits penetration for the shorter wavelengths.

Experimental flights over agricultural areas near Phoenix, Arizona and Imperial Valley, California showed that the range in T_B between wet and dry ground for little or no vegetative cover is about 90K for 21 cm and 60K for 1.55 cm. An example of one flight is shown in Figure 35 where the 21 cm radiometer indicated T_B of 206 to 210K for 35% field soil capacity while dry desert (3% field capacity) showed a T_B of 272K. The slope of the T_B curve was greatest beyond 25% field capacity (Schmugge et al., 1976). The 1.55 cm radiometer was found to be incapable of detecting soil moisture variation through a plant canopy. The

21 cm radiometer showed only slight brightness differences over vegetated and bare fields hence was found to be more suitable for observing a wider spectrum of soil moisture than radiometers using shorter wavelengths (Meneely, 1977).

Landsat 1 (1972) data, (80 m resolution) was also found to be very useful as a regional tool for flood mapping during the Spring 1973 Mississippi River disaster. Particularly in the 0.8 to 1.1 μm (Band 7) spectral region of the Multi-spectral Scanner Subsystem (MSS), water and/or moist ground surface show up much darker than dry soil or vegetated areas (Rango and Anderson, 1973). Fig. 36 shows the pre-flood stage of the Mississippi River in the St. Louis area. (C) and (B) indicate the confluence of the Missouri and the Mississippi and the Illinois and Mississippi River, respectively and (D) indicates areas of significant flooding. The stream flow in this area was the highest since 1844 and approximately 10 million acres was under water (Short et al., 1977). Similarly, Band 7, was used to show the western Negev (vegetated-dark) and non-vegetated (light) Sinai desert area on the Israel-Egypt border (Fig. 37). A fence runs along this demarcation line and the bleakness of the ground south and west of the fence is due to over-grazing by camel, sheep, and goats, denuding the existing vegetation (Otterman et al., 1974, Otterman and Fraser, 1976, Allison, 1976).

LANDSAT C (1977), will carry a fifth channel, a thermal infrared band in the MSS which will have a lesser sensor spatial resolution than LANDSAT A and B, namely 200 meters. This channel will improve the capability to classify crops, vegetation and soils.

A Heat Capacity Mapping Mission (HCMM) is planned by Goddard, to map the Northern Hemisphere surface temperatures and derive thermal inertial images near hours of maximum heating (1:30 p. m.) and cooling (2:30 a. m.), with 500 meter resolution. It is expected that soil moisture patterns, soil and rock compositions and geothermal sources can be distinguished better with this satellite than with LANDSAT (Kahle et al., 1976).

A Thematic Mapper, LANDSAT D (1981), is under study at Goddard with plans for a 18-day-repetitive coverage with a 30 meter ground resolution for visible channels and 120 meters for infrared. Four bands will most likely be centered at $0.48 \mu\text{m}$ (blue), $0.56 \mu\text{m}$ (green), $0.66 \mu\text{m}$ (red) and $0.83 \mu\text{m}$ (reflective infrared). Two additional bands near 1.65 and 11.5μ will also be added. The Thematic Mapper will be especially useful for improved monitoring and prediction of the agricultural food resources on a global scale. The system feasibility has been demonstrated by LANDSAT 1 in the Large Area Crop Inventory Experiment (LACIE) (MacDonald, 1976).

Identification of snow cover from satellite has generally been made from visible and to some extent infrared imagery. Microwave detection of snow has also been used in some areas. The primary snow mapping sensors on the NOAA satellites is the VHRR (Very High Resolution Radiometer) with one channel in the visible ($0.6\text{--}0.7 \mu\text{m}$) and another in the window infrared ($10.5\text{--}12.5 \mu\text{m}$) and the Scanning Radiometer (SR) with similar sensors but poorer resolution (McGinnis et al., 1975, Barnes and Bowley, 1974).

Snow has about the same high albedo as many clouds. However, snow can be distinguished from clouds by pattern recognition and stability, since clouds do not retain the same shape for more than an hour. Cloud shadows on the ground can also be recognized at low sun angle.

Wiesnet and Matson (1975) have prepared northern hemisphere average snow charts during the years 1966-1975 for the months September through March. These charts were prepared from photo interpretation of satellite imagery obtained from ESSA, ITOS, NOAA and SMS-1 satellites.

An example of snow detection in the visible using LANDSAT imagery (80 m resolution) is shown in Fig. 38, for the Sierra Nevada Mountains in California. The winter of 1975 was a normal snow year as compared to 1977, a drought year.

Since the capability of the LANDSAT and NOAA satellites to accurately measure snow-covered areas on various size watersheds has been demonstrated, an Application Systems Verification Test (ASVT) Program was initiated to test the results of these studies in Arizona, California, Colorado and Oregon (Rango, 1975). In addition, seasonal stream flow estimations can be made for flood and watershed conditions (Rango et al., 1977).

Similar winter time LANDSAT imagery (Fig. 39) over Lake Michigan, on Nov. 24, 1972 shows smoke plumes from seven steel mills and powerplants in the Chicago, Illinois-Gary, Indiana area. These plumes line up directly with stratoform clouds over the lake and the location of snow on the eastern lake

shore. This picture is an observable example of weather modification due to man's industrial activities (Mercante, 1974, Horan, 1976).

Snow detection using the window region of the infrared (10-12 μm) is possible because of the lower T_B associated with snow cover. However, in mountainous terrain care must be taken in interpreting temperature difference which depend on elevation.

Microwave has the advantage of detecting snow cover through clouds. The emissivity of snow is markedly different from that of bare ground. However, emissivity also varies with the age of the snow, depth and the amount of prior melting and freezing. A comparison of snow cover depths and microwave imagery from ESMR-6 (37 GHz) over Minnesota in December 1973 showed that the 230K T_B isotherm was a good delineation of the snow boundary (Meneely, 1977). Airborne microwave observations of snow indicate that it may be possible to distinguish dry and wet snow due to their different dielectric properties (Schmugge et al., 1973).

The Earth Radiation Budget (ERB) experiment flown on Nimbus 6 (1975), made measurements of the reflected short wave and emitted longwave radiation from the earth and the solar constant. Radiation budget calculations were made over the entire earth disk (3500 Km radius) from 1100 km satellite altitude, with wide angle channels (130° field of view) while narrow angle channels (0.25° x 5°) measured regional values and the angular distribution of outgoing radiation. The ERB solar channels indicated a 1394 w/m^2 value for the solar constant while

rocket measurements taken on 29 June 1976 indicate a lower value, i.e., 1367 w/m^2 (Duncan et al., 1977). The planetary global albedo, long wave radiation fluxes and net radiation were computed to be 30%, 240 w/m^2 and -4 w/m^2 for the months of July and August 1975, in good agreement with prior Nimbus 3 calculations (Smith et al., 1977). Albedo charts for August 1975 prepared from wide angle data (0.2 to $3.8 \mu\text{m}$) show maxima over northern tropical South America, the bright sands of the Sahara Desert and the Tibetan Plateau while minima were found in the oceanic sub-tropical high pressure ridges. The narrow angle measurements showed that Greenland was a highly specular reflector of short wave radiation but a diffuse emitter of long wave radiation whereas the Sahara Desert displayed the opposite characteristic. The variation in global albedo with latitude for different months is shown in Figure 40. Gruber (1976), using SR data (0.5 to $0.7 \mu\text{m}$ and 10.5 to $12.0 \mu\text{m}$ channels) computed net radiation balance profiles from June 1974 to May 1975 (Figure 41A). There was a net radiation loss in the winter hemisphere and a gain in the summer hemisphere. The net gain in the southern hemisphere summer is larger than the northern hemisphere summer. Mean annual meridional transport of energy computed by Gruber, 1976 (Fig 41B), agreed well with others but the northern hemisphere transport was appreciably greater in the southern hemisphere.

Measurements of total atmospheric ozone content were made in the last forty years by a poorly spaced quasi-global network of ground based Dobson spectrometers, balloons and sounding rockets. Much of the more recent

satellite ozone measurements were made by Nimbus-3 and -4 IRIS (Prabhakara et al., 1970, 1973) and Nimbus-4 Backscatter Ultraviolet instrument (BUV) (Krueger et al., 1973). The BUV, a double (cascaded) Ebert-Fastie spectrophotometer which was launched in April 1970 is still providing daily ozone data after seven years of operation. A similar instrument, launched on Atmosphere Explorer 55 in late 1975, is providing ozone data in an equatorial orbit over the region of the most active ozone formation. The BUV determines the total ozone content and vertical ozone distribution by measuring the backscattered ultraviolet solar energy at the satellite nadir at 12 wavelengths from 2550 to 3400 Angstroms in the ozone absorption band (Figure 42). The shorter wavelengths are more sensitive to ozone high in the stratosphere and the longer wavelengths are most sensitive to ozone low in the stratosphere. To infer the ozone profile, the atmospheric albedo must be determined to within one percent.

Figure 43 shows two periods (April-May 1970) of global ozone data processed from Nimbus 4 BUV data. A full-scale effort to produce an atlas of the 7 years of BUV ozone data is now underway at Goddard. The Solar Backscatter Ultraviolet and Total Ozone Mapping Spectrometer (SBUV/TOMS) experiment to be flown on Nimbus G in 1978 will measure the ozone vertical profile and solar UV spectrum and provide a total ozone map by means of a mechanical scan across the Nimbus track. This instrument is a refinement of the BUV system with special provisions for minimizing the effects of space radiation (Heath et al., 1975).

The Limb Radiance Inversion Radiometer (LRIR) flown on Nimbus 6 (1975) also made measurements of the vertical distribution of ozone, temperature, and water vapor from 15 km to 60 km on a global scale (Gille et al., 1975). Vertical distributions were determined by inverting measured limb radiance profiles from the LRIR, an infrared multispectral scanning radiometer in four spectral regions: two in the $15\text{ }\mu\text{m}$ CO_2 band, one in the $9.6\text{ }\mu\text{m}$ ozone band, and one in the $23\text{ }\mu\text{m}$ to $2\text{ }\mu\text{m}$ rotational water vapor band.

V. FUTURE ENVIRONMENTAL SATELLITE PROGRAMS

The Global Atmospheric Research Program (GARP) was established in 1967 by the World Meteorological Organization (WMO) and the International Council of Scientific Unions (ICSU) in response to resolutions of the United Nations. It is an international cooperative effort to increase the accuracy of medium range weather forecasting (1 day to 2 weeks), to develop mathematical models of the atmosphere which will permit reliable long-range weather forecasts, to guide the design of a cost-effective global observing and forecasting system for routine use by the international community, and to investigate the mechanisms underlying climate variations which may lead eventually to some level of climate prediction. The First GARP Global Experiment (FGGE) will have 145 member country participants and global observations will be taken from 1 September 1978 to 31 August 1979 with intensive observing periods Jan. to Feb. and May to June 1979 (Global Atmospheric Research Program, 1973). The system will utilize the following:

- | | |
|---|-----------------------|
| - World Weather Watch surface-based stations | - Global |
| - 4 Polar Orbiting weather satellites | - Global |
| - 5 Geostationary weather satellites | - 50°N to 50°S |
| - Special and commercial aircraft releasing
dropsondes | - Tropics |
| - 50 Ships releasing radiosondes | - Tropics |
| - 300 Ocean drifting buoys | - Southern hemisphere |
| - Commercial ships equipped with weather
instruments | - Southern hemisphere |

Figure 44 shows the full complement of weather satellites to be in orbit by 1978-79 for this experiment while Figure 45 illustrates schematically the global data flow and planned utilization for the FGGE program (Greaves, 1977). NASA has already conducted six Data System Tests (DST) to date to address problems in data management and utilization and to demonstrate the full potential of satellite temperature sounding data.

A Climate Research Program, now under study at Goddard Space Flight Center will make full use of the TIROS-N, GOES-METEOSAT, and proposed "CLIMSAT" and "ERBS-A" satellites shown in Figure 46. With this system, most of the climate-related observational requirements now anticipated can be met (Global Atmospheric Research Program, 1975). In those areas where the requirements cannot be met by direct observations special intensive studies are planned so that the climate parameter can be derived and later modeled.

Figure 47 illustrates the complicated climatic cause-and-effect (feedback) linkages which have an important effect on the earth's climate. These and other meteorological parameters, which may be partially monitored by satellites will be recorded and fed into mathematical climate models for further study (Kellogg and Schneider, 1974, Schneider and Dickinson, 1974, National Academy of Sciences, 1975, Laurmann, 1975).

The TIROS-N a two-satellite system to be launched in 2nd quarter of 1978, was designed to provide better meteorological data than the present NOAA polar orbiting satellites. It's major improvements will be higher spatial accuracy, an increase in the number of tropospheric and stratospheric temperature and water vapor soundings under clear sky and cloudy conditions by the TIROS Operational Vertical Sounder (TOVS), increased spectral radiometric information by the Advanced Very High Resolution Radiometer (AVHRR) for more accurate sea surface temperature mapping and delineation of melting snow and ice fields, a remote platform location and data collection capability (ARGOS) and increased proton, electron and alpha particle spectral information by the Space Environment Monitor (SEM) for improved solar disturbance prediction (Schneider, 1976). Direct readout of Automatic Picture Transmission (APT) and High Resolution Picture Transmission (HRPT) data to a world-wide ground network will be provided for operational coverage. For purposes of the Climate Program, and to support NOAA operational needs, it has been suggested that two instruments be added to TIROS-N:

a. A solar Backscatter Ultra-Violet Instrument System (SBUV) to monitor global ozone and solar ultra-violet flux.

b. An Earth Radiation Budget Satellite Instrument (ERBSI).

The SBUV measures backscattered and direct solar ultraviolet radiation in 12 channels of the UV spectrum. The instrument is nadir viewing with a field of view covering 165 km on the earth. These data are used to derive the total ozone in the vertical column and also the vertical profile of the ozone concentration. The second instrument is the Earth Radiation Budget Instrument. This instrument system, consisting of two optical units, measures the total upwelling radiation in the 0.2 to 50 micrometer band and the reflected visible radiation in the 0.2 to 5.0 micrometer band. Three spatial resolutions are used in parallel, a wide field of view (1000 km) sensor and a narrow field of view (87 km) scanning unit. These data are used in combination to derive global, zonal, and regional values of the components of the earth's radiation budget. For calibration purposes, a solar constant measurement channel is also included. Interest in including both the ERBS and SBUV instruments on TIROS-N has been expressed by NOAA. Table 3 gives the TIROS-N payload characteristics.

The orbital parameters and instrument payloads for an earth radiation budget and stratospheric aerosol satellite (ERBS-A) and CLIMSAT A and B are still under consideration for final selection.

The oceans which cover about two-thirds of the earth's surface has important influences on our weather and climate and is an important resource needing further exploration. The SEASAT-A program will demonstrate synoptic monitorings of the motions and temperatures of the oceans and provide better ocean ship routing and warnings of severe wind-wave, rain, sea current and ice conditions which should benefit the oceanographic community.

SEASAT-A (Figure 48) to be launched on May 1978 will carry complement of instruments fully dedicated to oceanic prediction (NOAA Staff members, 1977).

The sensor applications are as follows:

- Altimeter: A nadir-looking instrument that measures the displacement between the satellite and the ocean surface to a processed accuracy of 10 cm every 18 km and a RMS roughness of that surface to 1 meter.
- Radar: A 100 km swath-width image of the ocean surface with a 25 meter spatial resolution and viewed every 18 days.
- Scatterometer: Low to intermediate surface wind velocity determined over a swath width of 1200 km, providing global coverage ($\pm 75^\circ$ latitude) every 36 hours on a 100 km grid basis.
- Microwave Radiometer: Ice boundaries and leads, atmospheric water vapor, sea surface temperature, and intermediate to high wind speeds are provided over a swath width of 1000 km every 36

hours. Spatial resolution of ice features is 25 km and 125 km for sea surface temperature.

- Visible and IR Radiometer: Provide a 7 km spatial resolution imagery for feature identification for the microwave data.

An example of the ocean data distribution plan for SEASAT-A is shown in Figure 49.

Nimbus G to be launched in the 4th quarter, 1978 is a multidisciplinary satellite with application to pollution monitoring, oceanography, and weather and climate (Figure 50). The payload consists of eight instruments (Staff members, Goddard Space Flight Center, 1976):

- 1) Scanning Multichannel Microwave Radiometer (SMMR). Measures radiances in five wavelengths and ten channels to extract information on sea surface roughness and winds, sea surface temperature, cloud liquid water content, precipitation (mean droplet size), soil moisture, snow cover and sea ice. (Gloersen and Barath, 1977)

- 2) Stratospheric and Mesospheric Sounder (SAMS). Measures vertical concentrations of H_2O , N_2O , CH_4 , CO and NO; measure temperature of stratosphere to ~90 km and trace constituents.

- 3) Solar-Backscattered Ultraviolet/Total Ozone Mapper System (SBUV/TOMS). Measures direct and backscattered solar UV to extract information on variations of solar irradiance, vertical distribution of ozone and total ozone on a global basis.

4) Earth Radiation Budget (ERB). Measures short- and longwave upwelling radiances and fluxes and direct solar irradiance to extract information on the solar constant, earth albedo, emitted longwave radiation and the anisotropy of the outgoing radiation.

5) Coastal Zone Color Scanner (CZCS). Measures chlorophyll concentration, sediment distribution, gelbstoff (yellow substance) concentration as a salinity indicator and temperature of coastal waters and open ocean.

6) Stratospheric Aerosol Measurements II Experiment (SAM II). Measures the concentration and optical properties of stratospheric aerosols as a function of altitude, latitude and longitude. Tropospheric aerosols can be mapped also if no clouds are present in the IFOV.

7) Temperature-Humidity Infrared Radiometer Experiment (THIR). Measures the infrared radiation from the earth in two spectral bands ($11\ \mu\text{m}$ and $6.7\ \mu\text{m}$) both day and night to provide pictures of cloud cover; three-dimensional maps of cloud cover, temperature maps of clouds, land and ocean surfaces, and atmospheric moisture.

8) Limb Infrared Monitoring of the Stratosphere Experiment (LIMS). Make a global survey of selected gases from the upper troposphere to the lower mesosphere. Inversion techniques are used to derive gas concentrations and temperature profiles.

The Nimbus G launch will coincide with the FGGE and substantially enhance the results of that experiment.

The main objective of the proposed STORMSAT mission is to observe meso- and synoptic scale meteorological parameters from geostationary altitude for use in early detection and prediction of severe local storms (Fujita, 1973, Fujita et al., 1976). Vertical temperature and moisture sounding under cloudy and clear sky conditions and high resolution imagery from the Advanced Atmospheric Sounding and Imaging Radiometer (AASIR) and Microwave Atmospheric Sounding Radiometer (MASR) can best be obtained from a three-axis stabilized satellite. This system offers an order of magnitude sensing improvement over a spinning GOES VAS system. Preliminary design studies of the AASIR, the spacecraft and ground system design for STORMSAT has been completed. (Computer Sciences Corporation, 1976) (Figure 51). Figure 52 shows the chronological development of geostationary satellites to the present STORMSAT concept (U. S. Dept. of Commerce, 1976).

From early in the 1980's, and at least throughout the following decade, the Shuttle will be NASA's transportation system for access to space. Beyond that, the joint venture with European countries in developing the Spacelab will provide a functioning manned laboratory facility in space. These two programs will have a major impact on and will play vital roles in the development of future remote sensors. The four functional categories that these programs will provide are as follows: (1) calibration of instruments on operational satellites, (2) direct monitoring of slowly changing earth/atmosphere parameters,

(3) development and demonstration of new remote sensors, and (4) special experiments not possible or impractical by other means.

The difficulties inherent to calibration and correction for long-term drift of satellite instruments has in the past presented manifold problems. First, logistic problems associated with deployment of enough ground systems and interrelating their independent errors imposed severe limitations. A second factor is that ground instruments do not generally measure the same quantities as satellite instruments. For example, a satellite radiometer measures a brightness temperature (T_B) integrated over the entire scene in view, while ground truth data are usually restricted to point measurements. Thus, at least for NASA's emerging Climate Program, calibrations of satellite instruments over their several years of useful lifetimes, as well as interrelating succeeding satellites, is a crucial requirement. The Shuttle can fulfill this requirement by periodic flight of instruments, calibrated against standards before and after flight, that can provide comparative measurements at points of orbit conjunction with the satellites when identical scenes are in view.

Monitoring of certain slowly varying parameters can be accomplished directly by regular flights in conjunction with Shuttle-Spacelab missions. The requirements for measuring the solar spectral irradiance can be adequately met by two flights per year spaced at six month intervals (Fig. 53). Experience with the Nimbus-6 ERB instrument substantiates the desirability of continuing total solar flux measurements at six month intervals. Such measurements will

provide an independent and highly calibrated set of data by themselves, but will also serve to inter-relate the total solar flux measurements of the ERBSI proposed for TIROS-N. Other parameters that can be directly monitored by the Shuttle-Spacelab include a number of the well mixed atmospheric constituents, ozone, and tropospheric aerosols. For example, annual measurements are probably adequate for CO_2 , CFM's, N_2O , NO_x and CH_4 .

The Spacelab will also provide the needed facilities to develop, test and demonstrate new remote sensors. Briefly, some of these are:

(a) Sea Surface Temperature: Improvements that appear possible include increased signal-to-noise ratios and additional wavelengths to reduce errors due to atmospheric water vapor and clouds.

(b) Vertical Temperature Profile: Accuracy of passive sounding below 20 km altitude can be improved with measurements at $4\ \mu\text{m}$ and with bandwidths of 2 wave numbers. Active Lidar promises even higher accuracy along with an order of magnitude improved vertical resolution.

(c) Winds: Lidar techniques may be able to measure wind speed and direction in cloud-free regions.

(d) Stratospheric Aerosols: Stellar sources provide a large number of occultations not limited to the ecliptic plane so that reasonably good coverage of stratospheric aerosols is possible.

(e) Tropospheric Aerosols: At present, no technique exists for measuring tropospheric aerosols, but a pulsed lidar system is believed to hold promise.

As plans for the development of these instruments, as well as any others that have and may yet be identified, are formulated to the point that space flight development and testing can be visualized, the advantages that Spacelab can provide will be capitalized upon the maximum extent possible.

There are two particularly important special experiments in the area of remote sensing that are especially suited to the Spacelab capabilities. These are: extended cloud physics and radiation studies; and precipitation over land and water. In the case of the extended cloud and radiation studies a group of instruments including two separate radiometers and a lidar system are required. In the case of the precipitation studies, a microwave radiometer, a visible band radiometer, an IR radiometer and a 10 cm radar are required. A number of short duration flights are adequate to meet the objectives of both of these studies and Spacelab offers a unique capability for their accomplishment.

VI. CONCLUSION

The meteorological satellites have used instrumentation sensitive to different portions of the electromagnetic spectrum to observe and measure atmospheric and surface properties. In the ultraviolet, solar variability has been measured and total atmospheric ozone determined. In the visible, imagery of cloud systems has provided better location of storms in data sparse areas, observed ice and snow boundaries, and monitored floods. In the infrared, sea surface and cloud top temperatures have been measured and water vapor flow patterns determined. By using infrared CO₂ absorption bands, centered at

4.3 and 15 μm , radiometers have derived atmospheric vertical temperature profiles. Microwave radiometer measurements in the 5 mm O_2 absorption bands have improved these atmospheric soundings and allowed penetration through clouds. Microwave measurements near 1.55 and 0.8 cm have determined rainfall intensities over the ocean, snow and ice boundaries through clouds, and have provided some indications of soil moisture.

Cloud tracking from geosynchronous satellites have allowed wind determinations at different levels from which important properties such as divergence and vorticity have been derived. Geosynchronous satellites have also monitored the development and motions of severe storms such as hurricanes or severe thunderstorms with hail or tornados. These observations and measurements have not only increased our knowledge of atmospheric processes but also have been used operationally in short term forecasting. For practical use, the satellite provides observations denser in time and space scales than any national network of surface observing stations.

Future approved satellite missions include improved resolutions for some of the above measurements but also include new experiments such as pollution detection and oceanographic monitoring. Proposed satellite missions include STORMSAT, a geosynchronous satellite, for better monitoring of severe storms with temperature and moisture sounding capabilities.

A proposed Climate Program would provide observations from a system of satellite sensors for numerical modeling of climate, leading to a better

understanding of climate processes and, hopefully, to an improved capability to predict climate change.

VII. ACKNOWLEDGMENT

The authors wish to thank Professor G. C. Gill, University of Michigan for his encouragement in writing this paper.

VIII. REFERENCES

- Ackley, S. F. and T. E. Keliher, 1976, "Antarctic Sea Ice Dynamics and It's Possible Climatic Effect", AIDJEX Bulletin, No. 33, p.p. 53-76.
- Allison, L. J. and Neil, E. A., 1962: "Final Report on the TIROS 1 Meteorological Satellite System", NASA TR R-131, Goddard Space Flight Center, Greenbelt, Md., p.p. 258.
- Allison, L. J., E. B. Rodgers, T. T. Wilheit, and R. W. Fett, 1974, "Tropical Cyclone Rainfall as Measured by the Nimbus 5 Electrically Scanning Microwave Radiometer", Bull. of American Meteorological Society, Vol. 55, No. 9, p.p. 1074-1089.
- Allison, L. J., E. B. Rodgers, T. T. Wilheit and R. Wexler, 1975, "A Multi-sensor Analysis of Nimbus 5 Data Recorded on January 22, 1973", NASA TN D-7911, Goddard Space Flight Center, Greenbelt, Md., p.p. 44.
- Allison, L. J., 1977, "Geological Applications of Nimbus Radiation Data in the Middle East", NASA TN D8469, Goddard Space Flight Center, Greenbelt, Md., p.p. 79.
- Barazotto, R. M., 1977, "Winter of Extremes as Viewed from NOAA Satellites", Mariners Weather Log, Vol. 21, No. 2, p.p. 73-77.
- Barnes, J. C. and C. J. Bowley, 1974, "Handbook of Techniques for Satellite Snow Mapping", ERT Document 0407-A, ERT, Concord, Mass., p.p. 100.
- Bartholic, J. F., 1976, Private Correspondence.

- Bauer, K. E., 1976, "A Comparison of Cloud Motion Winds Extracted from SMS-1 Infrared Images with Coinciding Radiosonde Winds Over North America", Studies of the Atmosphere Using Aerospace Probes, U. of Wisconsin, Madison, Wisconsin, p. p. 45-78.
- Billingsley, J. B., 1976, "Interactive Image Processing for Meteorological Applications at NASA/Goddard Space Flight Center", Seventh Conference on Aerospace and Aeronautical Meteorology and Symposium of Remote Sensing from Satellites, Nov. 16-19, 1976, Melbourne, Florida, p. p. 268-275.
- Bristor, C. L., 1975, "Central Processing and Analysis of Geostationary Satellite Data", NOAA TM NESS 64, p. p. 155.
- Brower, R. L., H. S. Gohrband, W. G. Pichel, T. L. Signore and C. C. Walton, 1976, "Satellite Derived Sea-Surface Temperatures from NOAA Spacecraft", NOAA Tech. Memo NESS 78, U.S. Dept. of Commerce, NOAA, NESS, Wash., D.C., pp 74.
- Campbell, W. J., P. Gloersen, W. Nordberg, T. Wilheit, 1973, "Dynamics and Morphology of Beaufort Sea Ice," GSFC X-650-73-791, pp 20.
- Cogan, J. L. and J. H. Willand, 1975, "Mapping of Sea Surface Temperature by the DMSP Satellite", ERT Document No. 1065, Final Report EPRF 7-75 (ERT), ERT Inc. Concord, Mass. 01742.
- Computer Sciences Corporation, 1976, "Stormsat Ground System Concept Study", CSC/SD -76/6088, Contract NAS 5-11999 Computer Sciences Corp., Silver Spring, Md.

- Conlan, E. F., 1973, "Operational Products from ITOS Scanning Radiometer Data", U.S. Dept. of Commerce, Wash., D.C., NOAA Tech. Memo. NESS 52, pp 57.
- Corbell, R. P., C. J. Callahan and W. J. Kotsch, 1976, "The GOES/SMS User's Guide", NOAA-NESS, NASA, Washington, D.C. pp. 118.
- Curran, R. and R. Wexler, 1977, "Separation of cloud contribution to the Monthly Zonal Albedo", Unpublished manuscript.
- Duncan, C. H., R. G. Harrison, J. R. Hickey, J. M. Kendall, Sr., M. P. Thekaekara, R. C. Willson, 1977, "Rocket Calibration of the Nimbus 6 Solar Constant Measurements", NASA X-942-77-66, pp. 32 (to be published in Science).
- Follansbee, W. A., 1976, "Estimation of Daily Precipitation over China and the USSR Using Satellite Imagery", NOAA TM NESS 81, U.S. Dept of Commerce, NOAA, NESS, Wash., D.C. pp. 30.
- Fortuna, J. J. and L. N. Hambrick, 1974, "The Operation of the NOAA Polar Satellite System", NOAA TM NESS 60, U.S. Dept. of Commerce, NOAA, NESS, Wash., D.C. pp. 127.
- Fujita, T., 1973, "Tornadoes Around the World," Weatherwise, Vol. 26, No. 2, pp 56-83.
- Fujita, T., G. S. Forbes, T. A. Umenhofer, 1976, "Close-up View of 20 March 1976 Tornadoes, Sinking Cloud Tops to Suction Vortices", Weatherwise, Vol. 29, No. 3, pp 117-145.

- Gentry, R. C., E. Rodgers, W. E. Shenk, V. Oliver, 1976, "Deriving Winds for Hurricanes Using Short Interval Satellite Imagery", Seventh Conference on Aerospace and Aeronautical Meteorology and Symposium on Remote Sensing from Satellites, Nov. 16-19, 1976, Melbourne, Florida, pp 115-118.
- Gillie, J. C., F. B. House, R. A. Craig, J. R. Thomas, 1975, "The Limb Radiance Inversion Radiometer (LRIR) Experiment", Nimbus 6 User's Guide, NASA, Goddard Space Flight Center, Greenbelt, Md. pp. 141-162.
- Global Atmospheric Research Program (GARP), 1973, "The First GARP Global Experiment," GARP Publications Series No. 11, WMO-ICSU Joint Organizing Committee, pp. 107.
- Greaves, J. 1977, Private Correspondence.
- Global Atmospheric Research Program (GARP), 1975, "The Physical Basis of Climate and Climate Modeling", GARP Publications Series No. 16, WMO-ICSU Joint Organizing Committee, pp 265.
- Gloersen, P., W. Nordberg, T. Schmugge, T. Wilheit, W. Campbell, 1972, Microwave Signatures of First-Year and Multiyear Sea Ice, GSFC X-652-72-312, pp 19.
- Gloersen, P. and F. T. Barath, 1977, "A Scanning Multichannel Microwave Radiometer for Nimbus G and SeaSat-A", IEEE Jrl. of Oceanic Engineering, Vol. OE-2, No. 2, pp 172-178.

- Griffith, C. G. and W. L. Woodley, 1974, "Rainfall estimates from Geosynchronous Satellite Imagery". Proc. 11th Space Congress, Cocoa Beach, Fla., August 17-19, 1974.
- Gruber, A., 1976, "Satellite Estimates of the Earth-Atmosphere Radiation Balance", Proc. of the Symposium on Radiation in the Atmosphere (IAMAP), August 19-28, 1976, Garmisch-Partenkirchen, FRG.
- Gulfstream Staff, 1977, "Gulf Stream Navigation for Fuel Savings", Gulfstream, Vol. 11, No. 9, U.S. Dept. of Commerce, NOAA, NWS, Wash., D.C. pp 6-7.
- Hansen, J. E. and L. D. Travis, 1974, "Light Scattering in Planetary Atmospheres", Space Science Reviews 16, pp 527-610.
- Hasler, A. F., W. Shenk and W. Skillman, 1976, "Wind Estimates from Cloud Motions". Jl. App. Meteor. 15, 10-15.
- Hayden, C., 1976, "The Use of the Radiosonde in Deriving Temperature Soundings from the Nimbus and NOAA Satellite Data," NOAA TM NESS 76, pp 19.
- Heath, D. F., A. J. Krueger, H. A. Roeder, and B. D. Henderson, 1975, "The Solar Backscatter Ultraviolet and Total Ozone Mapping Spectrometer (SBUV/TOMS) for Nimbus G," Optical Eng., Vol. 14, No. 4, pp 323-331.
- Hoppe, E. R. and A. L. Ruiz, 1974, "Catalog of Operational Satellite Products", NOAA TM NESS 53, U.S. Dept. of Commerce, NOAA, NESS, Wash., D.C. pp 91.

- Horan, J., 1976, "LANDSAT", Multispectral Eye in the Sky", IEEE Spectrum, March 1976, pp 59-62.
- Hubert, L. E. and L. F. Whitney, 1974, "Comparability of Low Level Cloud Vectors and Rawins for Synoptic Analysis", NOAA Tech. Mem. NESS 70, pp 26.
- Johnson, J. D., F. C. Parmenter, and R. Anderson, 1976, "Environmental Satellites," U.S. Dept. of Commerce, Wash., D.C. NOAA, NESS, pp 66.
- Kahle, A. B., A. R. Gillespie and A. F. H. Goetz, 1976, "Thermal Inertia Imaging: A New Geologic Mapping Tool", Geophysical Research Letters, Vol. 3, No. 1, pp 26-28.
- Kaplan, L. D., 1959, Inference of Atmospheric Structure from Remote Radiation Measurements, J. Opt, Soc. Amer. 49, 1004-1007.
- Kellogg, W. W. and S. H. Schneider, 1974, "Climate Stabilization: For Better or Worse", Science, Vol. 186, No. 4170, pp 1163-1172.
- Krueger, A. J., D. F. Heath and C. L. Mateer, 1973, "Variations in the Stratospheric Ozone Field Inferred from Nimbus Satellite Observation", Pure Appl. Geophys, No. 106-108, pp 1254-1263.
- Kunde, V. G., R. A. Hanel, L. W. Herath, 1976, "High Spectral Resolution Ground-Based Observations of Venus in the 450-1250 cm^{-1} Region, NASA X-622-76-249, pp 39.
- Laurmann, J. A., 1975, "On the Prospects for Seasonal Climate Forecasting", Bulletin of American Meteorological Society, Vol. 56, No. 10, pp 1084-1088.

- Lintz, J. Jr., and D. Simonett, eds. (1976), "Remote Sensing of Environment".
Addison-Wesley Publishing Co., Reading, Mass., pp 694.
- MacDonald, R. B., 1976: "The Large Area Crop Inventory Experiment", 2nd
Annual W. T. Pecora Memorial Symposium, Sioux Falls, S. D., 25-29
Oct. 1976, pp 20.
- Martin, D. W. and W. D. Scherer, 1973, "Review of Satellite Rainfall Estima-
tion Results", Bull. of Amer. Meteor. Soc., 54, pp 661-674.
- McCulloch, A. W., 1972, "The Temperature-Humidity Infrared Radiometer
(THIR) Subsystem", Nimbus 5 User's Guide, ERTS/Nimbus Project,
Goddard Space Flight Center, Greenbelt, Md. pp. 11-47.
- McGinnis, D. F., J. A. Pritchard, D. R. Wiesnet, 1975, "Determination of
Snow Depth and Snow Extent from NOAA 2 Satellite Very High Resolution
Radiometer Data", Water Resources Research, Vol. 11, No. 6, pp
897-902.
- Meneely, J. M., 1977, "Application of the Electrically Scanning Microwave
Radiometer (ESMR) to Classification of the Moisture Condition of the
Ground", Final Report, Earth Satellite Corporation, Wash. D.C. pp 39.
- Mercanti, E. P., 1974, "Widening ERTS Applications", Astronautics and
Aeronautics, May 1974, pp 28-39.
- Minzner, R. A. and J. D. Oberholtzer, 1972, "Space Applications Instrumenta-
tion Systems, NASA TM X-2066, NASA, Wash., D.C. pp 262.

- Minzner, R. A., W. E. Shenk, J. Steranka, R. D. Teagle, 1976, "Cloud Heights Determined Stereographically From Imagery Recorded Simultaneously by Two Synchronous Meteorological Satellites, SMS-1 and SMS-2", Proceedings of 1976 Spring AGU Meeting, Wash., D.C.
- National Academy of Sciences, 1975, "Weather and Climate," Report of the Panel of Weather and Climate to the Space Applications Board of the Assembly of Engineering, National Research Council, NAS, Wash., D.C. pp. 25.
- NOAA Staff Members, 1977, "NOAA Program Development Plan for SEASAT-A Research and Applications", U.S. Dept. of Commerce, NOAA, NESS, Wash., D.C. pp 95.
- Ostrow, H. and O. Weinstein, 1968, "A Review of a Decade of Space Camera Systems Development for Meteorology", Proceedings of the SPIE 13th Annual Technical Symposium, Society of Photographic-Optical Instrumentation Engineers, Wash., D.C. pp 251-262.
- Otterman, J., G. Ohring, and A. Ginzburg, 1974, "Results of the Israeli Multidisciplinary Data Analysis of ERTS-1 Imagery," Remote Sensing of the Environment, Vol. 3, pp 133-148.
- Otterman, J., P. D. Lowman, and V. V. Salomonson, 1976: "Surveying Earth Resources by Remote Sensing from Satellites", Geophysical Surveys, Vol. 2, pp 431-467.
- Otterman, J. and R. S. Fraser, 1976: "Earth-Atmosphere System and Surface Reflectivities in Arid Regions from LANDSAT MSS Data," Remote Sens. of Envir., 5, pp 247-266.

- Prabhakara, C., B. Conrath, and R. A. Hanel, 1970, "Remote Sensing of Atmospheric-Ozone Using the 9.6 μ m Band", J. Atmos. Sci, Vol. 27, pp. 689-697.
- Prabhakara, C., V. V. Salomonson, B. J. Conrath, J. Steranka and L. J. Allison, 1973, "Nimbus 3 Satellite Observations of Ozone Associated with the Easterly Jet Stream over India during the 1969 Summer Monsoon," Jrl of the Marine Biological Assn. of India, Vol. 14, No. 1, pp 42-54.
- Press, H. and W. B. Huston, 1968: "Nimbus: A Progress Report," Astro-nautics and Aeronautics, March 1968, pp 56-65.
- Rango, A. and A. T. Anderson, 1973, "ERTS-1 Flood Hazard Studies in the Mississippi River Basin," Third Earth Resources Technology Satellite-1 Symposium, Vol. 1, Section B, NASA, Goddard Space Flight Center, Greenbelt. Md. pp 1127-1166.
- Rango, A., 1975, "Operational Applications of Satellite Snowcover Observations Project", Proceedings of the Tenth International Symposium on Remote Sensing of the Environment, 6-10 Oct. 1975, ERIM, U. of Michigan, Ann Arbor, Mich. pp 1367-1376.
- Rango, A. and V. V. Salomonson, 1977, "Seasonal Streamflow Estimation in the Himilayan Region Employing Meteorological Satellite Snow Cover Observations", Water Resources Research, Vol. 13, No. 1, pp 109-112.
- Rao, M. S. V., W. V. Abbott, J. S. Theon, 1976, "Satellite-Derived Global Oceanic Rainfall Atlas, (1973-1974), NASA SP-410, NASA, Wash., D.C. pp 184.

Schmugge, T., T. Wilheit, W. Webster, Jr., and P. Gloersen, 1976, "Remote Sensing of Soil Moisture with Microwave Radiometers-II" NASA TN D-8321, pp 34.

Schneider, S. H. and R. E. Dickinson, 1974, "Climate Modeling", Reviews of Geophysics and Space Physics, Vol. 12, No. 3, pp 447-493.

Schneider, J. R., 1976, "Guide for Designing RF Ground Receiving Stations for TIROS-N," NOAA Tech. Report NESS 75, U.S. Dept. of Commerce, NOAA, NESS, Wash., D.C. pp 75.

Schwalb, A. and J. Gross, 1969, "Vidicon Data Limitations", ESSA TM NESCTM 17, U.S. Dept. of Commerce, ESSA, NESC, Wash., D.C. pp 23.

Sellers, W. D (1965), "Physical Climatology". The University of Chicago Press/Chicago & London.

Short, N., P. D. Lowman, Jr., S. C. Freden, 1976, "Mission to Earth: LANDSAT Views the World", NASA SP 360, NASA, Wash., D.C. pp 459.

Smith, W. L., H. M. Woolf, P. G. Abel, C. M. Hayden, M. Chalfunt and N. Grody, 1974, "Nimbus 5 Sounder Data Processing System", NOAA Tech. Mem. NESS 57, pp 99.

Smith, W. L., J. Hickey, H. B. Howell, H. Jacobowitz, D. T. Hilleary and A. J. Drummond, 1977, "Nimbus-6 Earth Radiation Budget Experiment," Applied Optics, Vol. 16, No. 2, pp 306-318.

- Staff Members, Goddard Space Flight Center, 1976, "Nimbus G, Nimbus Observation Processing System (NOPS) Design Study Report", Goddard Space Flight Center, Greenbelt, Md., Jan. 1976, pp 100.
- Stoldt, N. W. and P. J. Havanac, 1973, "Compendium of Meteorological Satellites and Instrumentation", NSSDC 73-02, National Space Science Data Center, NASA, Goddard Space Flight Center, Greenbelt, Md., 20771, pp 285.
- Stumpf, H. G., 1974, "A Satellite-Derived Experimental Gulf Stream Analysis", Mariners Weather Log, Vol. 18, pp 149-152.
- Suomi, V. E., and T. H. Von der Haar, 1969, "Geosynchronous Meteorological Satellite", Journal of Spacecraft and Rockets, Vol. 6, No. 3, pp 342-344.
- Szekiela, K. H., 1976, "Spacecraft Oceanography", Oceanogr. Mar. Biol. Ann. Rev., Vol. 14, pp 99-166.
- U.S. Dept. of Commerce 1976, "The Federal Plan for Meteorological Services and Supporting Research", NOAA, Wash., D.C. pp 52.
- Valley, S. L., ed. (1965), "Handbook of Geophysics and Space Environments". Air Force Cambridge Research Laboratory, Bedford, Mass.
- Wiesnet, D. and M. Matson, 1975, "Monthly Winter Snow Line Variation in the Northern Hemisphere from Satellite Records," NOAA Tech. Memo. NESS 74, pp 21.

- World Meteorological Organization, 1975, "World Weather Watch, Global Observing System-Satellite Sub-System" WMO, No. 411, Secretariat of the WMO, Geneva, Switzerland, pp 51.
- Yates, H. W. and W. R. Bandeen, 1975, "Meteorological Applications of Remote Sensing from Satellites," Proc. of the IEEE, Vol. 63, No. 1, 148-163.
- Zwally, H. J., T. T. Wilheit, P. Gloersen, J. L. Mueller, 1976, "Characteristics of Antarctic Sea Ice as Determined by Satellite-borne Microwave Imagers", Proceedings of the Symposium on Meteorological Observations from Space, Their Contributions to the First GARP Experiment, Boulder, Col., NCAR pp 94-97.

TABLE 1
Major Atmospheric Windows Available for Spacecraft Remote Sensing

ULTRAVIOLET AND VISIBLE	0.30-0.75 μm 0.77-0.91
NEAR-INFRARED	1.0-1.12 1.19-1.34 1.55-1.75 2.05-2.4
MID-INFRARED	3.5-4.16 4.5-5.0
THERMAL INFRARED	8.0-9.2 10.2-12.4 17.0-22.0
MICROWAVE	2.06-2.22 mm 3.0-3.75 7.5-11.5 20.0+

From Lintz and Simonett (1976)

TABLE 2

Satellite	Launch	Ceased Operation	Remarks
TIROS 1	04/01/60	06/15/60	First cloud cover imaging in the visible (Vidicon).
TIROS 2	11/23/60	02/07/61	First multispectral imaging in the visible and infrared.
TIROS 3	07/12/61	10/30/61	
TIROS 4	02/08/62	06/12/62	
TIROS 5	06/19/62	05/05/63	
TIROS 6	09/18/62	10/11/63	
TIROS 7	06/19/63	02/03/66	
TIROS 8	12/21/63	01/22/66	First Automatic Picture Transmission (APT)
Nimbus 1	08/28/64	09/23/64	Carried Advanced Vidicon Camera System (AVCS), APT, and High Resolution Infrared Radiometer (HRIR) for night coverage.
TIROS 9	01/22/65	02/15/67	First TIROS satellite in sun-synchronous orbit.
TIROS 10	07/01/65	07/31/66	
ESSA 1	02/03/66	05/08/67	First operational weather satellite; carried 2 wide-angle TV cameras.
ESSA 2	02/28/66	10/16/70	Carried APT cameras; APT carried on all even-numbered ESSA satellites.
Nimbus 2	05/15/66	11/15/66	First direct-readout of HRIR. Carried Medium Resolution Infrared Radiometer (MRIR).
ESSA 3	10/02/66	10/19/68	Carried first operational AVCS cameras; AVCS carried on all odd-numbered ESSA satellites.
ATS 1	12/06/66	10/16/72	Carried first Spin Scan Cloud Camera (SSCC), continuously imaging in visible.
ESSA 4	01/26/67	06/19/67	
ESSA 5	04/20/67	02/20/70	
ATS 3	11/05/67	10/30/75	Carried first Multi-color Spin Scan Cloud Camera (MSSCC).
ESSA 6	11/10/67	11/04/69	
ESSA 7	08/16/68	07/19/69	
ESSA 8	12/15/68	--	
ESSA 9	02/26/69	11/29/73	
Nimbus 3	04/14/69	09/25/70	First vertical sounding of the atmosphere (SIRS, IRIS), data collection and location (IRLS), and solar UV monitoring (MUSE). Also carried MRIR.
ITOS 1	01/23/70	06/17/71	Second generation operational prototype (Improved TIROS Operational Satellite).
Nimbus 4	04/08/70	--	First vertical sounding to 60 km (SCR) and ozone sounding globally (BUV).
NOAA 1	12/11/70	08/19/71	First NOAA-funded second generation operational satellite.
Landsat 1	07/23/72	--	First Earth resources technology satellite
NOAA 2	10/15/72	01/30/75	First operational satellite to carry visible and IR Scanning Radiometer (SR) and Vertical Temperature Profile Radiometer (VTPR).
Nimbus 5	12/12/72	--	First passive microwave sounder (NEMS) and imager (ESMR) flown.
NOAA 3	11/06/73	--	First operational satellite to permit direct broadcast of VTPR data.
SMS 1	05/17/74	--	First Synchronous Meteorological Satellite (GOES prototype). Carried visible and IR imaging radiometer.
ATS 6	05/30/74	--	First three-axis-stabilized geostationary satellite. (Infrared and visible scanner failed on 8/15/74.)
NOAA 4	11/15/74	--	
Landsat 2	01/22/75	--	
SMS 2	02/06/75	--	Second operational geostationary SMS/GOES prototype.
Nimbus 6	06/12/75	--	First sounder including 4.3um CO ₂ band flown (HIRS). First measurement of Earth radiation budget at synoptic/planetary scales (ERB).
GOES 1	10/16/75	--	First Geostationary Operational Environmental Satellite.
NOAA 5	07/29/76	--	

TABLE 3

TIROS-N Instrumentation

Instrument	Channels	Resolution km	Swath Width km	Instr. Observ.	Climate Parameters
ERBSI (proposed)	2-50 μm 0.2-5 μm	1000,87	3000	Visible and IR wide field & scanner	Earth radiation budget
SBUV (proposed)	12 channels 2550-3440 Å	165	Nadir only	Ultraviolet backscatter	Ozone profile, total ozone
AVHRR/3	.58-.68 μm .725-1.0 1.53-1.73 3.55-3.93 10.3-11.3 11.5-12.5	1	3000	Visible and IR imaging	Sea surface temp. snow cover, albedo, clouds, vegetation cover, ice sheets
TOVS -- 3 Instruments					
HIRS	20 channels	30	1000	Multispectral IR radiation	Temp. profiles, humidity profiles
SSU	3 channels 668 cm^{-1}	147	1450	Selective absorp- tion of CO_2	Stratosphere tempera- ture profiles
MSU	4 channels 5.5 mm	100	1700	Passive microwave radiance	Temperature profiles
ARGOS -- Data collection and position location for surface sensors					

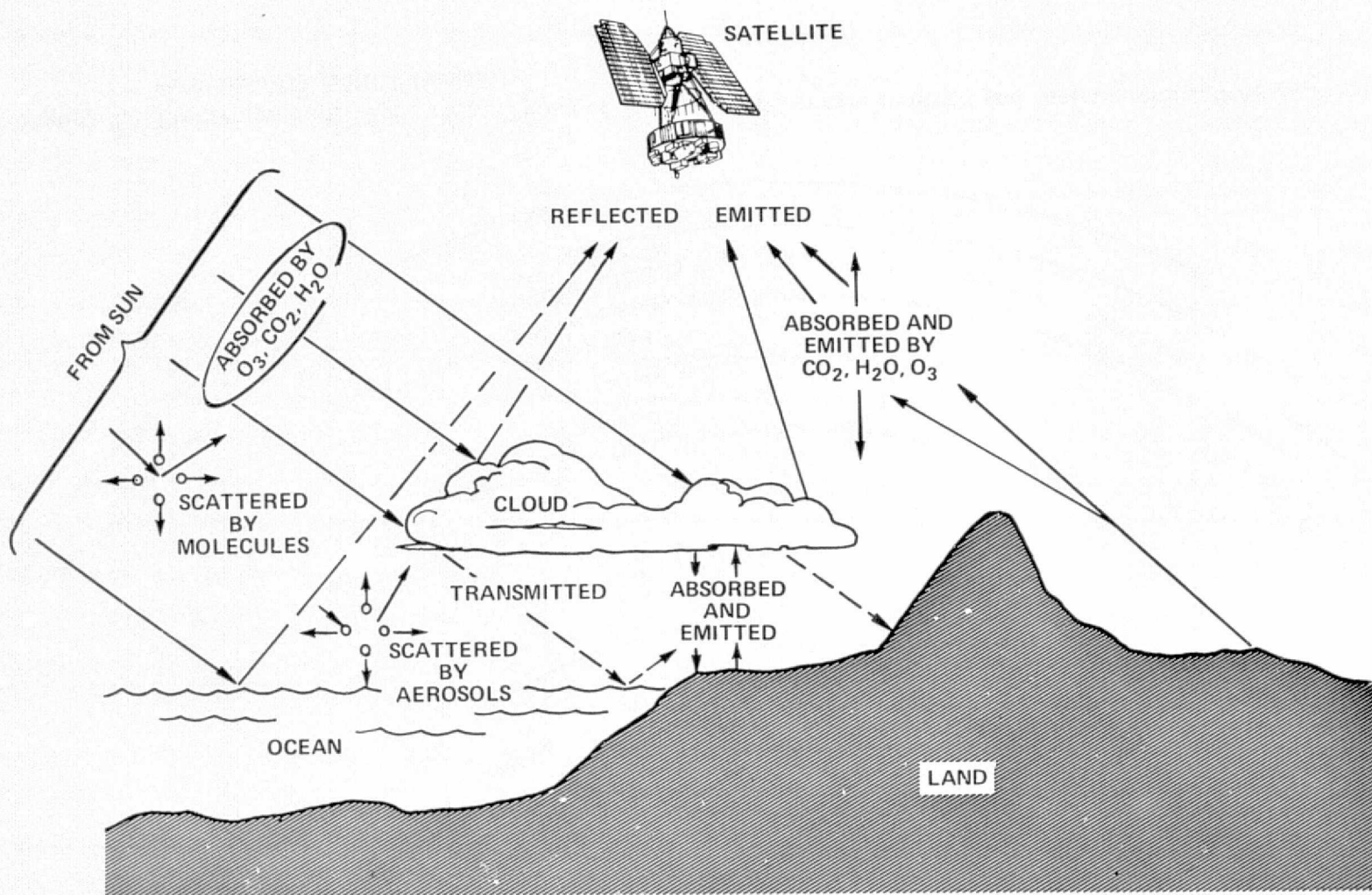


Figure 1. A Schematic Illustration of Earth-Sun-Satellite Radiative Interactions

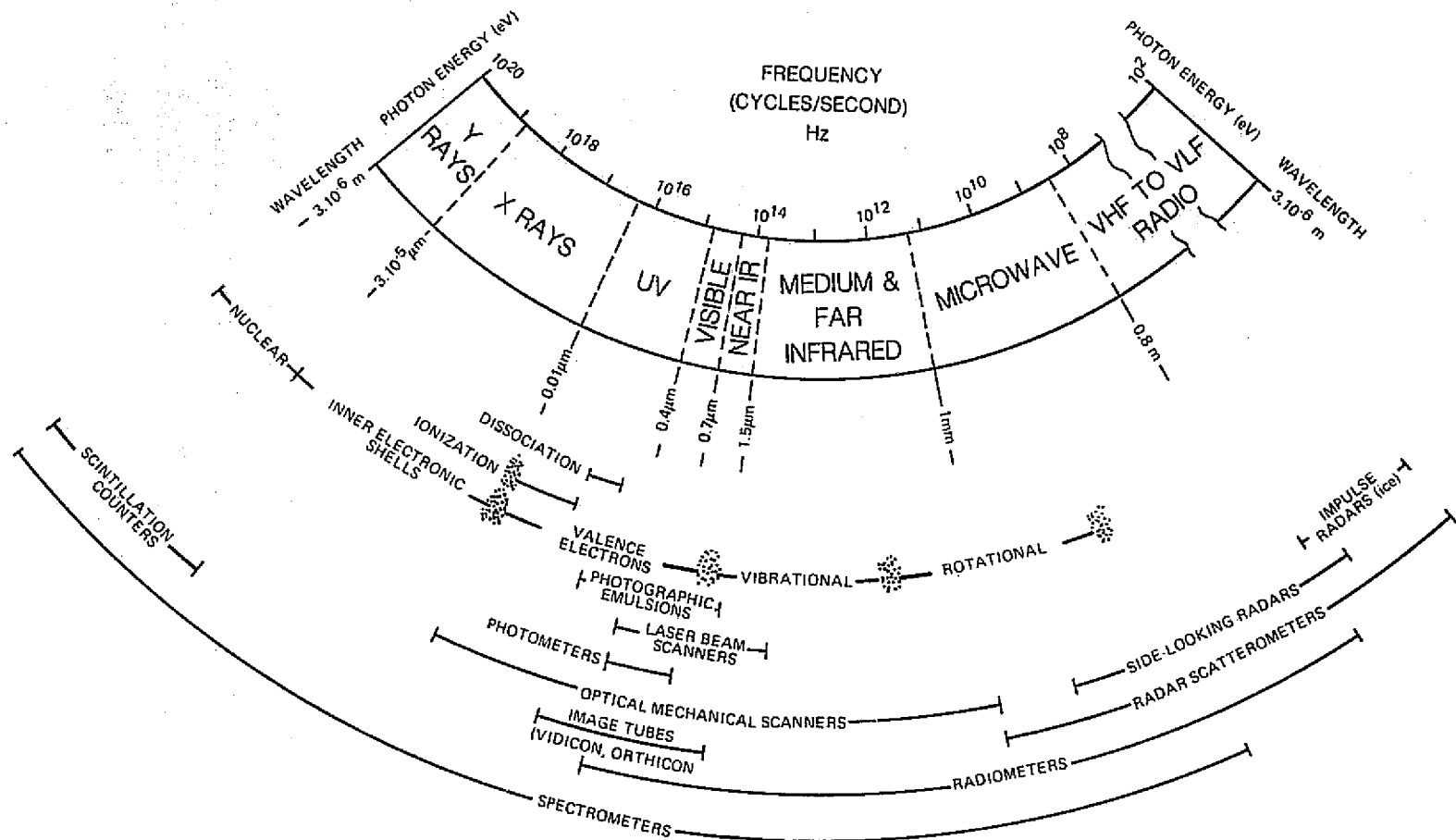


Figure 2. Electromagnetic Spectrum, Types of Physical Processes Involved and Instrumentation Associated with Specific EMR Intervals

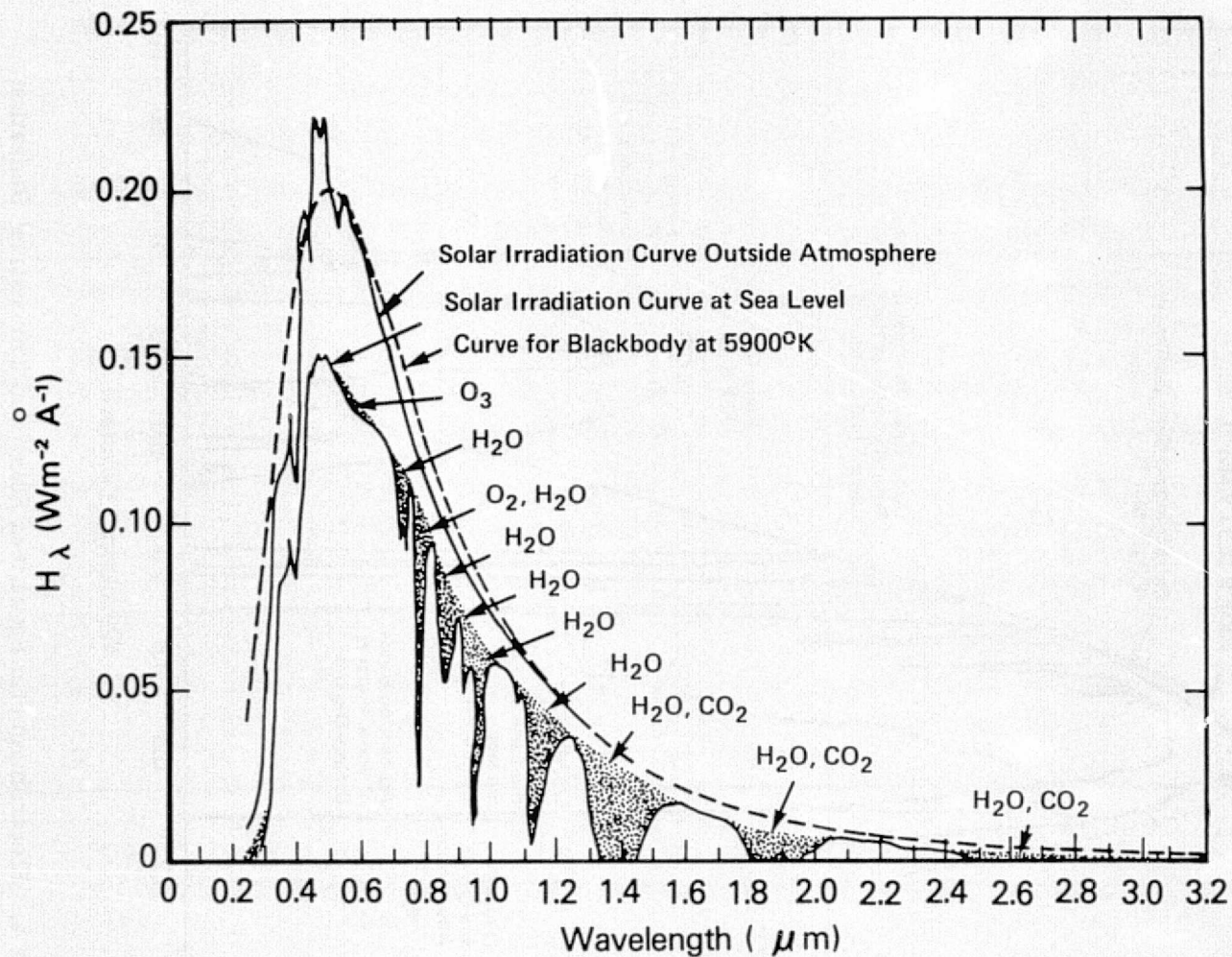


Figure 3. Spectral Irradiance (H_{λ}) of Direct Sunlight Before and After it Passes Through the Earth's Atmosphere. The Stippled Portion Gives the Atmospheric Absorption; the Sun is at Zenith :Valley, 1965)

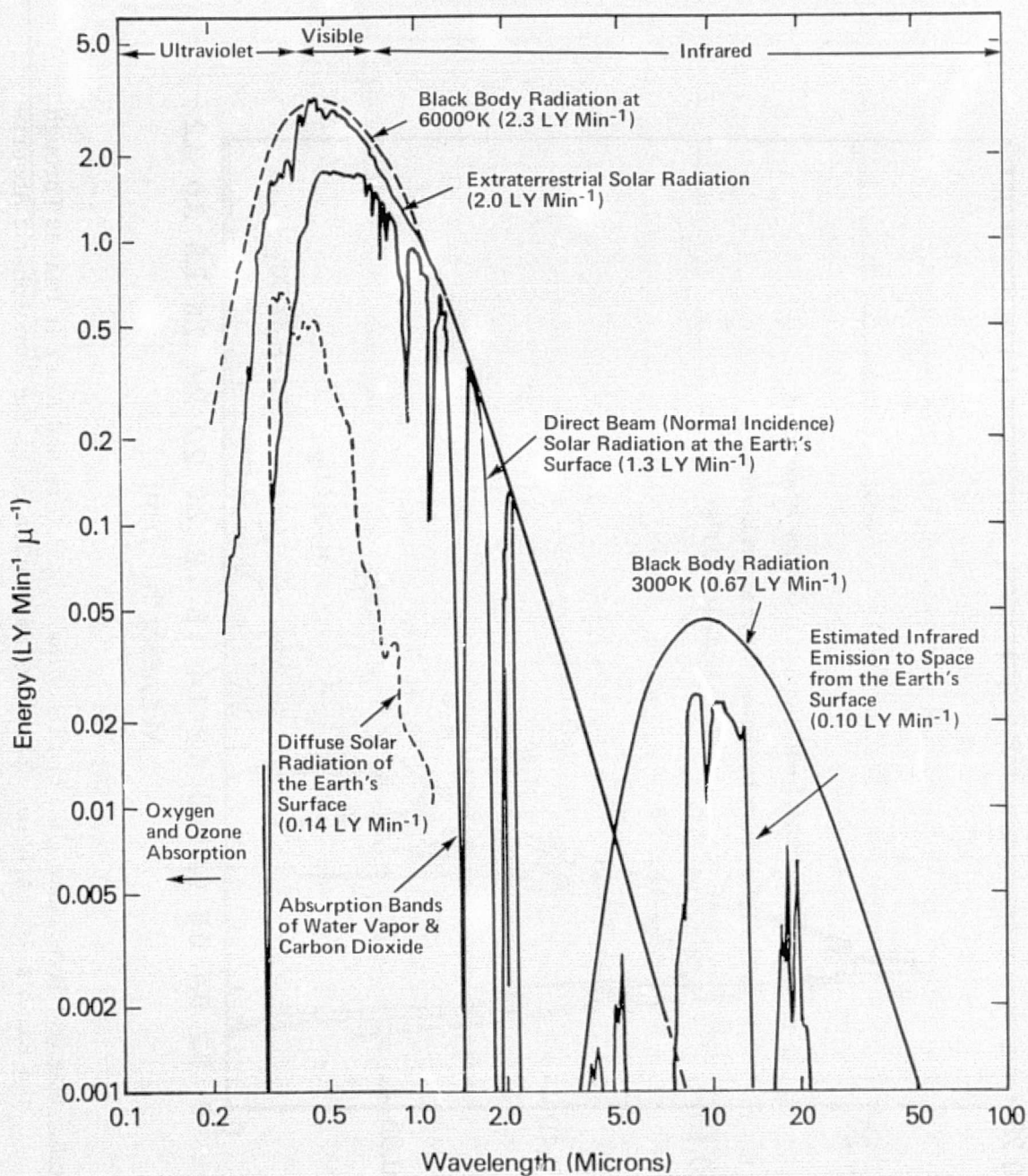


Figure 4. Electromagnetic Spectra of Solar and Terrestrial Radiation (Sellers, 1965)

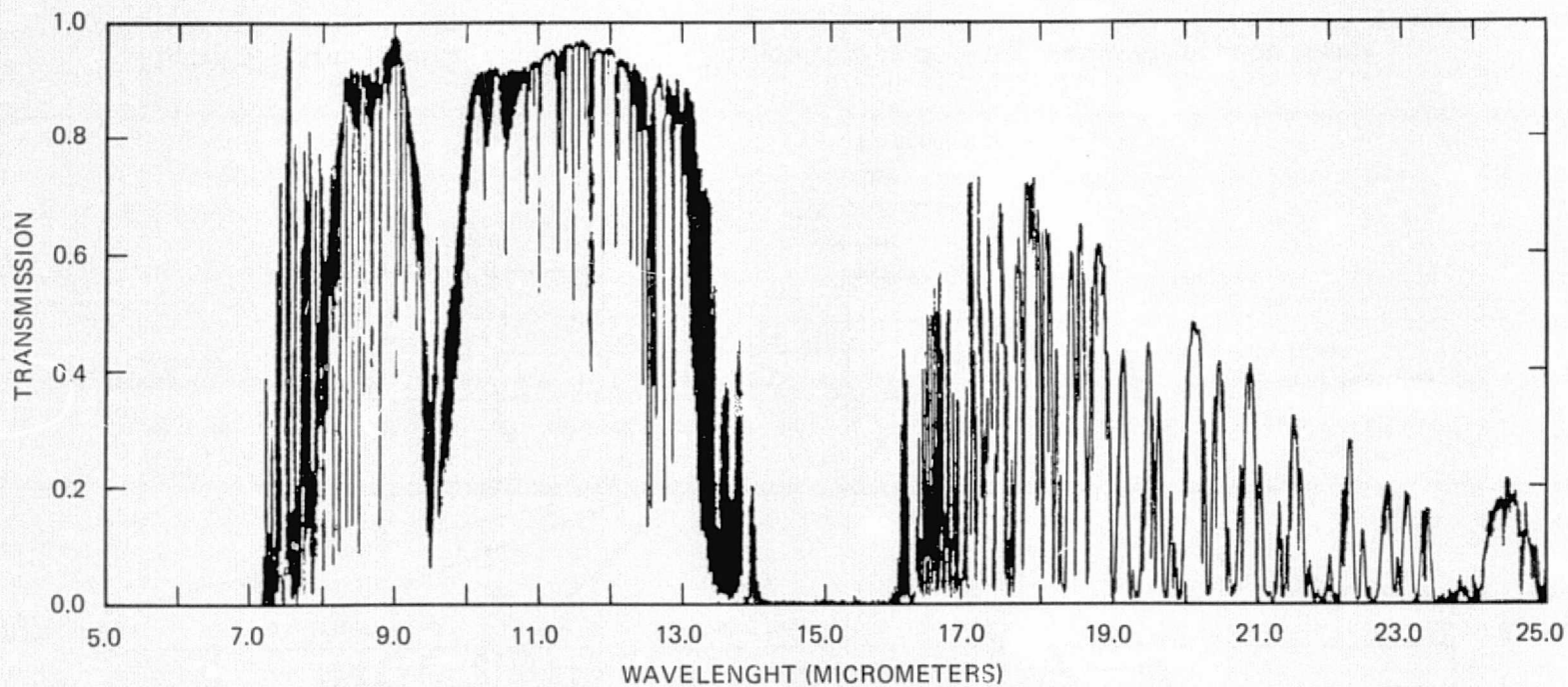


Figure 5. Measured Transmittances Through the Atmosphere for the 5 to 25 μm Region (Kunde, 1976)

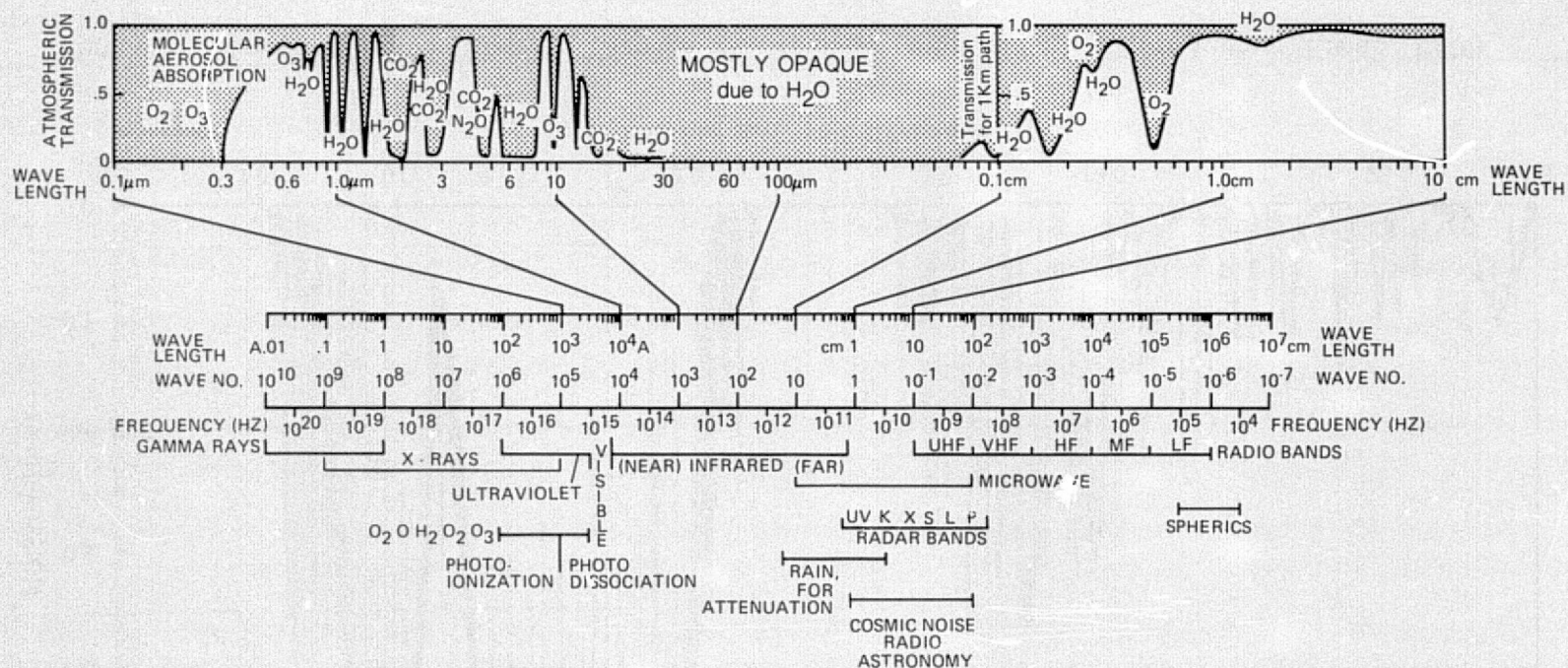


Figure 6. Atmospheric Transmission Characteristics Showing Major Absorption Bands

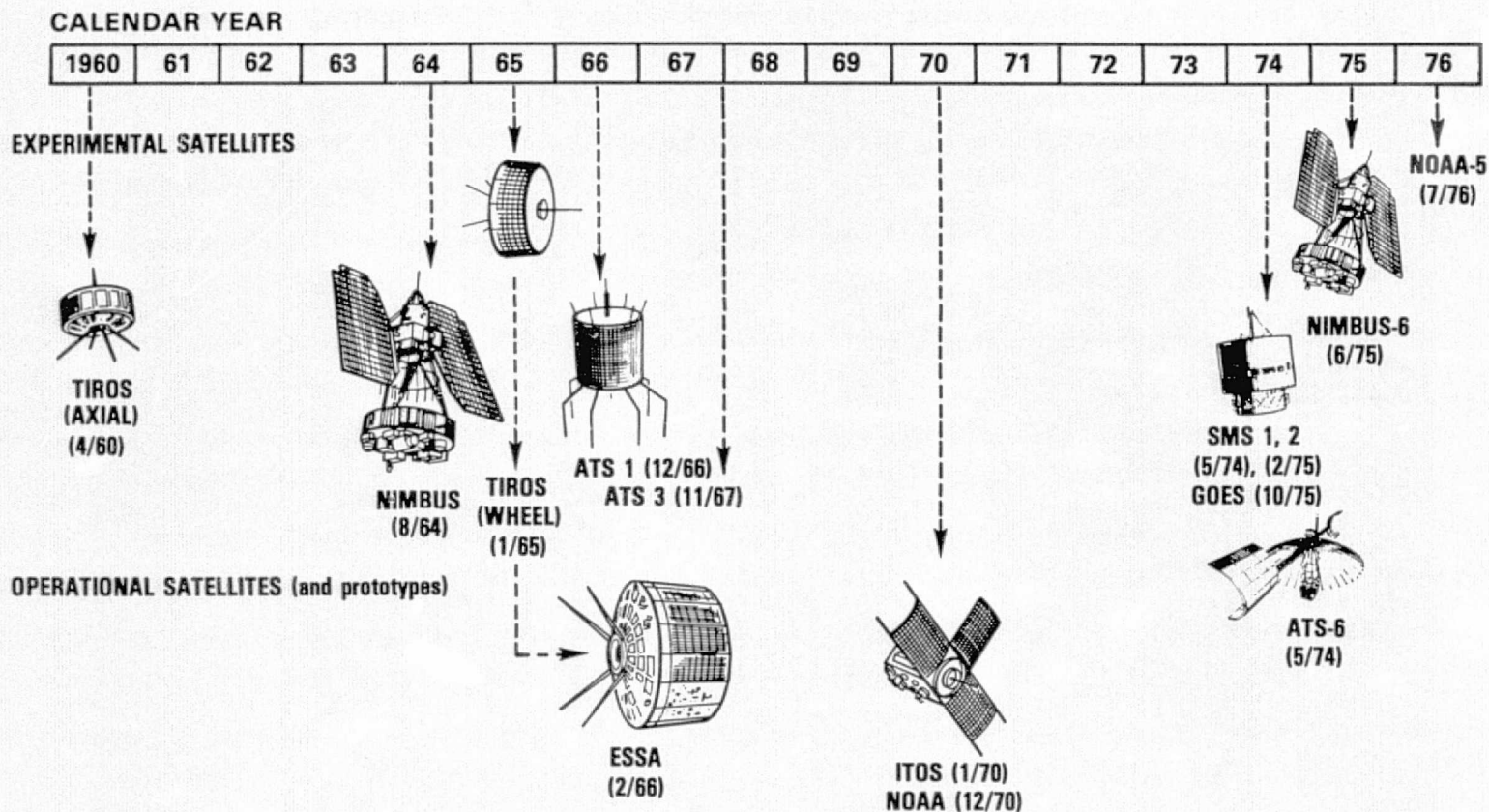


Figure 7. An Artist's Conception of the U.S. Meteorological Satellite Program From 1960 to 1976

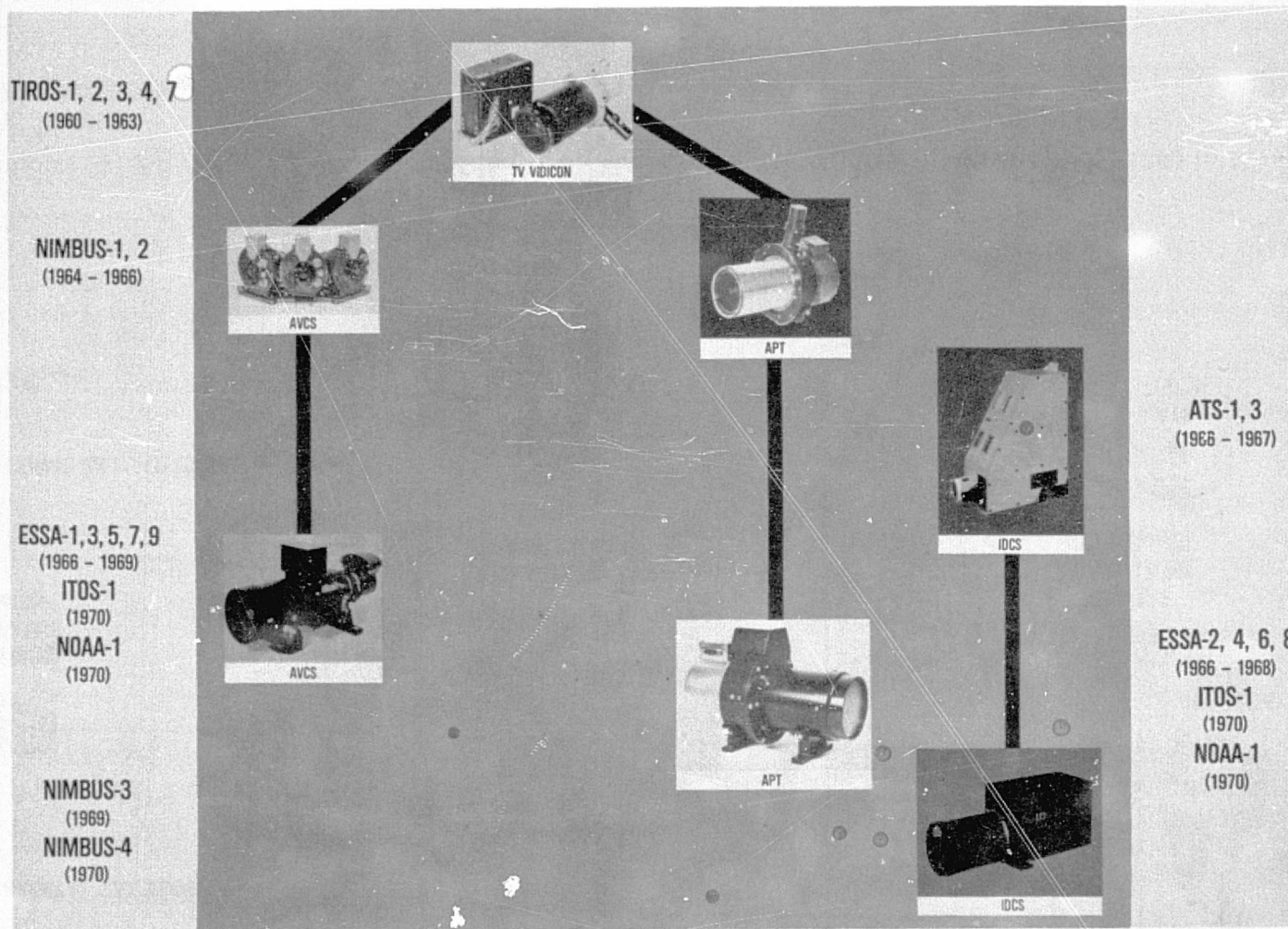


Figure 8. Evolution of U.S. Meteorological Satellite Camera Systems from 1960 to 1970

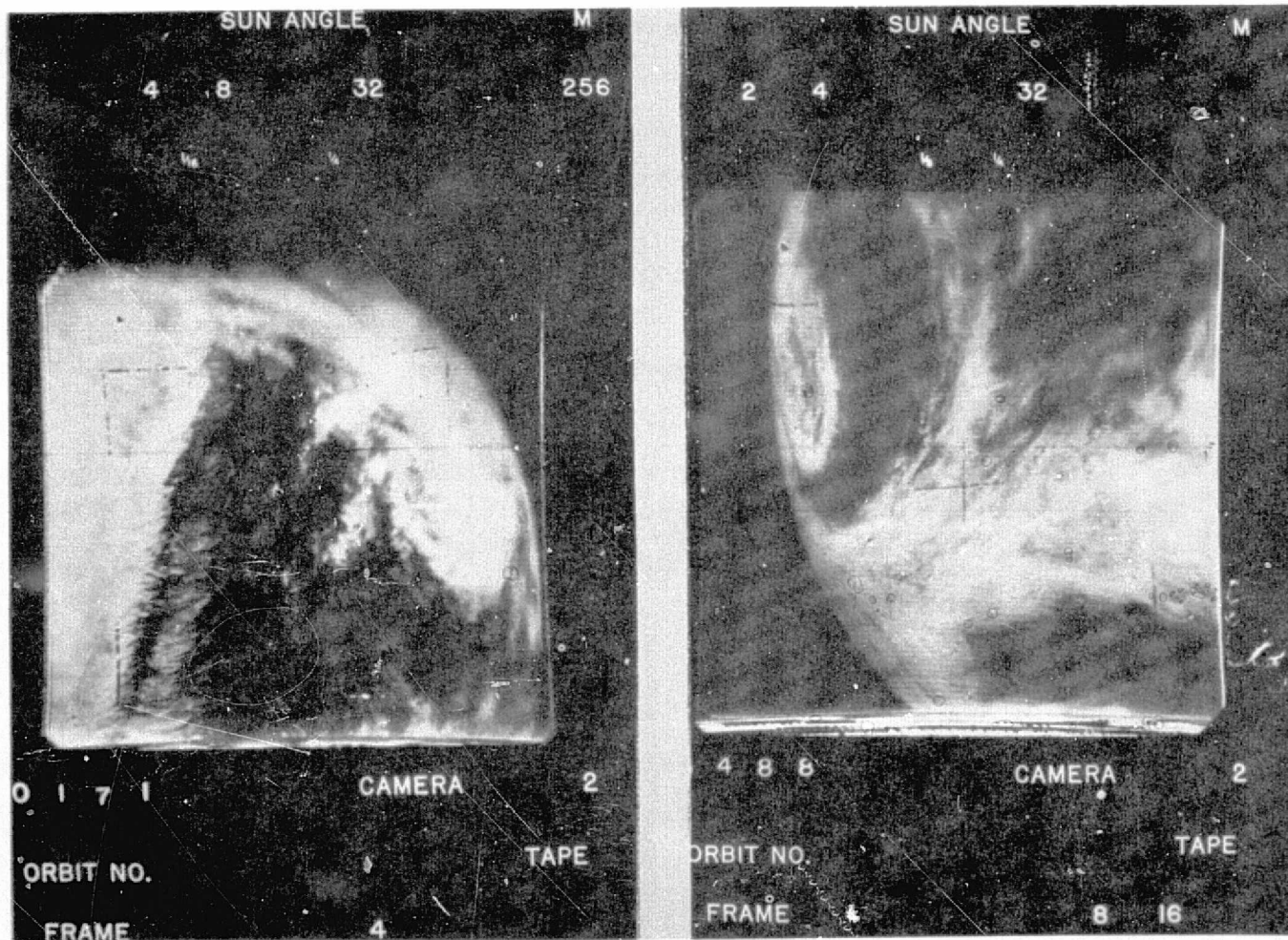


Figure 9. Examples of Early TIROS 1 (1960) Television Pictures

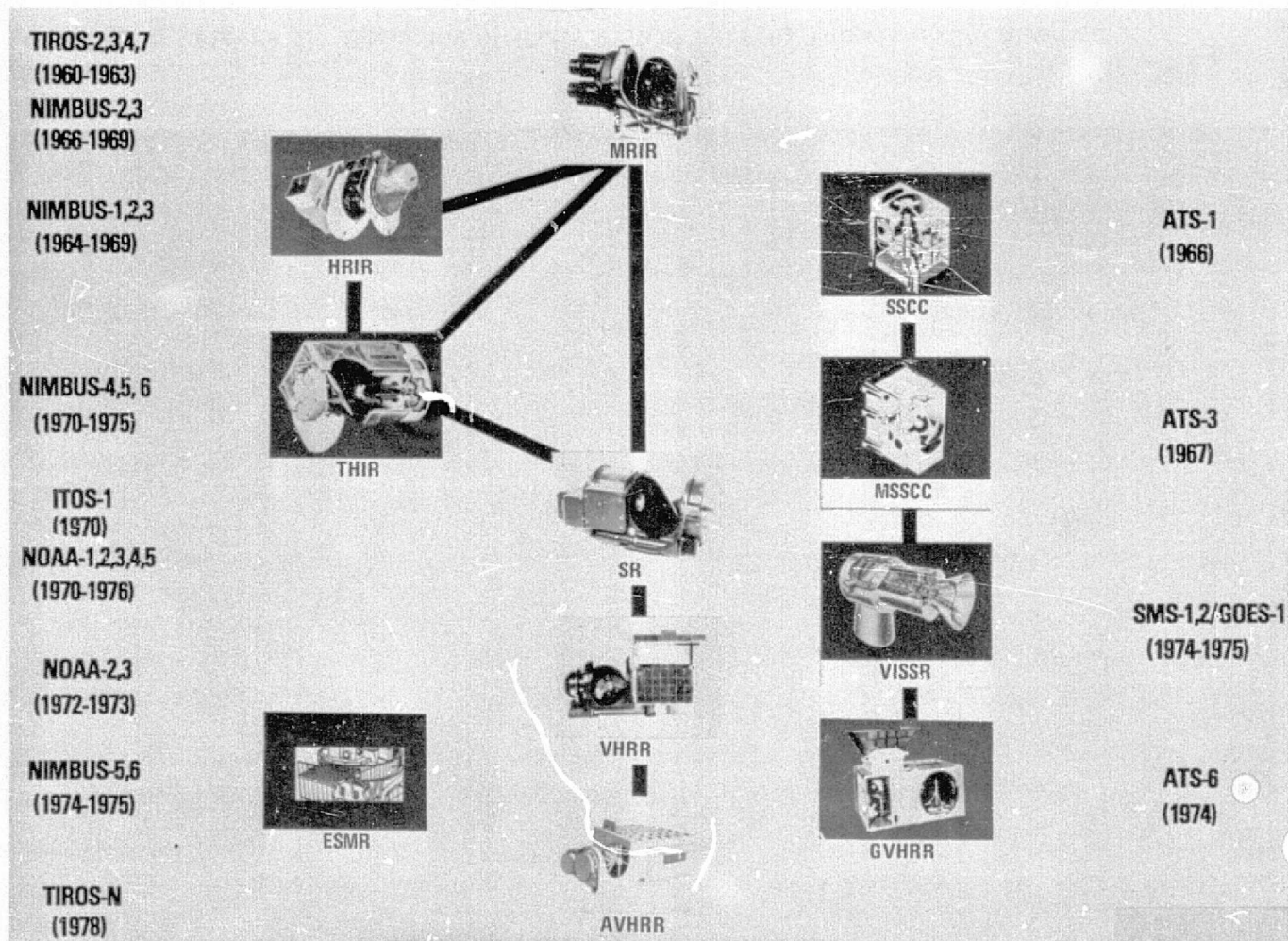
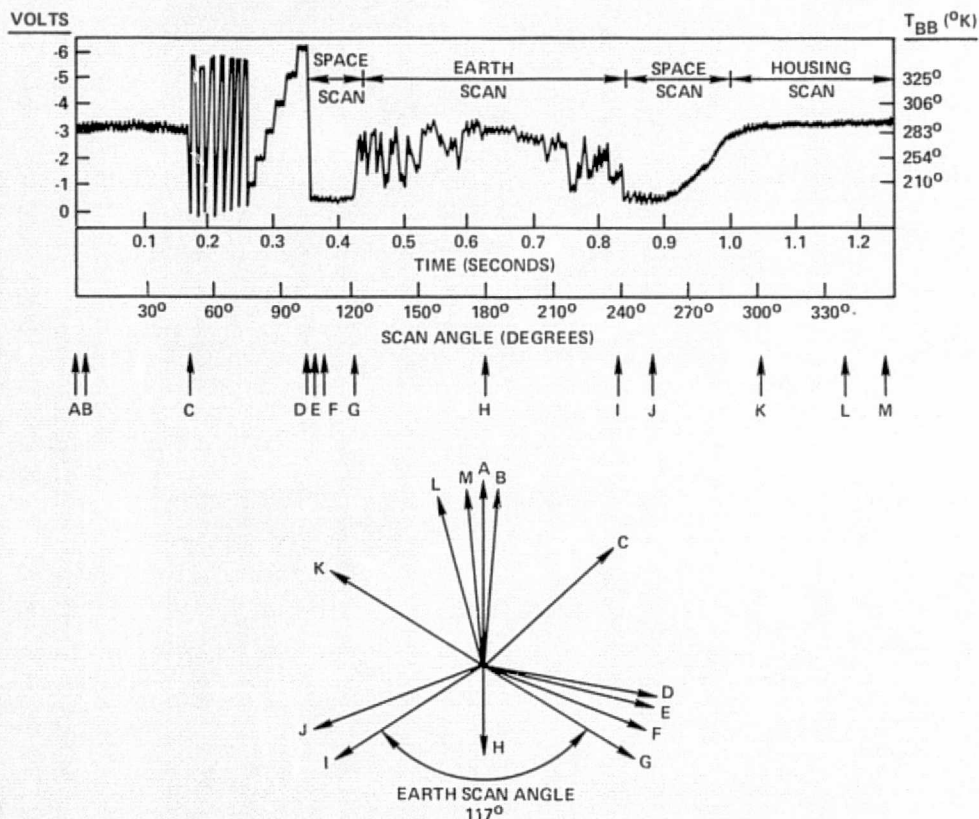


Figure 10. Evolution of U.S. Meteorological Satellite Scanner Systems from 1960 to 1978



LEGEND

REFERENCE LETTER	ANGLE (DEGREES)	TIME (MSEC)	EVENT
A:	0°	0	SPACECRAFT ZENITH
B:	5°	17.4	RADIOMETER IFOV JUST STARTING TO LEAVE HOUSING.
C:	48°	166.7	SCAN MIRROR POSITION PIP NO. 1 OCCURS AND RADIOMETER SYNC WORD AND CALIBRATION SIGNAL SEQUENCE IS STARTED. 6.7 MICRON CHANNEL GAIN RETURNED TO NORMAL.
D:	100°	347.5	RADIOMETER IFOV JUST STARTING TO SEE ALL OF SPACE.
E:	103.5°	359.4	CALIBRATE SIGNAL SEQUENCE ENDS AND RESTORE PERIOD STARTS.
F:	110.7°	384.4	RESTORE PERIOD ENDS
G:	121.5°	422.2	EARTH SCAN PERIOD BEGINS (600-NM! ORBIT)
H:	180°	625.0	SPACECRAFT NADIR
I:	238.5°	828.8	EARTH SCAN PERIOD ENDS (600-NM! ORBIT)
J:	250°	868.9	RADIOMETER IFOV JUST STARTING TO SEE HOUSING
K:	302°	1048.5	SCAN MIRROR POSITION PIP NO. 2 OCCURS AND 6.7 MICRON CHANNEL GAIN IS ATTENUATED BY A FACTOR OF 3.
L:	345°	1197.9	RADIOMETER IFOV COMPLETELY FILLED BY HOUSING
M:	355°	1232.6	RADIOMETER Z-AXIS

Figure 11. Nimbus 5 THIR (11 μ m) Scan Sequence

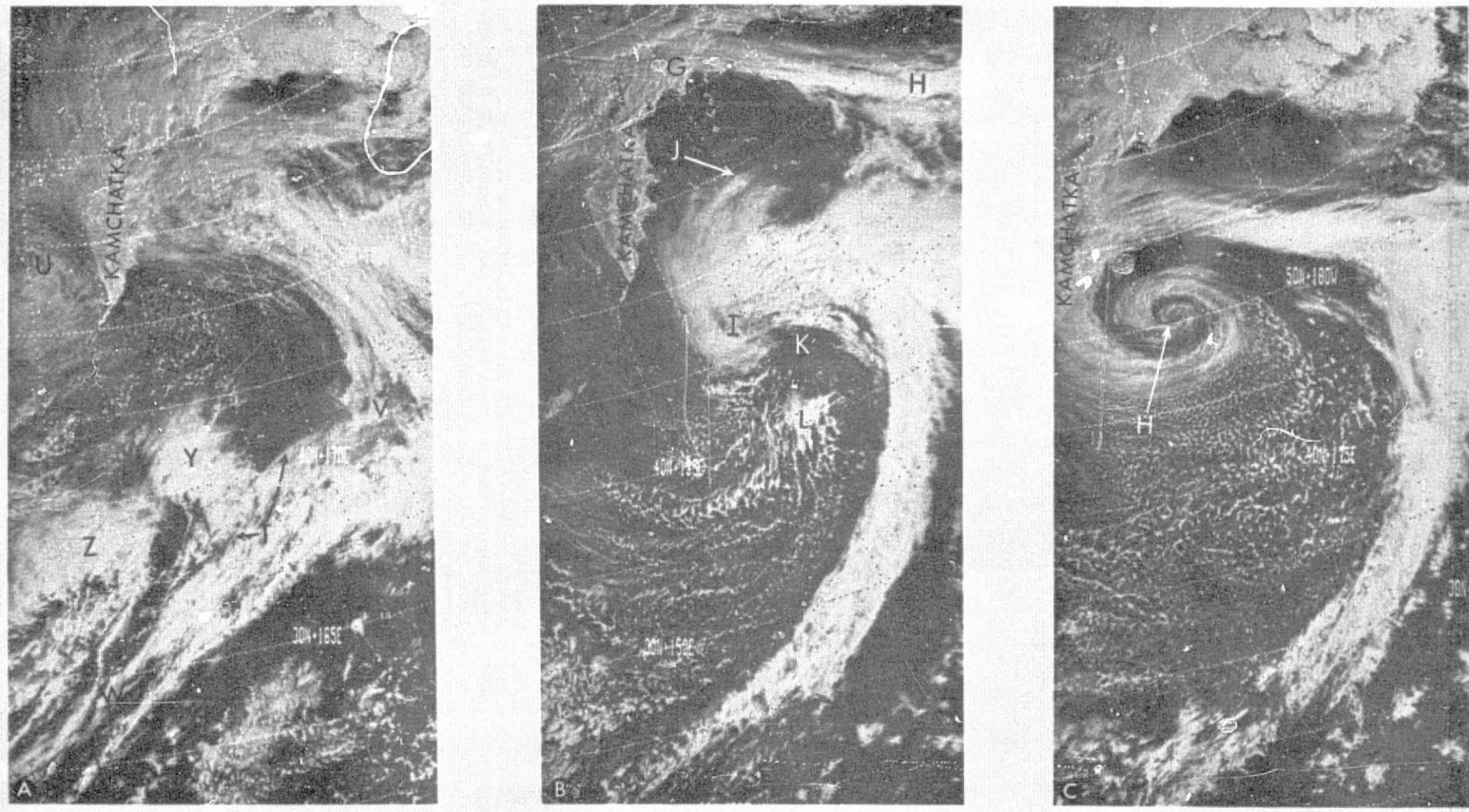


Figure 12. Development of a Pacific Storm Using NOAA 2 Visible Scanning Radiometer Data. A) Initial Frontal Wave, Orbit 6426, 2214 GMT, 12 March 1974. Y, Z are Vorticity Centers Close to a Front, T is a Developing Wave. B) Deepening Stage, Orbit 6439, 2307 GMT 13 March 1974. I is Main Storm System, J is Cirrus Outflow South of Aleutians, (G to H), K is Dry Air Behind Front, L is Cloudiness of Secondary Vorticity Center. C) Decaying Stage, Orbit 6451, 2209 GMT, 14 March 1974. H is Fully Occluded, Mature Storm Stage. Cold Dry Air Present in Vortex Center. (Johnson et al., 1976)

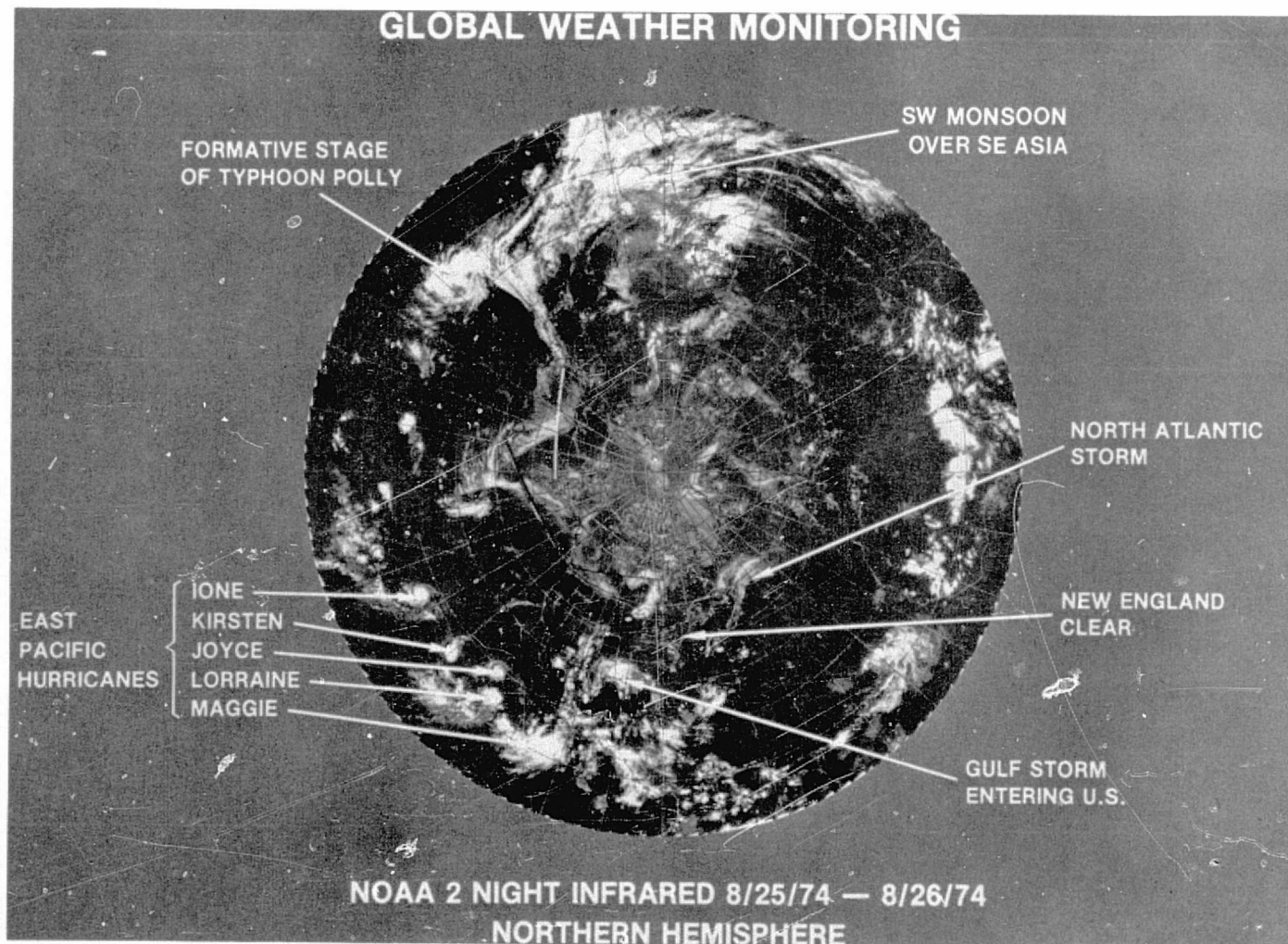


Figure 13. A Global Montage of Nighttime Infrared Data from NOAA-2 SR (10.5 to 12.5 μm) for the Northern Hemisphere 8/25/74 to 8/26/74

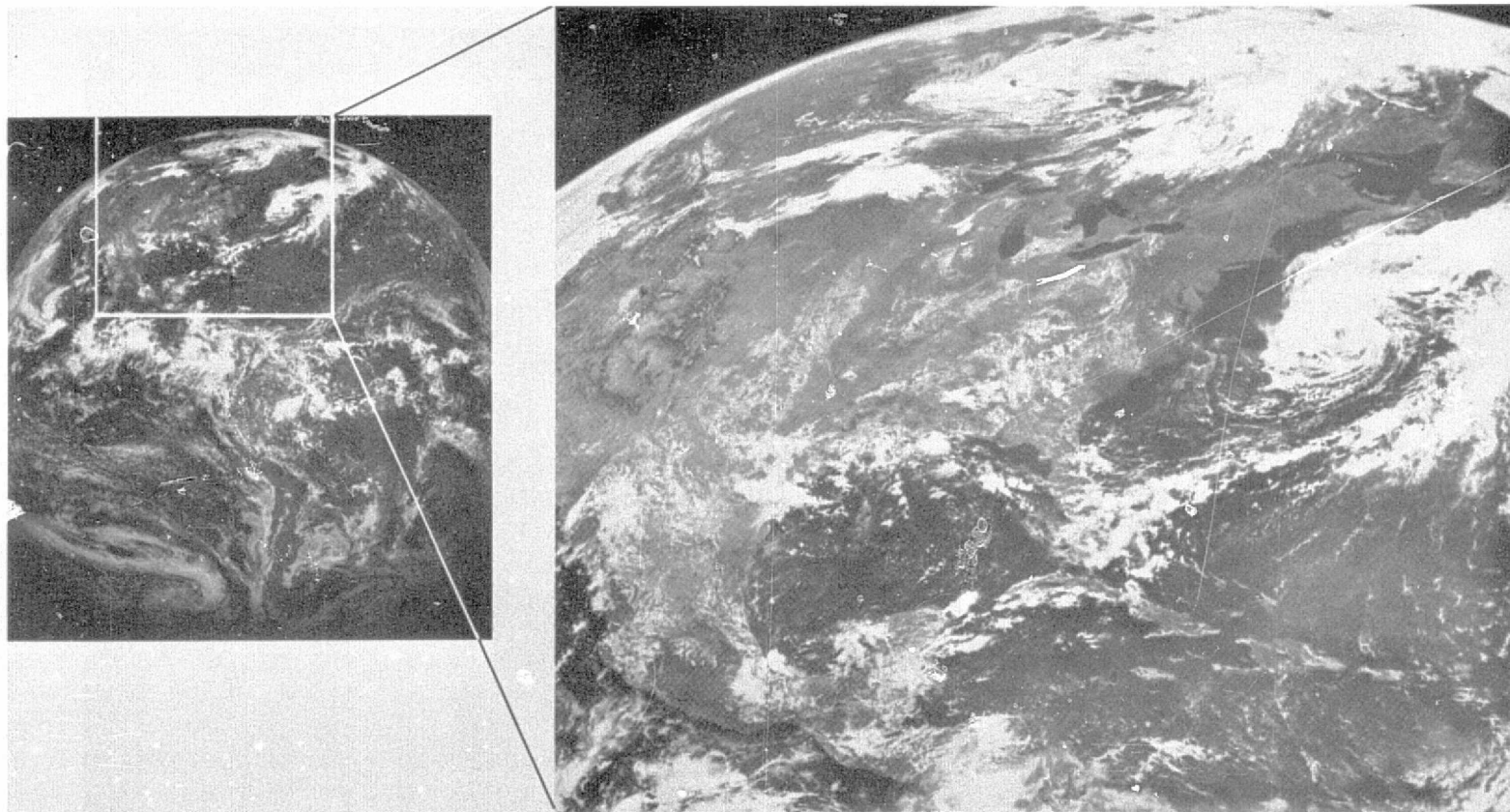


Figure 14. SMS-1 Visible Image, 1 n mile Resolution, June 30, 1975 with sector of the United States, Caribbean and Hurricane Amy off the U. S. East Coast.

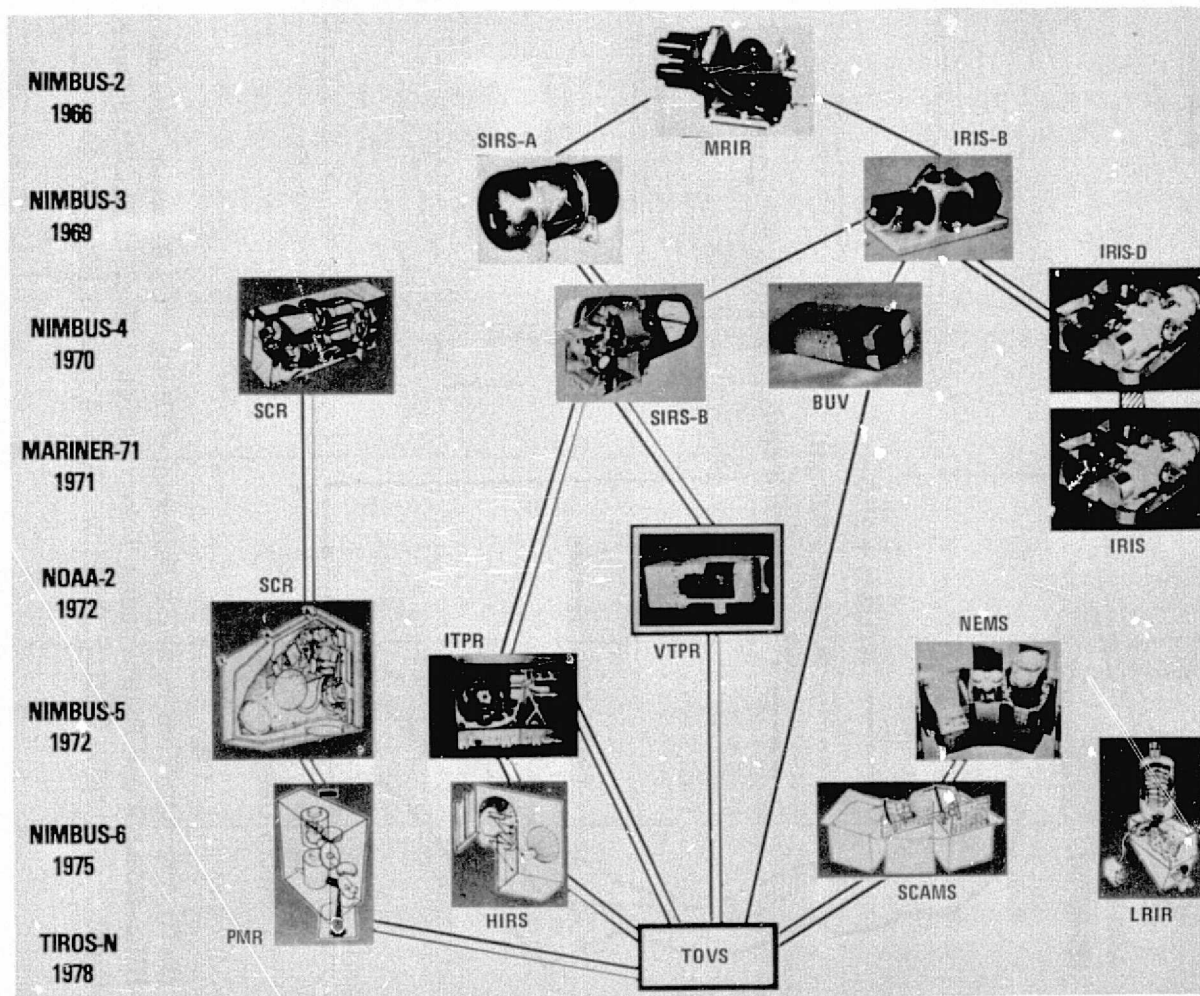


Figure 15. Evolution of Meteorological Atmospheric Sounders from 1966 to 1978

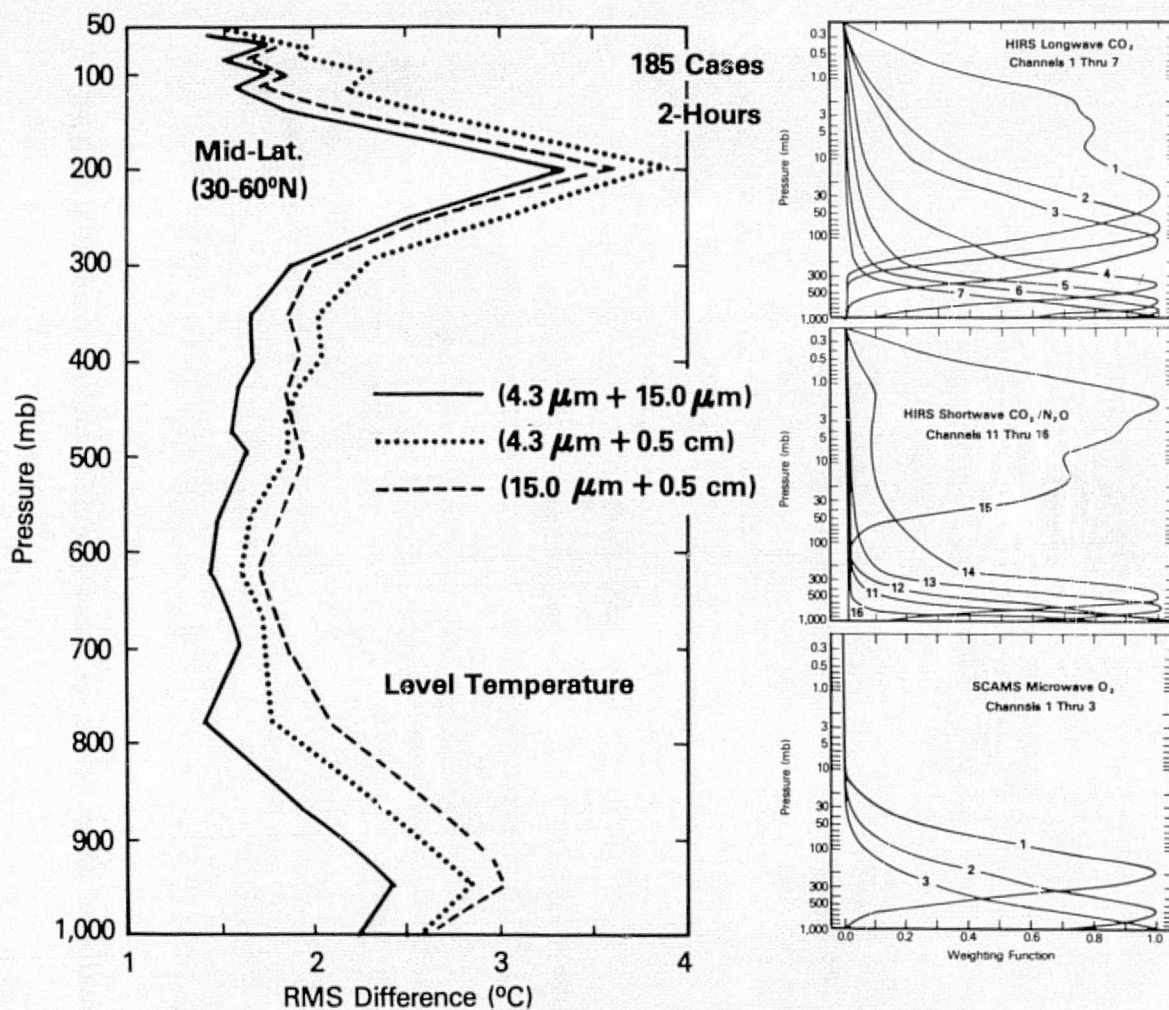


Figure 16. (Left) Average Temperature Difference (RMS, °C) Between Nimbus 6 HIRS-SCAMS and Radiosondes Taken Within 2 Hrs. of Satellite Over-flight. (Right) Weighting Functions for Nimbus 6 HIRS-SCAMS

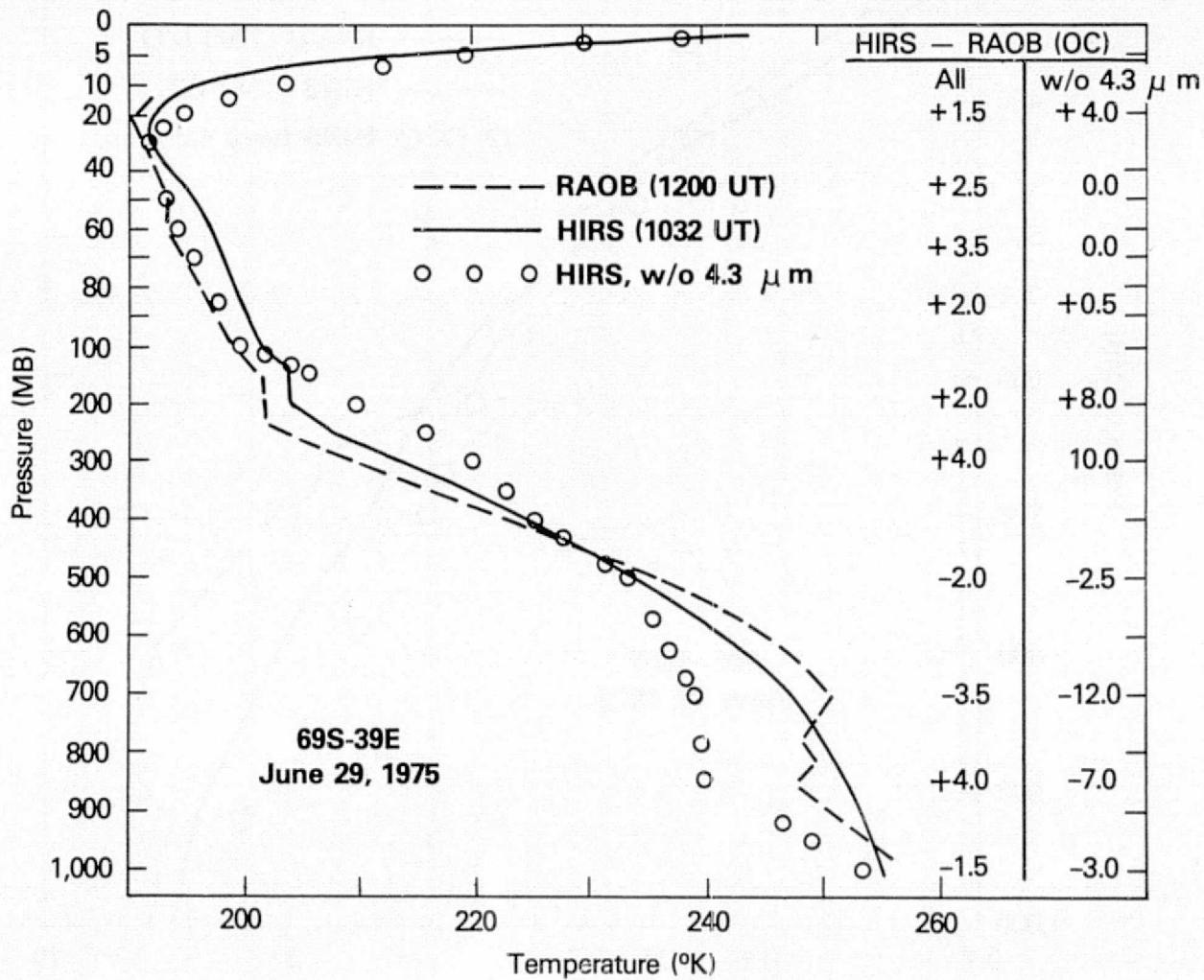


Figure 17. Comparison of Nimbus 6 HIRS and Radiosonde Temperature Profile on 29 June 1975

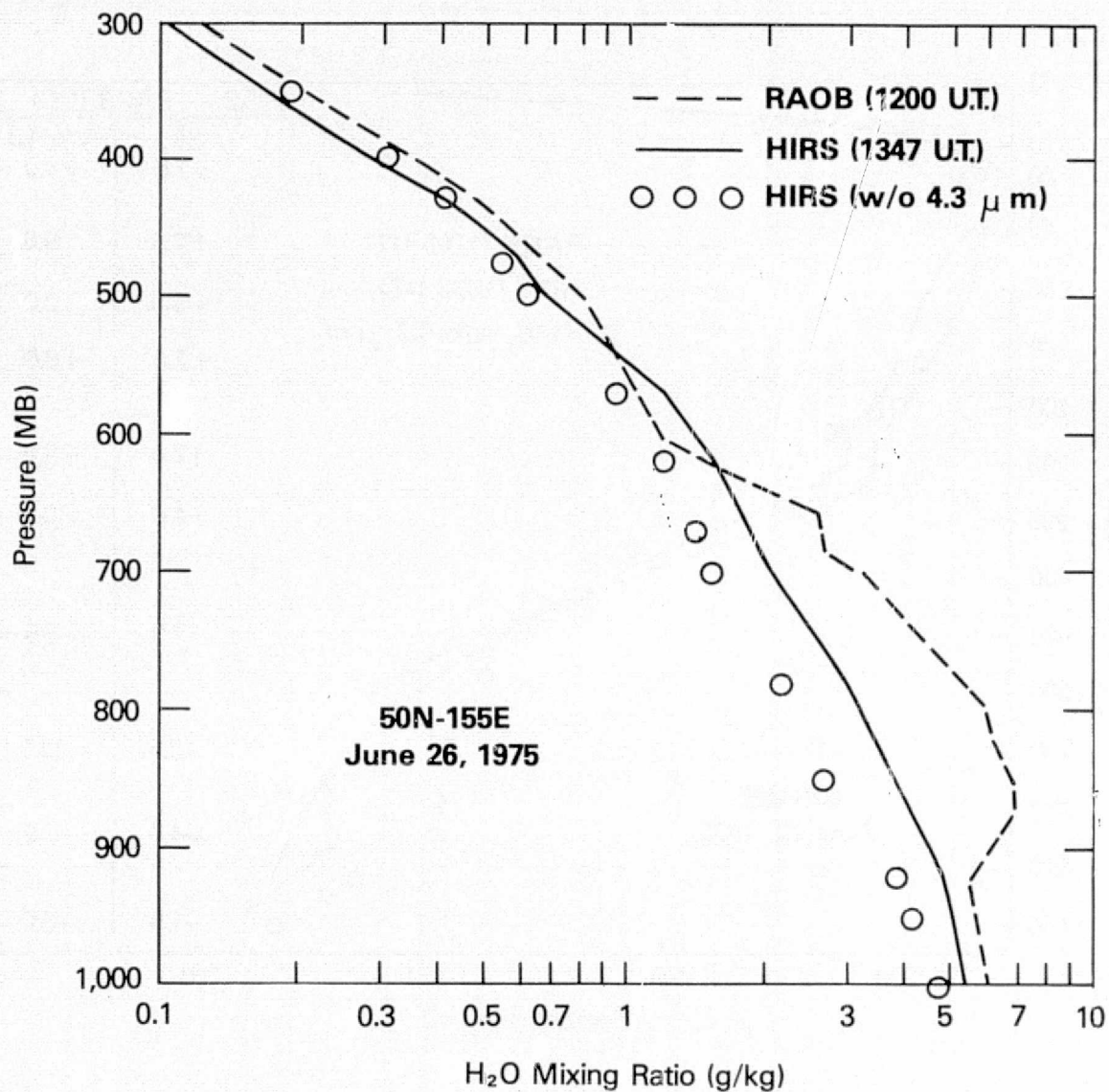


Figure 18. Comparison of Nimbus 6 HIRS and Radiosonde Water Vapor Profile on 26 June 1975

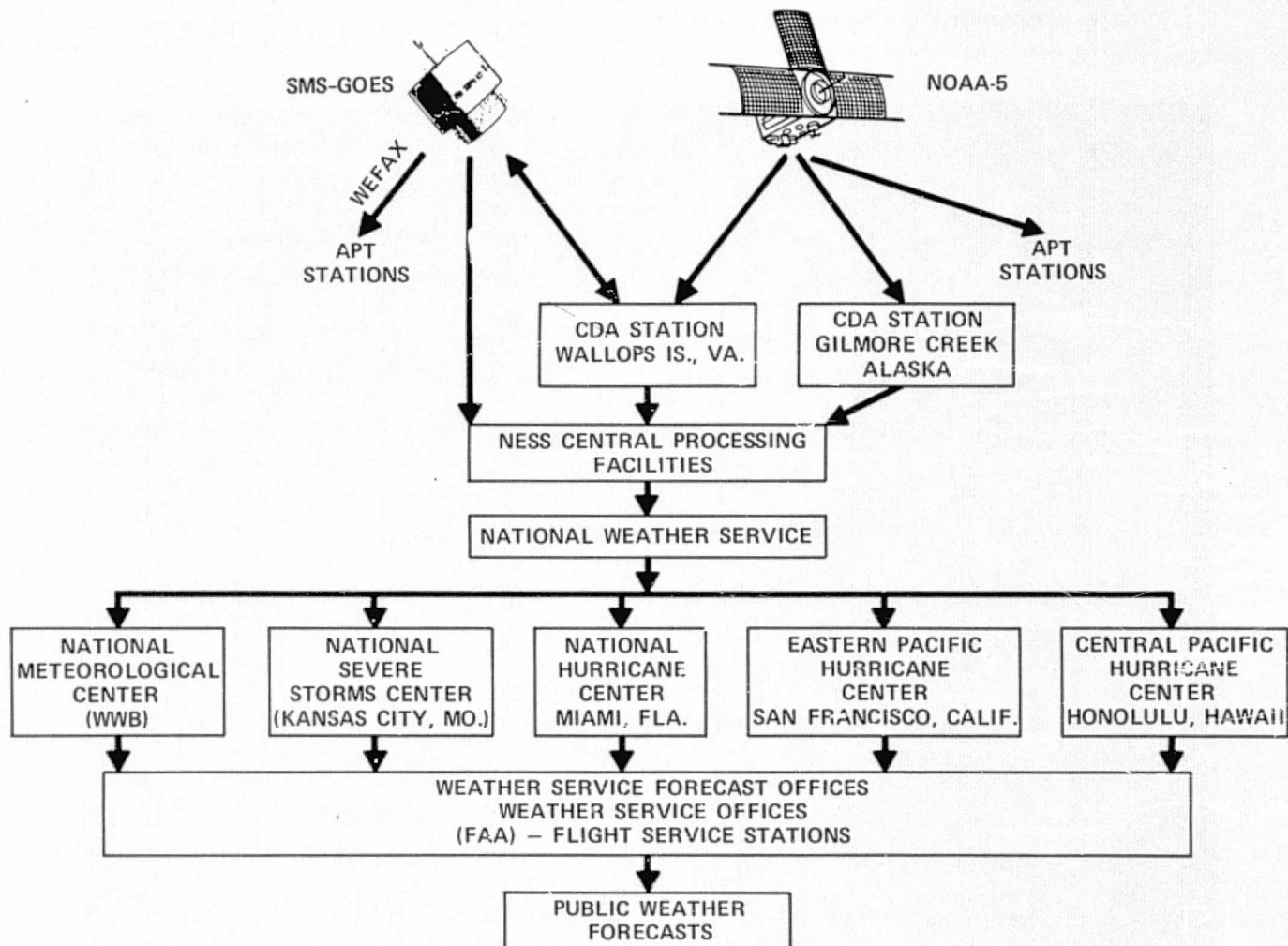


Figure 19. An Overview of the Present NOAA-NESS, Dept. of Commerce Operational Satellite Data Flow Diagram, the end product of which is weather forecasts

Figure 20. SMS-1, VISSR Infrared Surface and Cloud (T_B) Temperature Map of Florida, on 10 January 1976 (4 n mile Resolution)

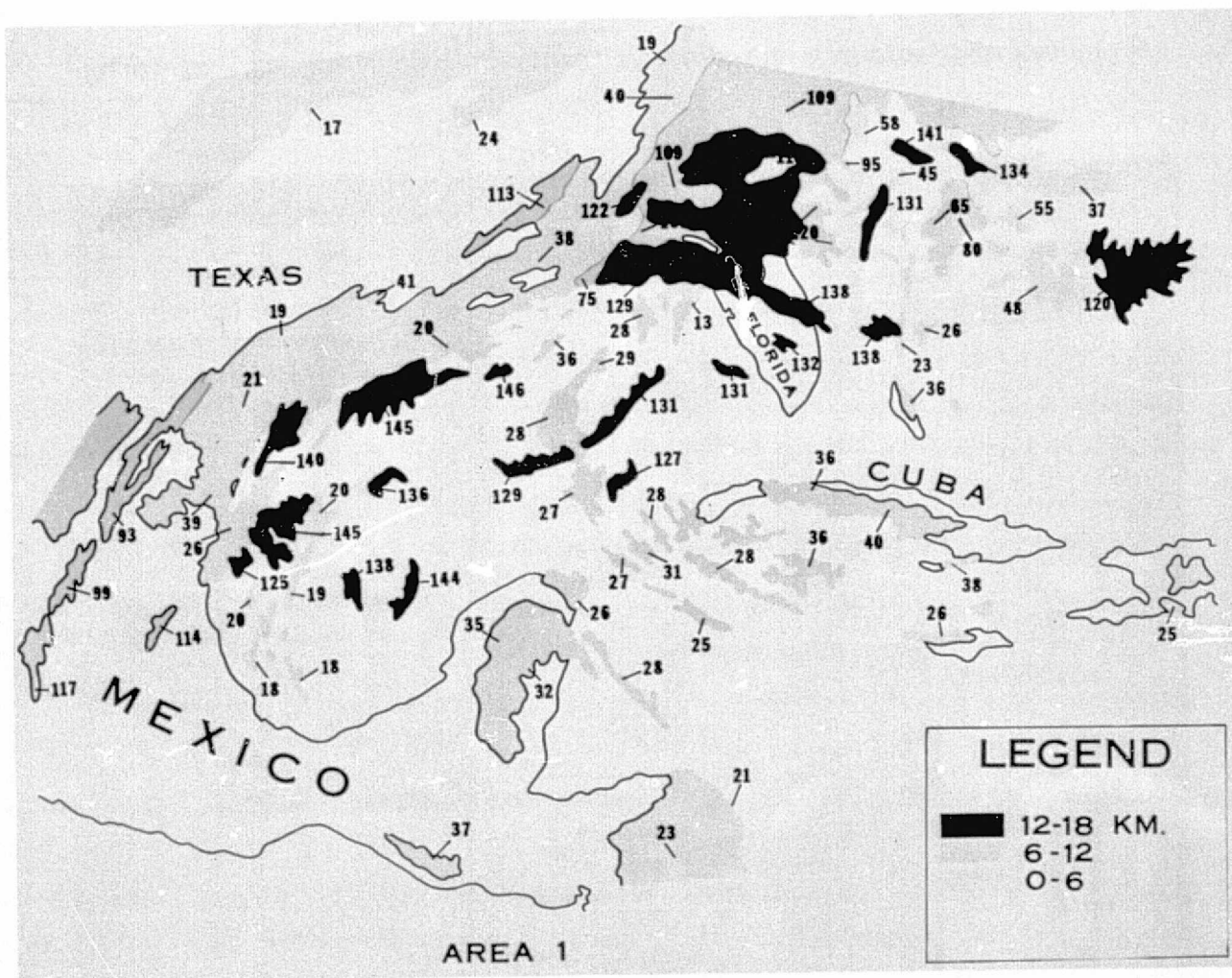


Figure 21. Cloud Heights (km) Derived Stereographically from SMS-1 and -2 on February 17, 1975 over the U.S., Gulf of Mexico and Caribbean Sea

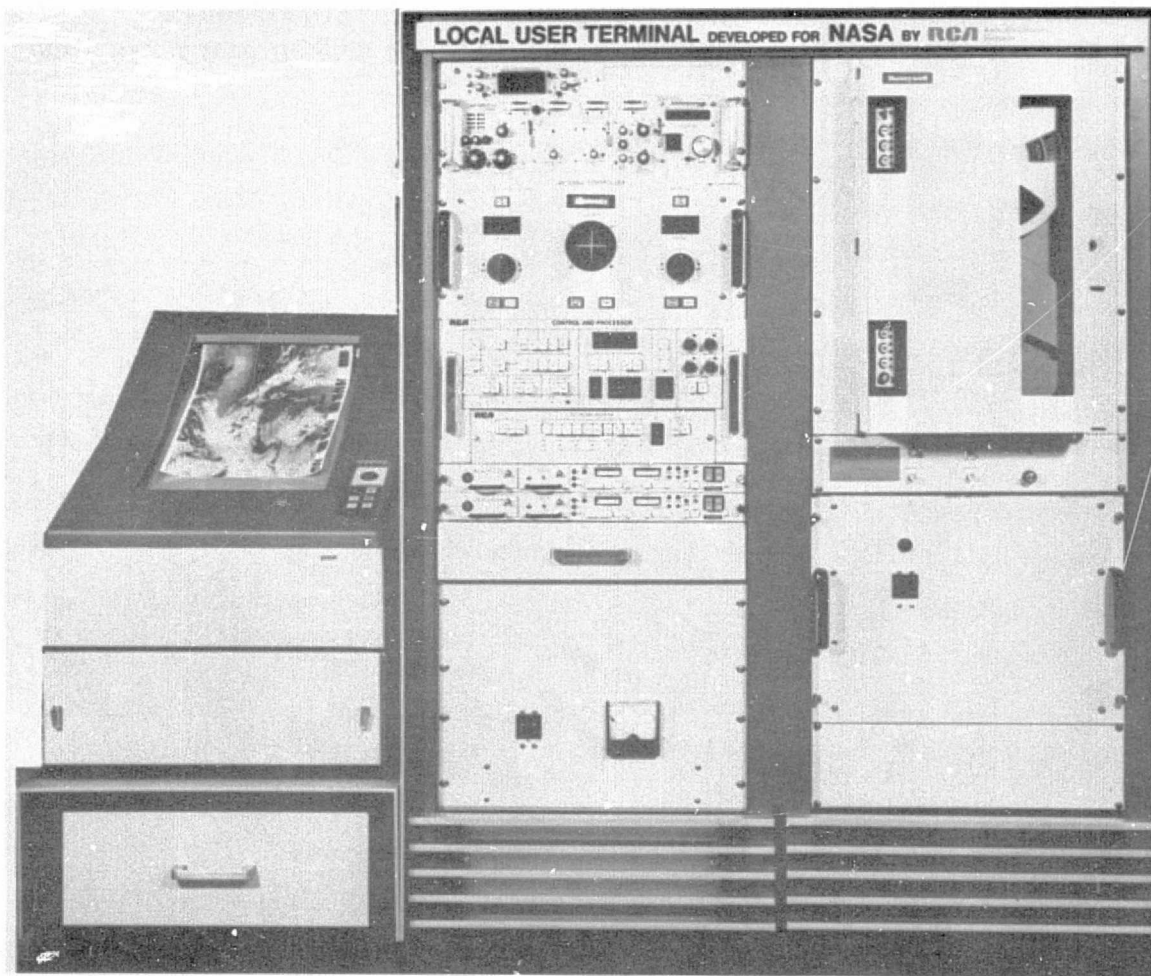


Figure 22. The Local User Terminal, Developed by NASA for High Resolution APT-Type Operation

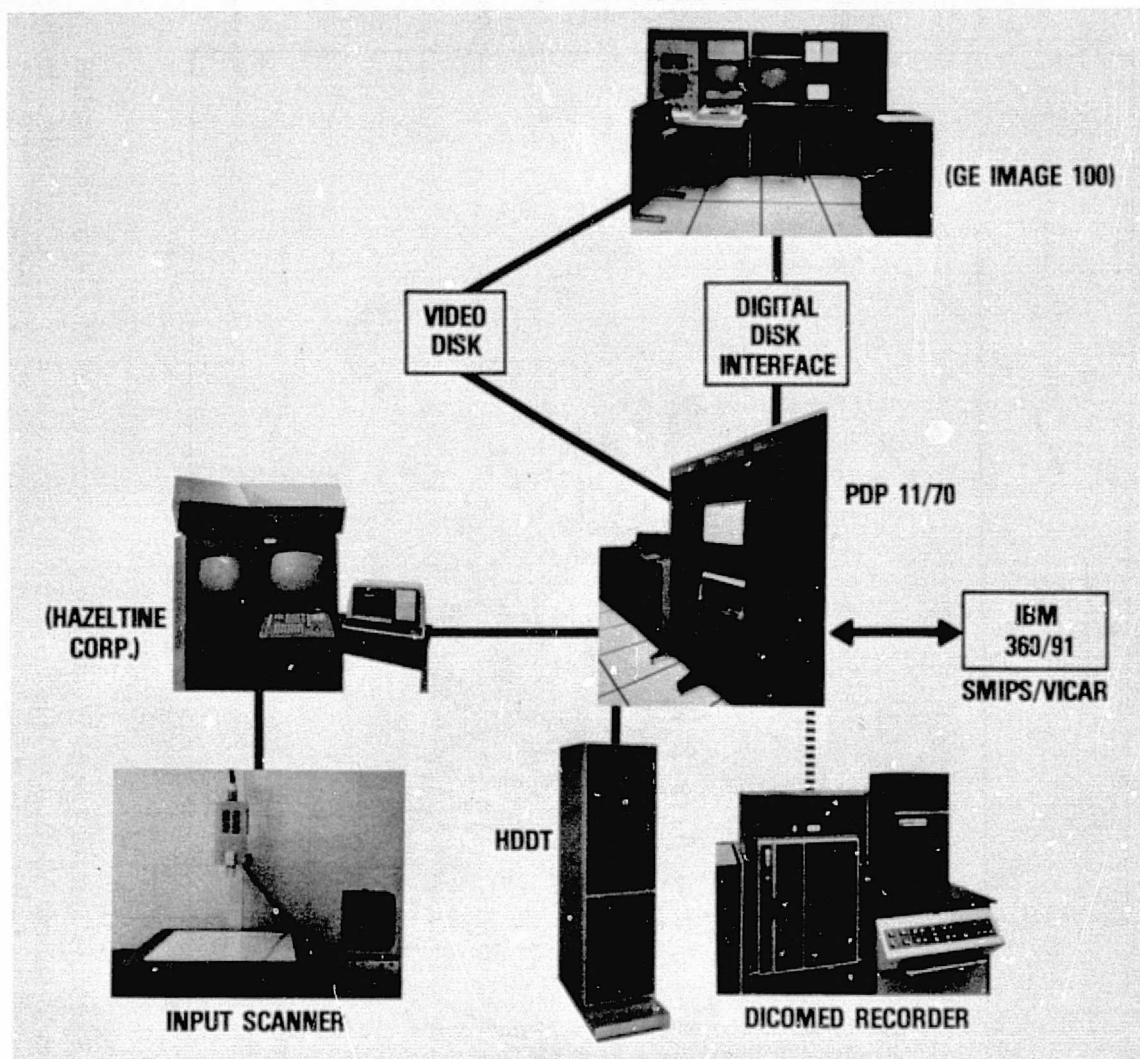


Figure 23. Components of the Atmospheric and Oceanographic Information Processing System (AOIPS) at Goddard Space Flight Center, Greenbelt, Md. 20771

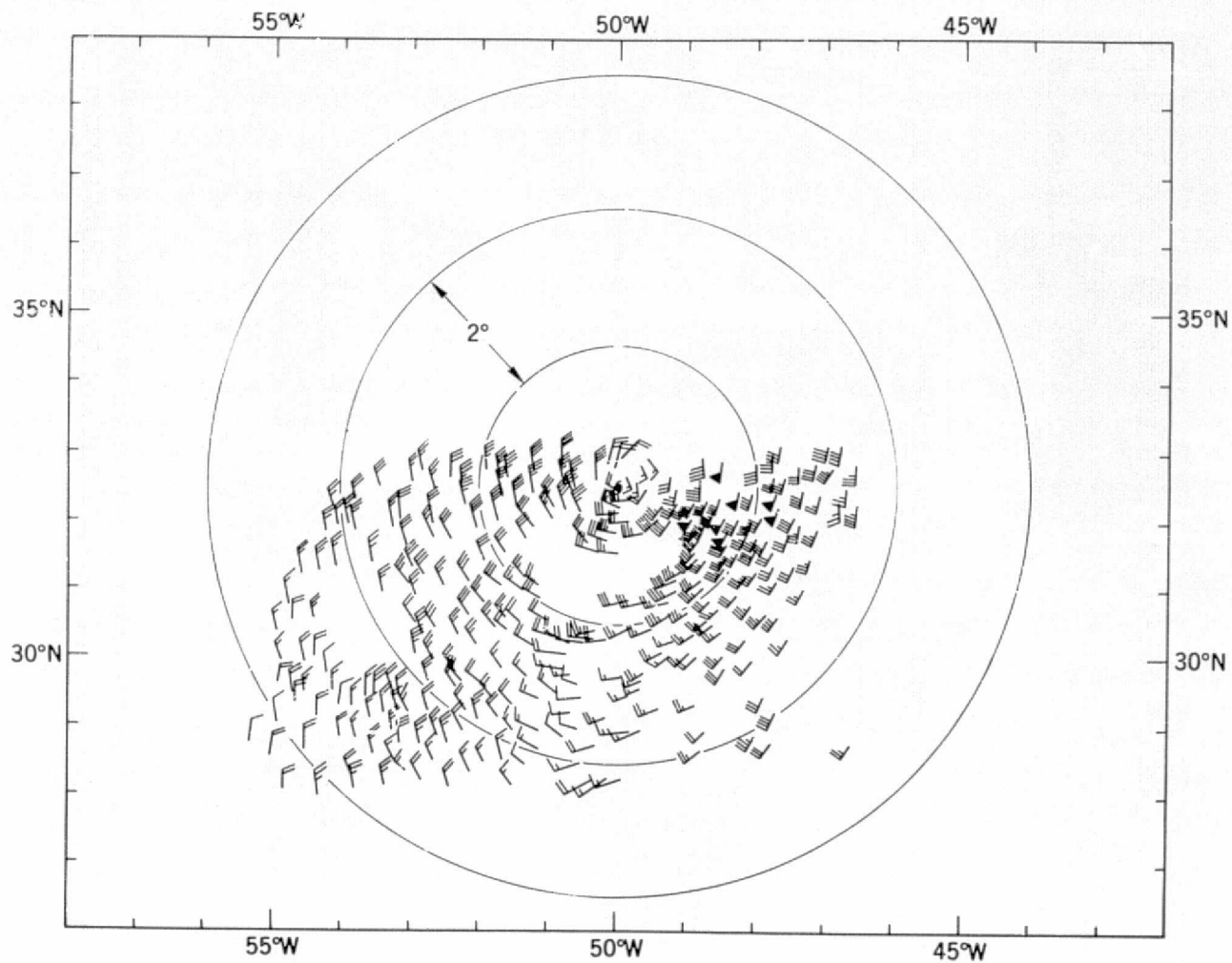


Figure 24. An Example of Low Level Winds Derived from Cloud Motion on the AOIPS from 3-Minute Visible GOES-1 Pictures Recorded over Tropical Storm Holly, 26 October 1973, 1300 GMT

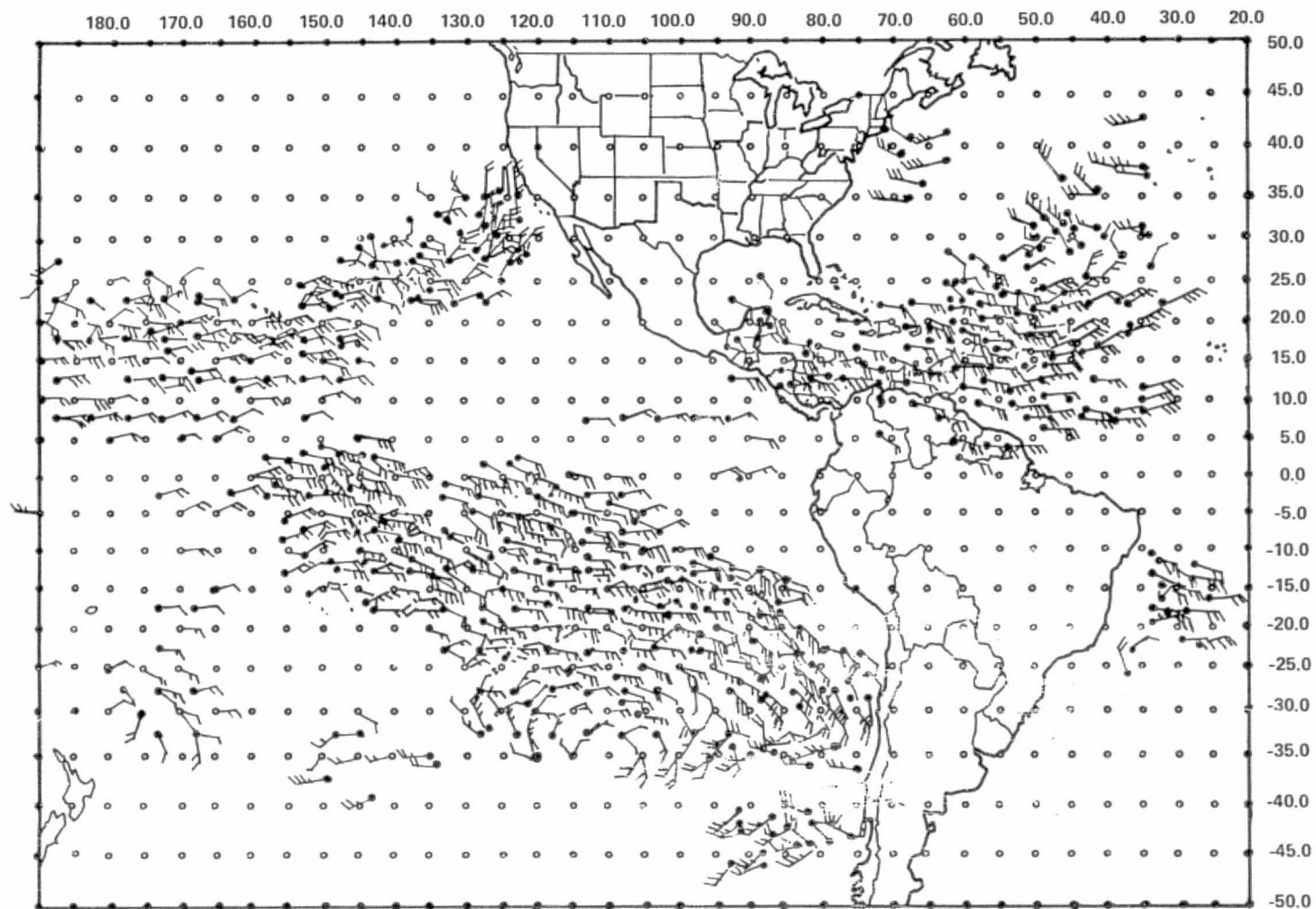
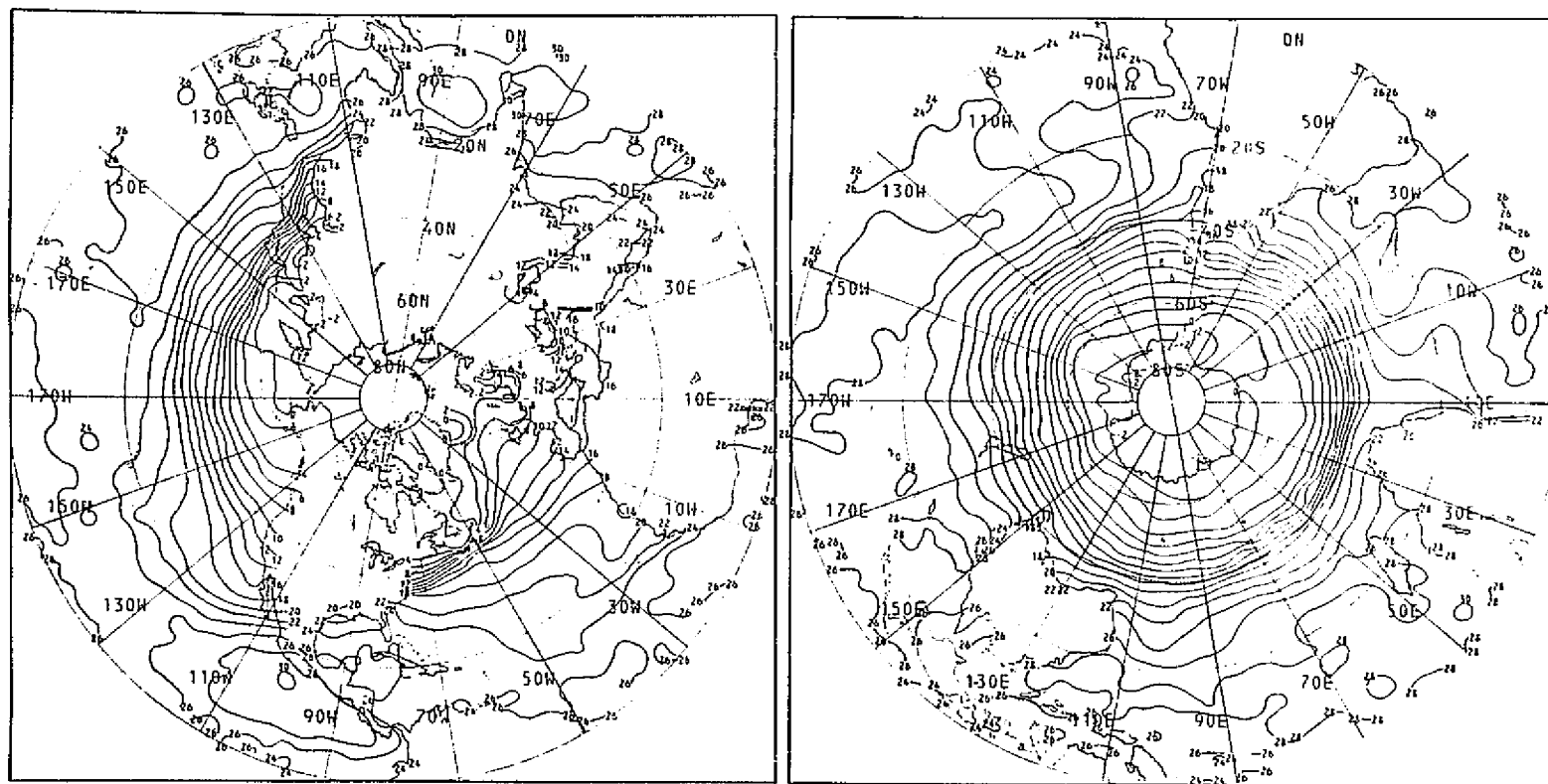


Figure 25. An Example of Low Level Winds Derived from Cloud Motion on the McIDAS, at the University of Wisconsin, Madison, Wisconsin, from Visible SMS-1, -2 Pictures, -30 Minute Data

NOAA — NESS SEA SURFACE TEMPERATURE PROJECT



NOAA-4 SATELLITE SST MONTHLY MEAN FOR MARCH 1975

Figure 26. NOAA-4 Global Infrared SR Mean Monthly Sea Surface Temperature Charts for March 1975

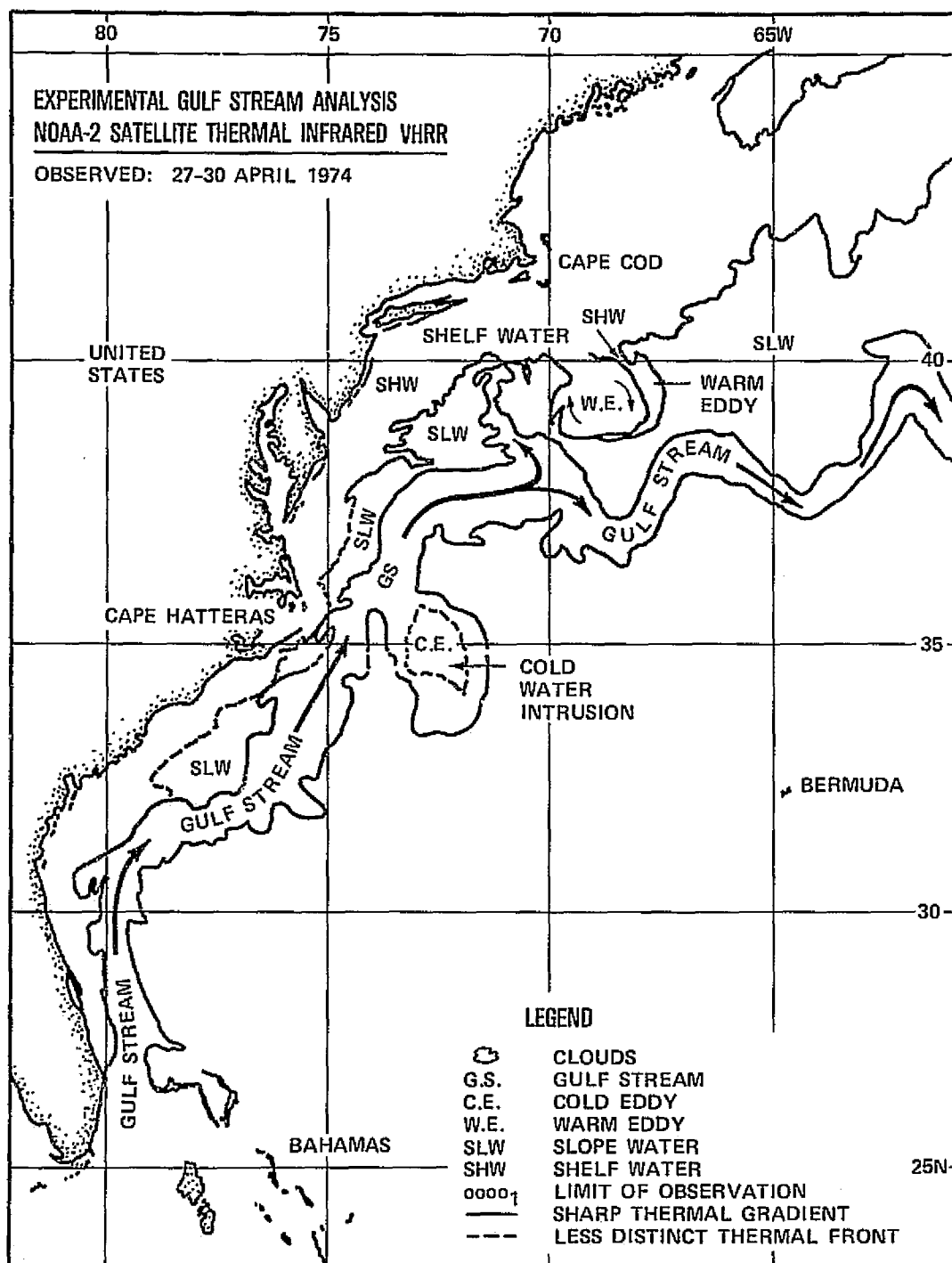


Figure 27. A Simplified Gulf Stream Infrared Sea Surface Temperature Analysis Derived from NOAA-2 VHRR Data from 27-30 April 1974

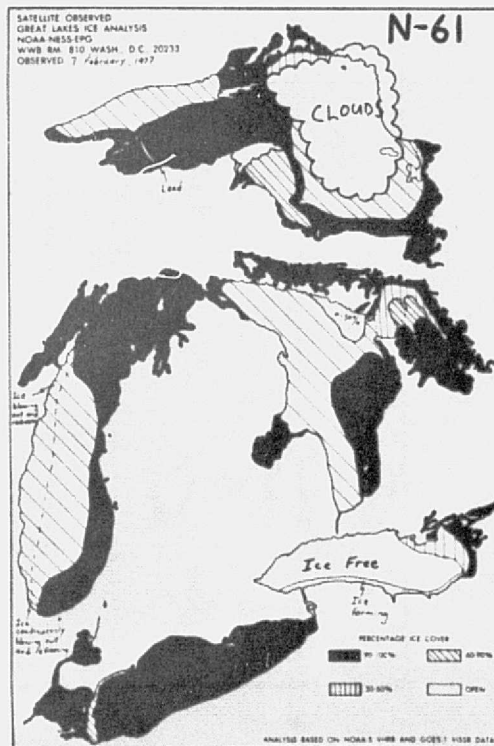
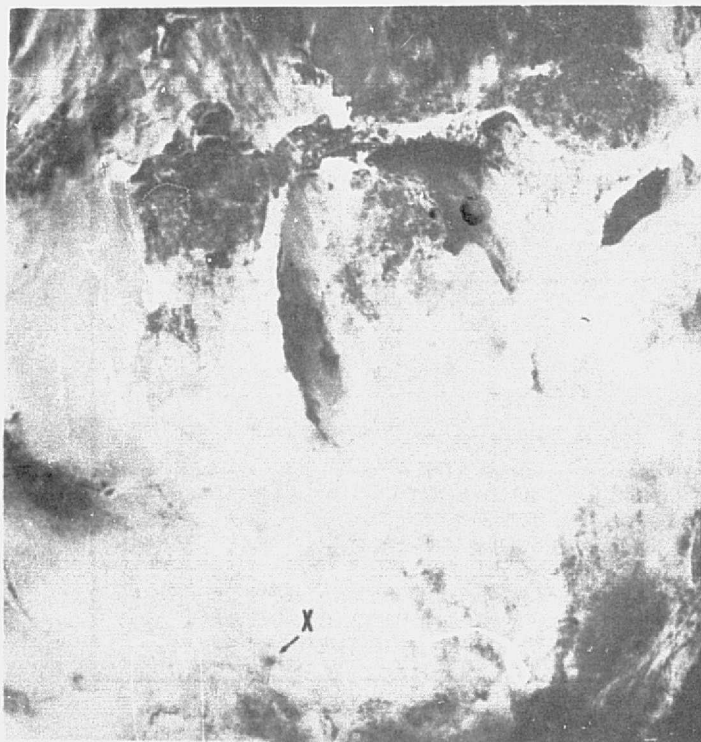
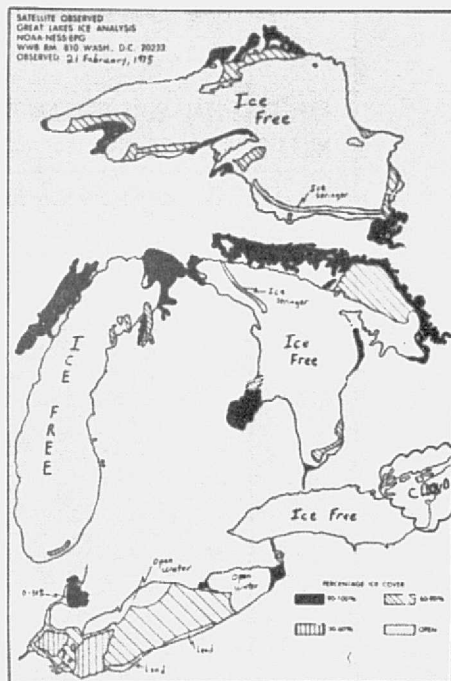
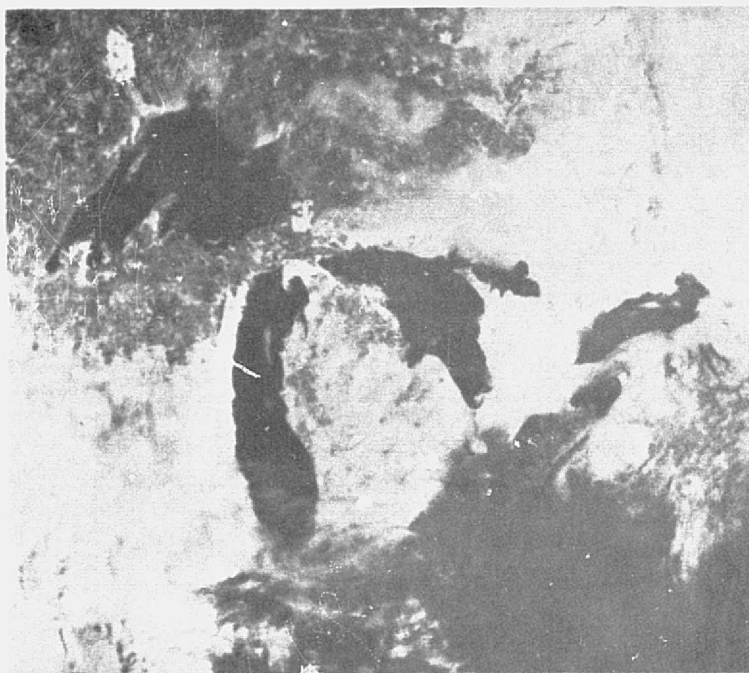


Figure 28. A NOAA-NESS Great Lakes Ice Analyses for 7 February 1977 and 21 February 1975 Derived from VHRR and VISSR Data

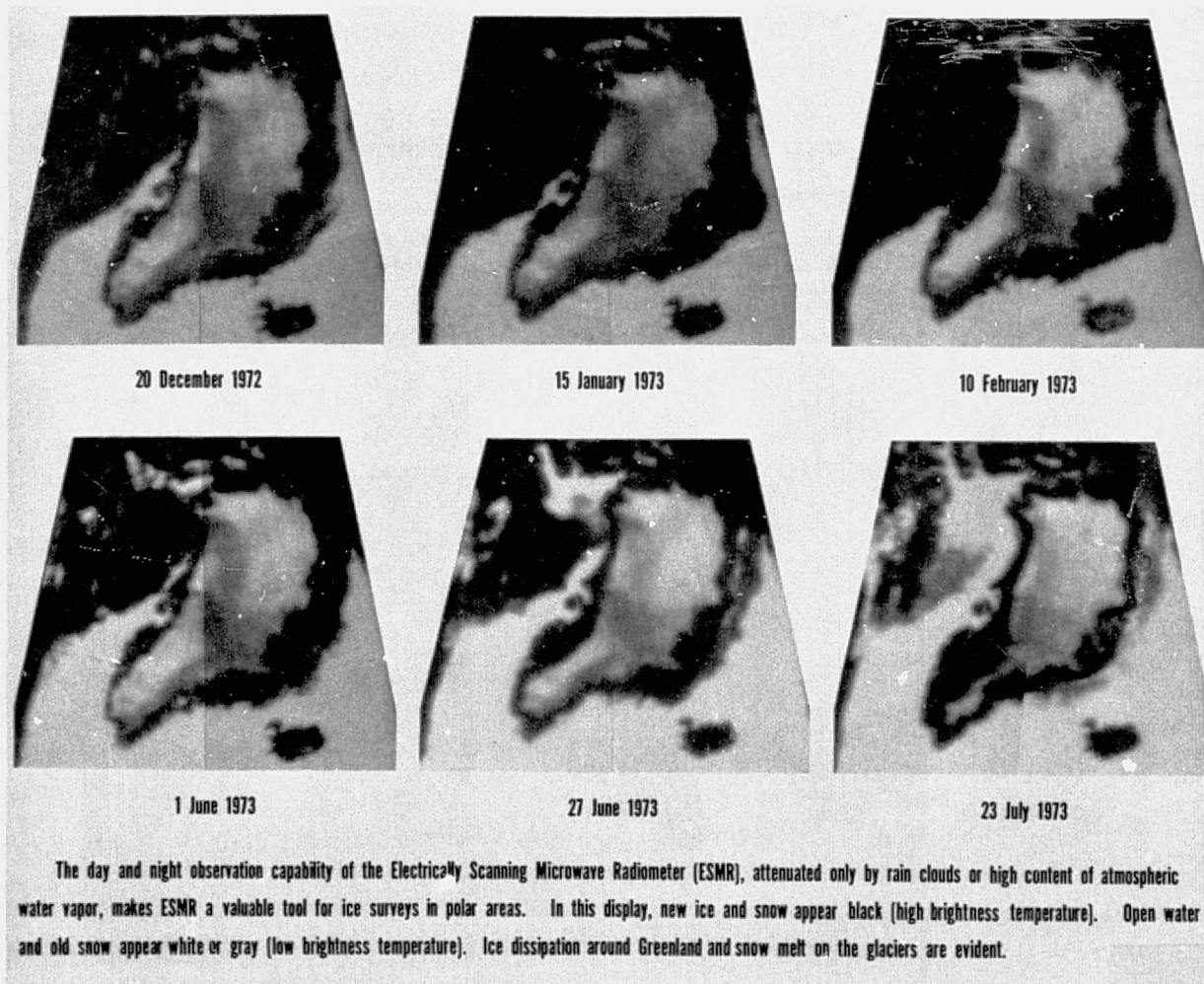


Figure 29. Seasonal Ice Boundary Changes in the Greenland Area from December 1972 to July 1973 as Recorded by Nimbus 5 ESMR (19.35 GHz), Open Water and Old Snow Appears White (Cold), while New Ice and Snow Appear Black (Warm)

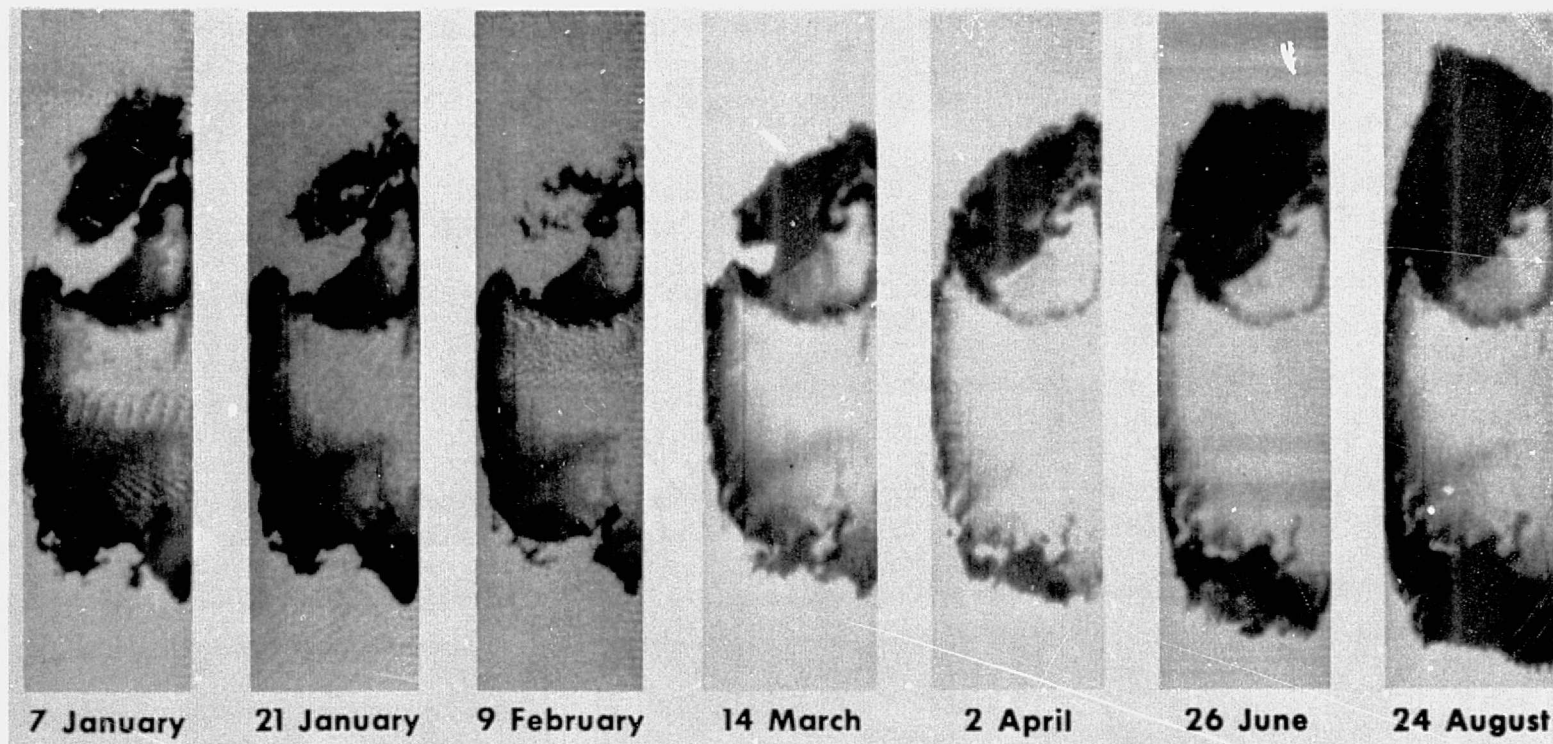


Figure 30. Seasonal Ice Boundary Changes in the Antarctic Area from January to August 1973 as Recorded by Nimbus 5 ESMR (19.35 GHz)

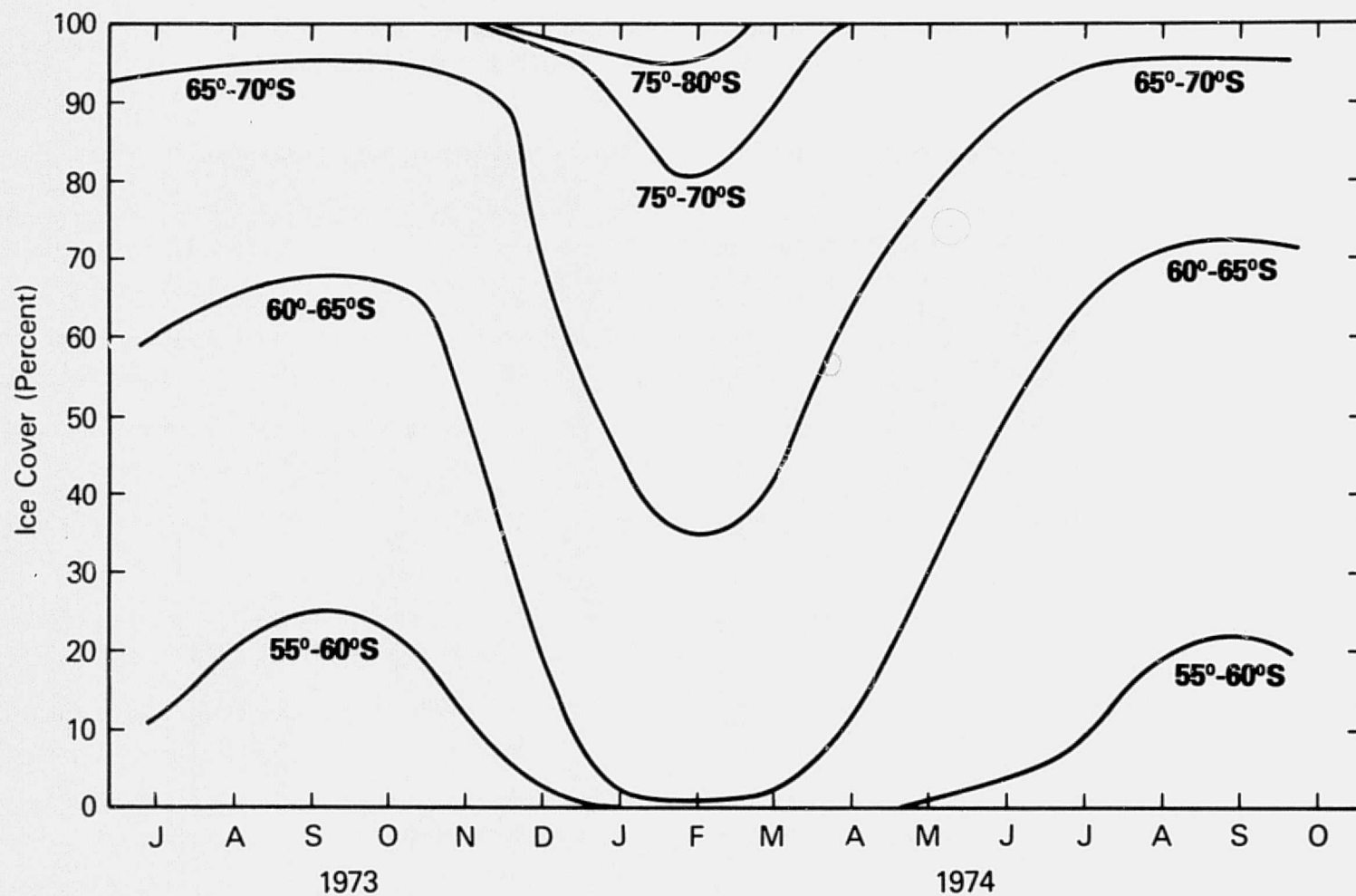


Figure 31. Monthly Ice Cover Changes, in Percent over the Antarctic from July 1973 to October 1974, as Derived from Nimbus 5 ESMR (19.35 GHz) Imagery

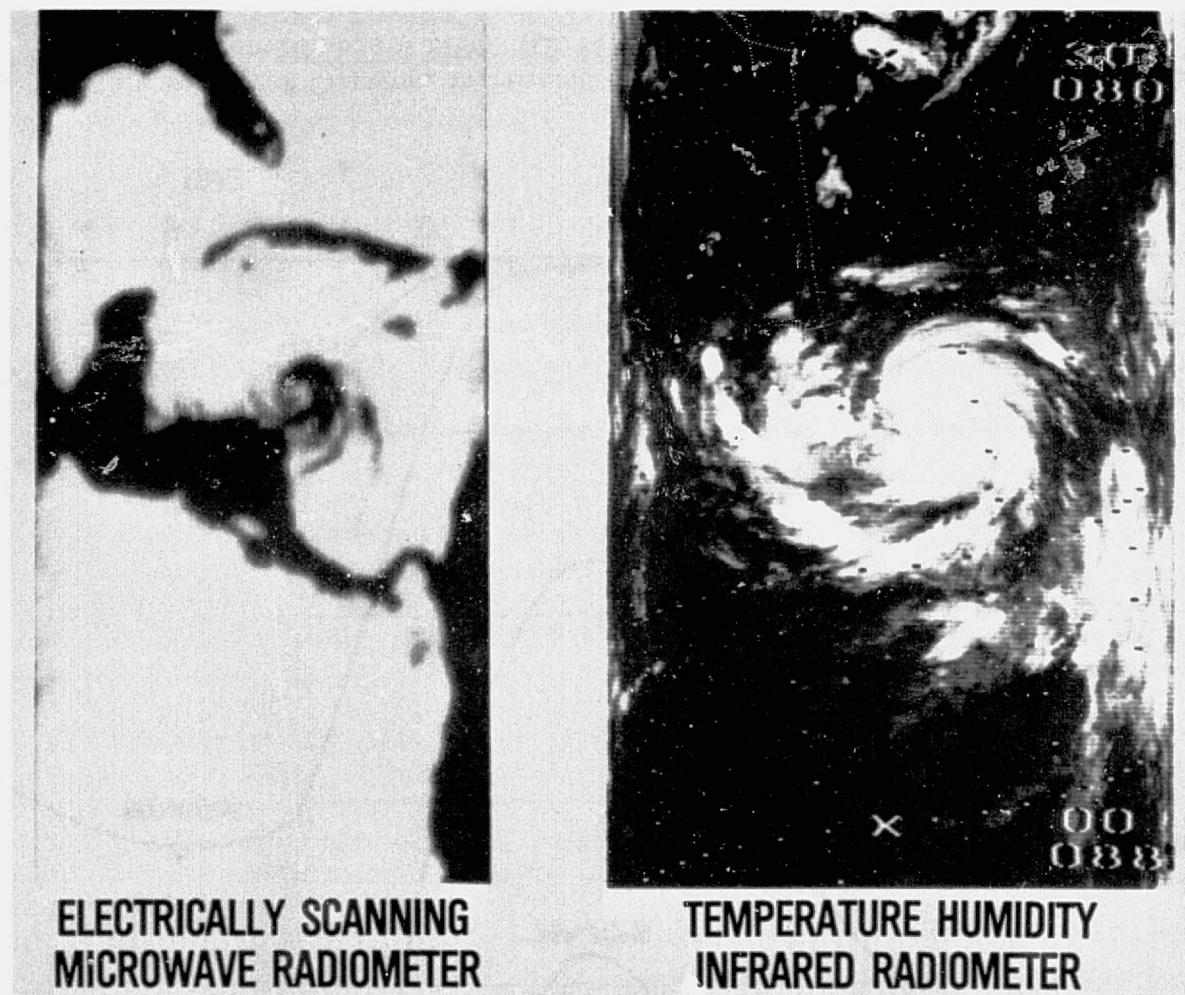


Figure 32. Nimbus 5 ESMR (19.35 GHz) and THIR (11 μ m) Facsimile Pictures over Hurricane Fifi, on 18 September 1974

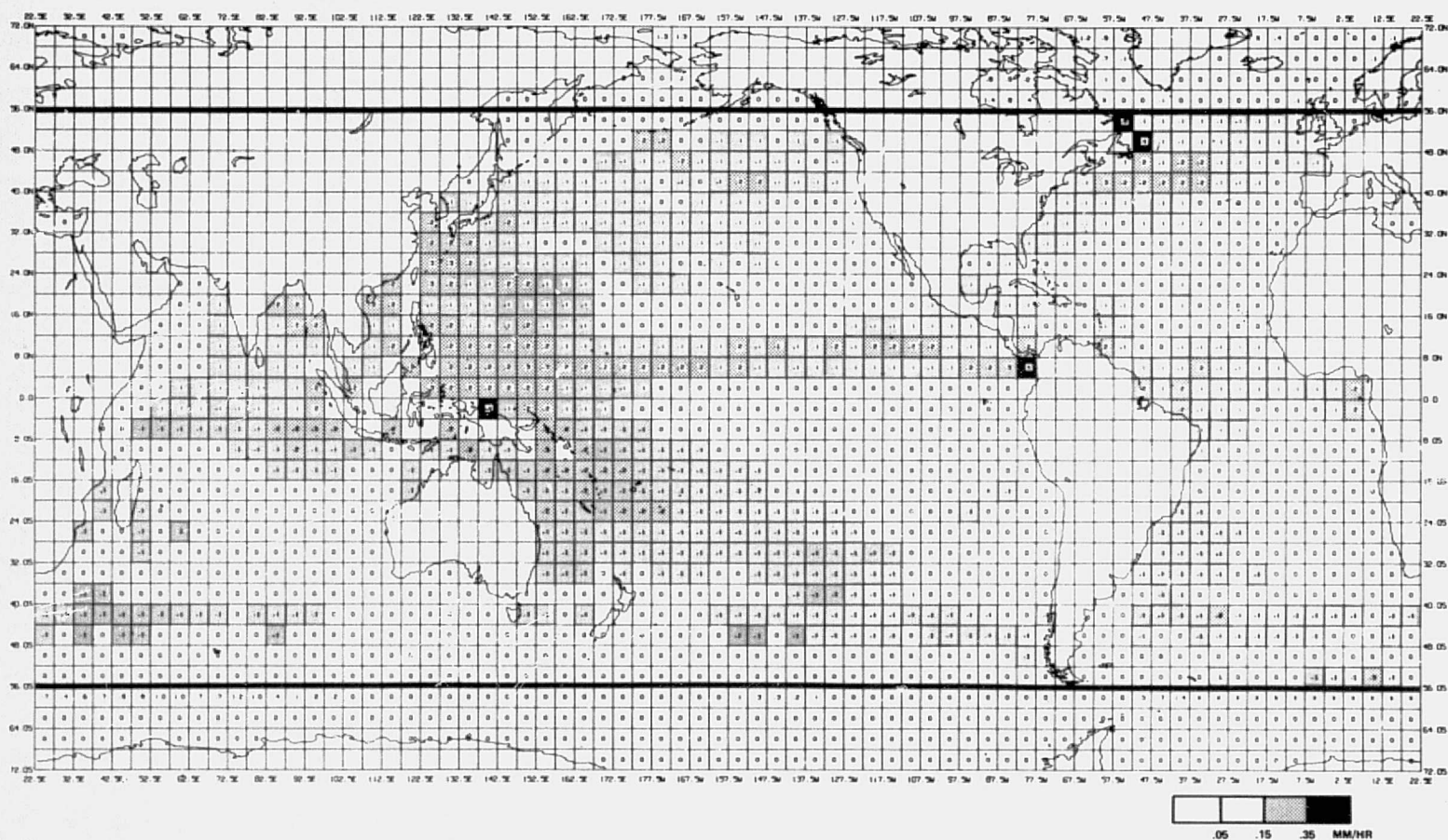


Figure 33. Global Annual Oceanic Rainfall Rate (Averaged in mm/hr) from Nimbus 5 ESMR (19.35 GHz) Data from January 1974 to December 1974

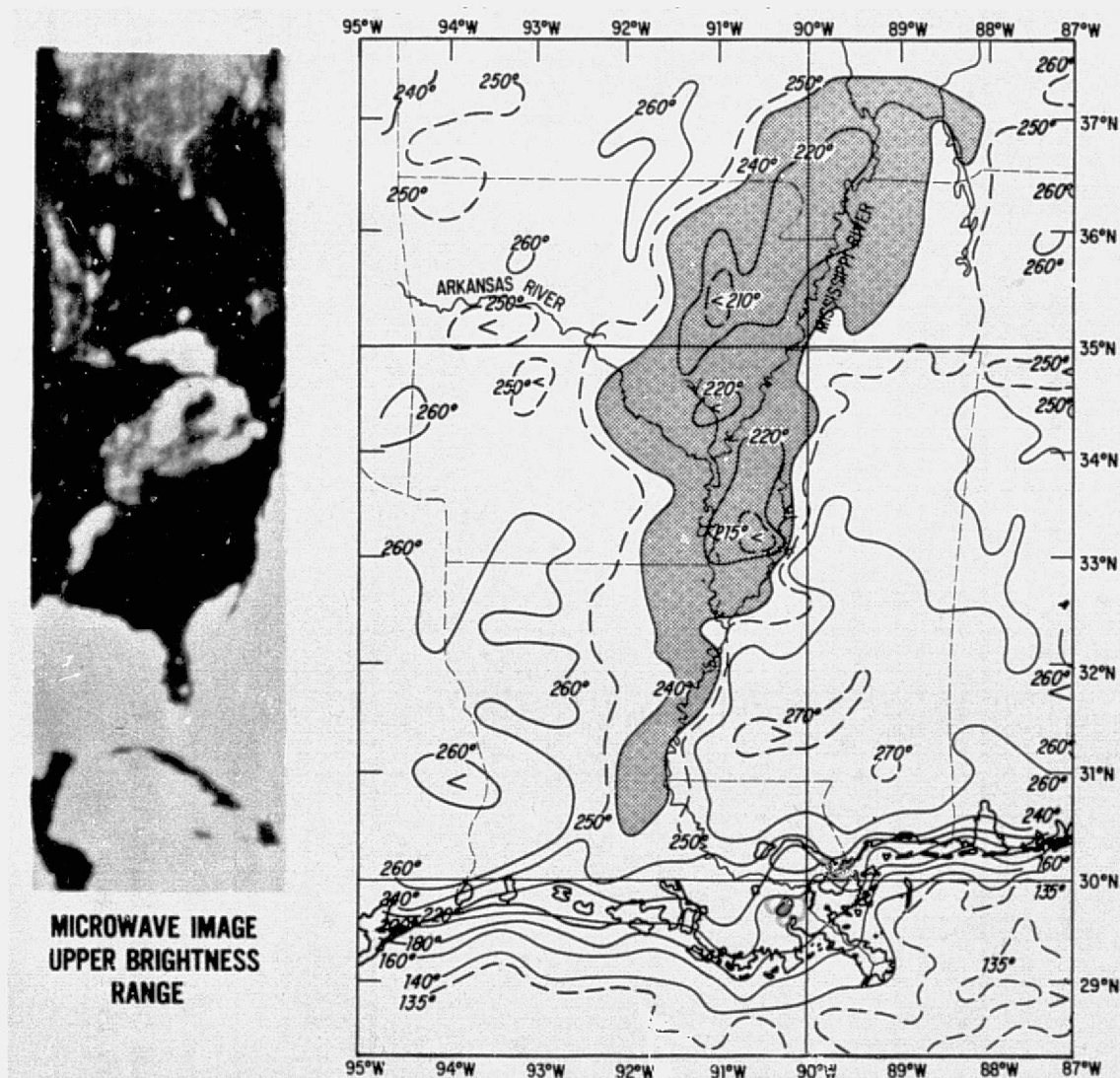


Figure 34. Nimbus 5 ESMR (1.55 cm) Facsimile Picture over the Eastern U. S. on 22 January 1973 and a Grid Print Map Analysis (T_B) in $^{\circ}\text{K}$ over the Mississippi Valley and Gulf Coast, Indicating High Soil Moisture (Cold T_B , $< 240^{\circ}\text{K}$), in Grey Tone

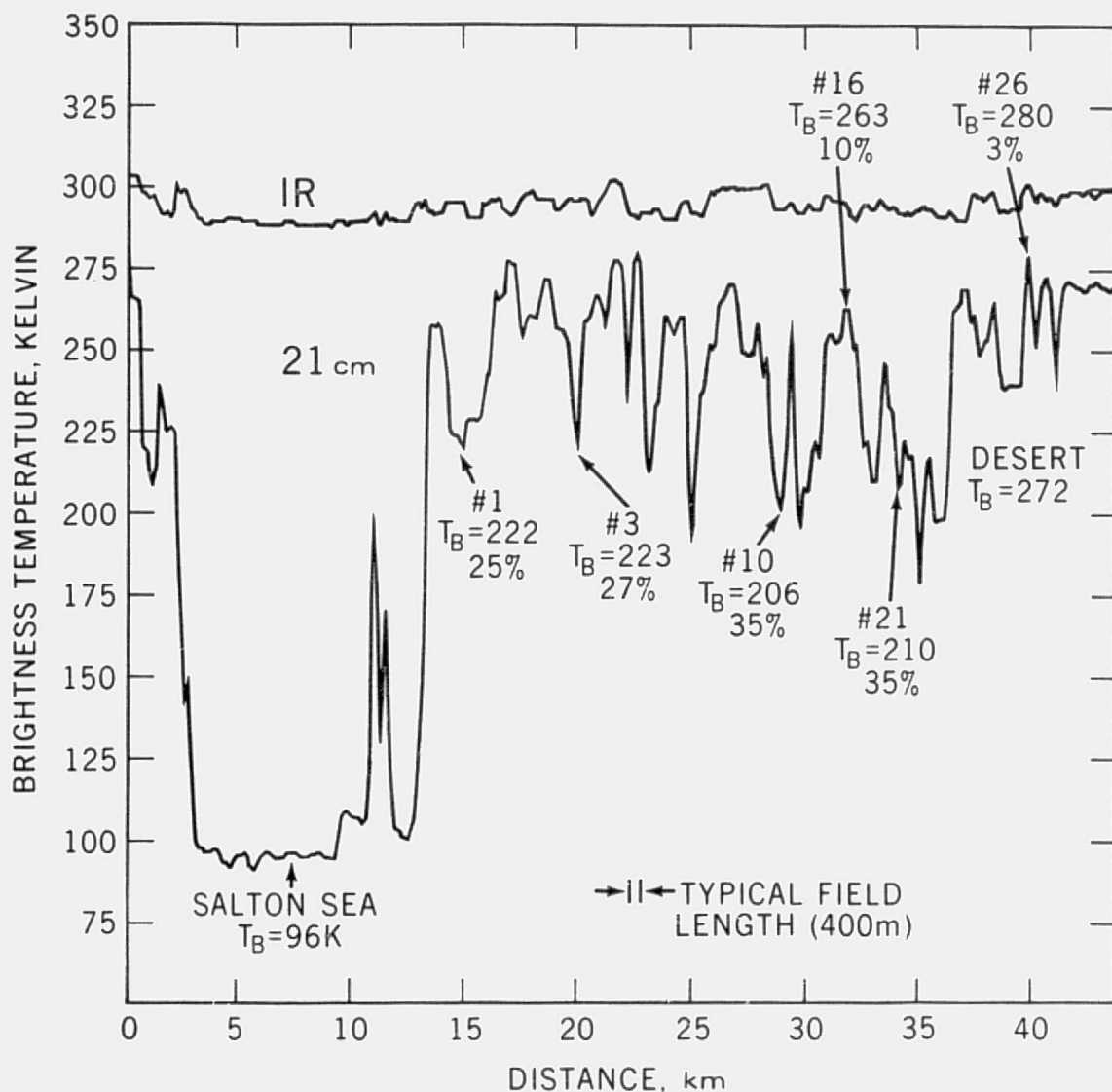


Figure 35. Aircraft Thermal Infrared (10 to 12 μm) and Microwave (21 cm) Brightness Temperature Versus Flight Distance at the North End of the Imperial Valley, Calif. The 21-cm Brightness Temperature and Measured Soil Moisture for Several Vegetated Fields the Salton Sea and Desert Land are Indicated (Schmugge et al., 1976)

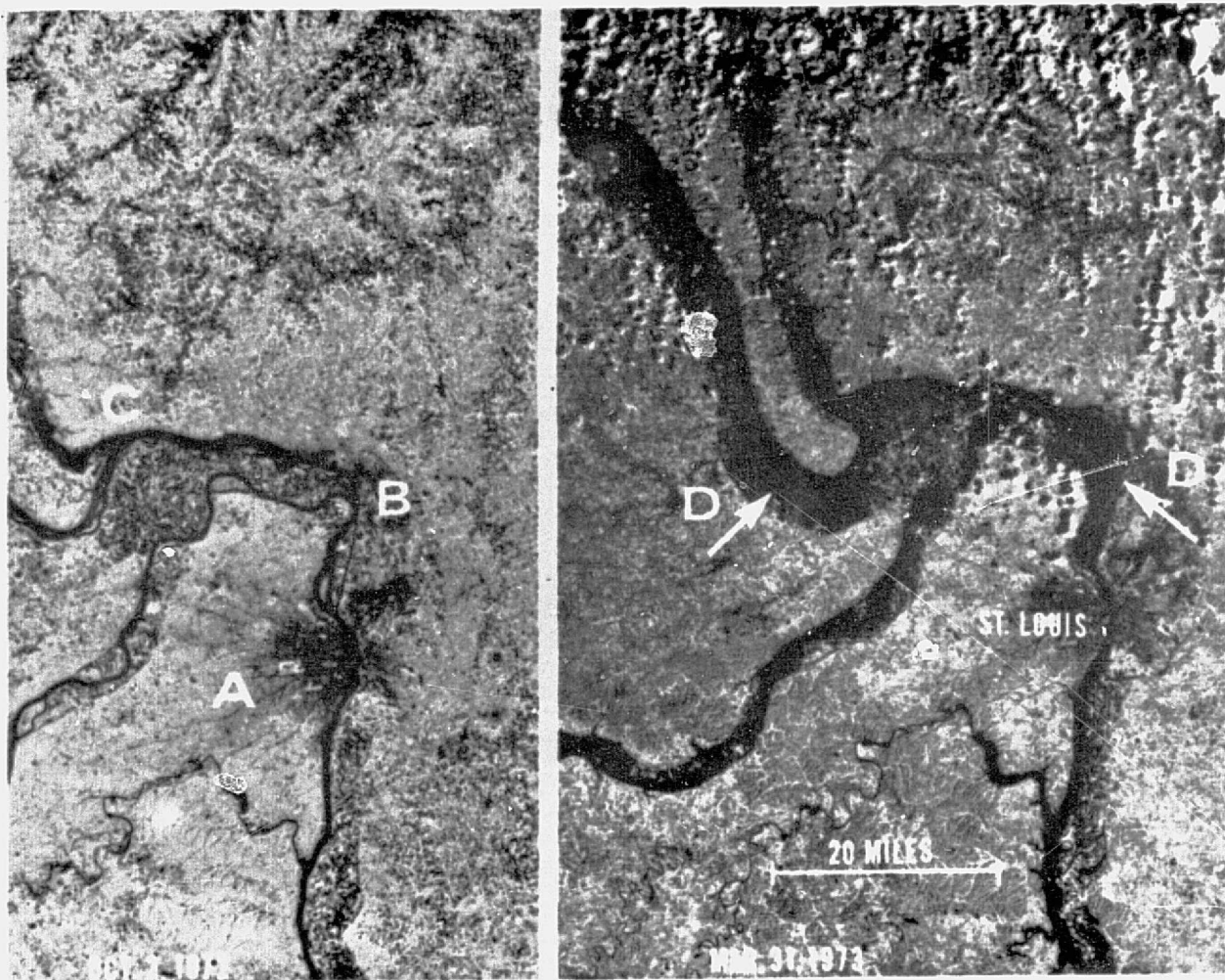
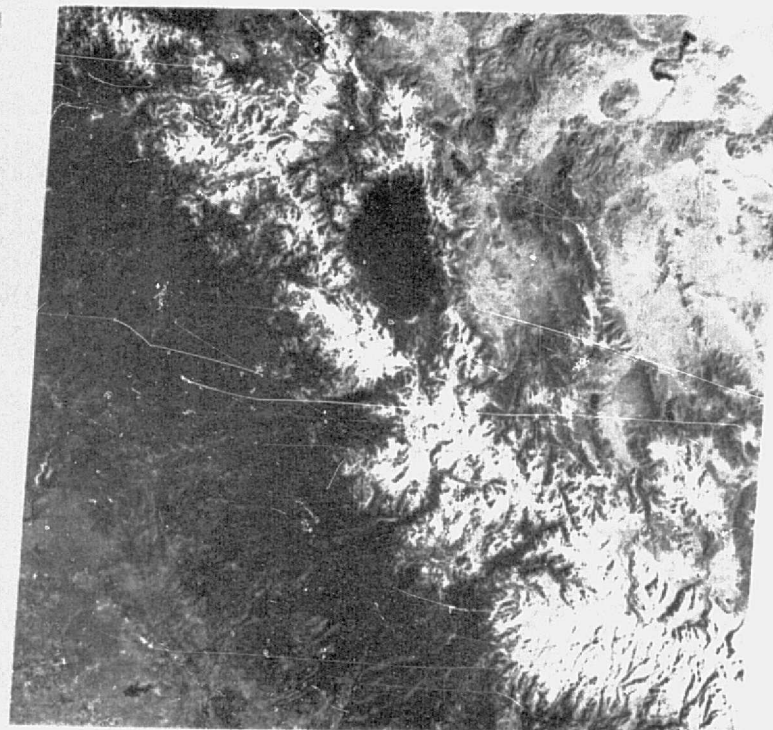
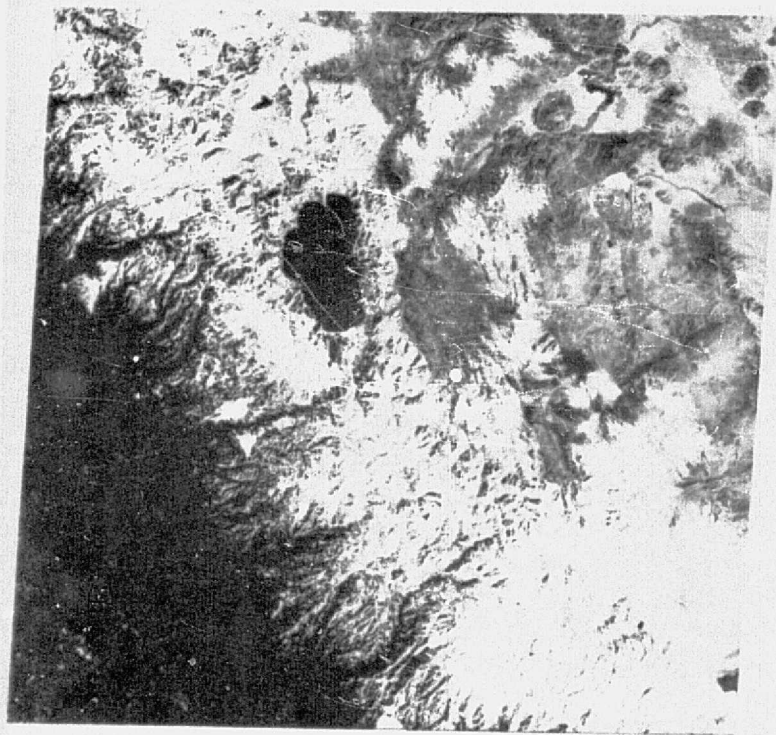


Figure 36. Pre-Flood (Oct. 2, 1972) and Flood (March 31, 1973) Stage for the Mississippi River Shown by Landsat MSS, Band 7 (0.8 to 1.1 μm). A Indicates St. Louis, Mo., C and B Indicate the Confluence of the Missouri and the Mississippi River and the Illinois and Mississippi River Respectively; D Indicates Areas of Significant Flooding



Figure 37. Western Negev (Vegetated-Dark) and Sinai Desert Non-Vegetated (Light) on the Israel-Egypt Border as Shown by LANDSAT 1, MSS, Band 7 Picture, 24 August 1973 (80 m Resolution)



25 FEBRUARY 1975 AVERAGE SNOWLINE ELEVATION=4500 FT. 14 FEBRUARY 1977 AVERAGE SNOWLINE ELEVATIONS=6500 FT.

Figure 38. Snow Cover Difference in the Sierra Nevada Mts., Near Lake Tahoe, Calif. (Left) 25 February 1975 (Normal Year) and (Right) 14 February 1977 (Drought Year) LANDSAT 2 MSS, Band 5, (0.6 to 0.7 μ m) Pictures



Figure 39. An Example of Weather Modification Due to Man's Industrial Activities Shown in a LANDSAT 1, (MSS 5) Picture Recorded on 24 November 1972 over Lake Michigan. SW to NE Wind Arrows and Barbs Point to Smoke Stack Plume Trajectory over the Lake Which Leads To Cloud Sheet and Snow Fall Development Further Downwind. Air Temperature Visibility and Dew Point Numbers are Plotted to Left of Weather Station Circle

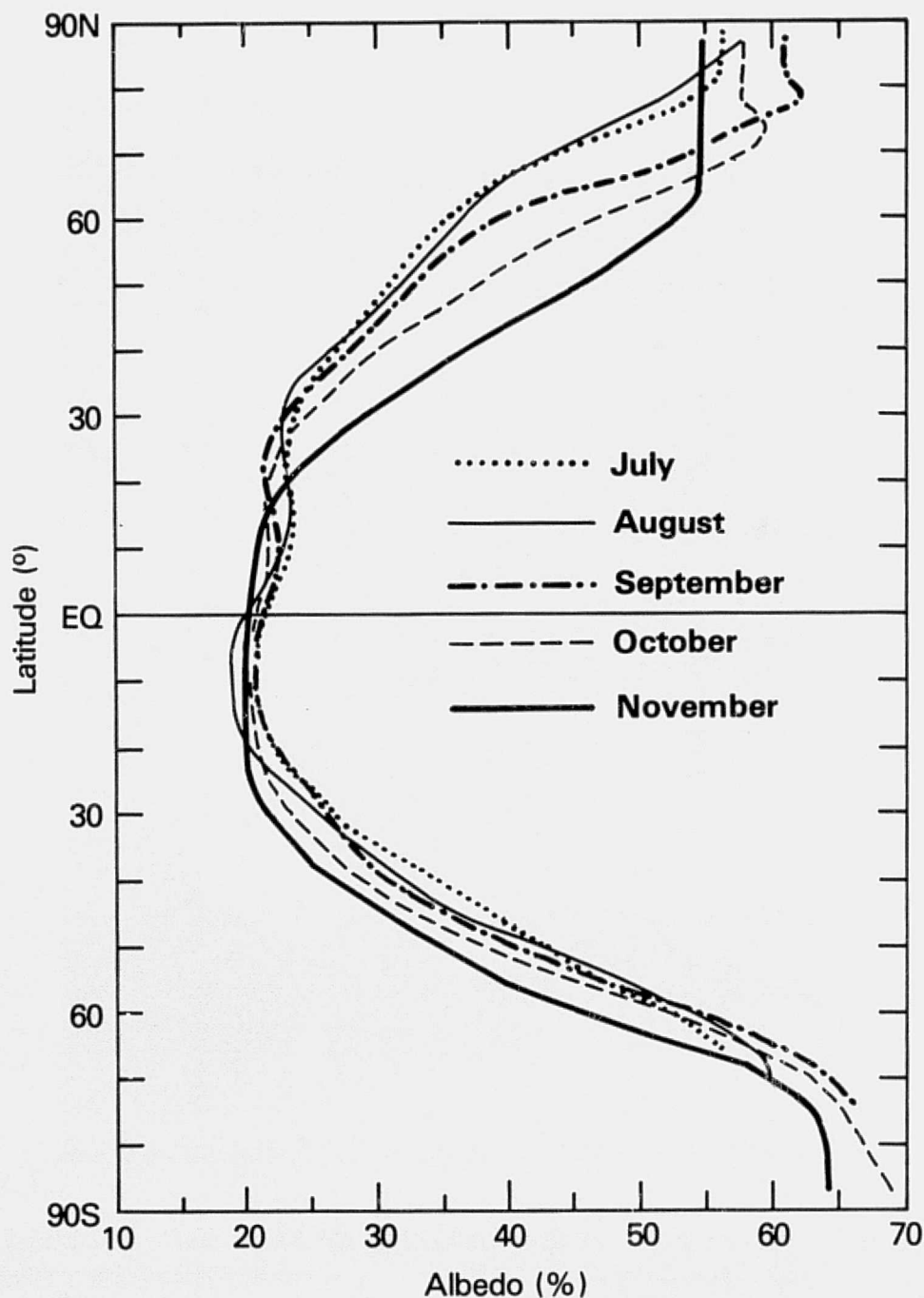
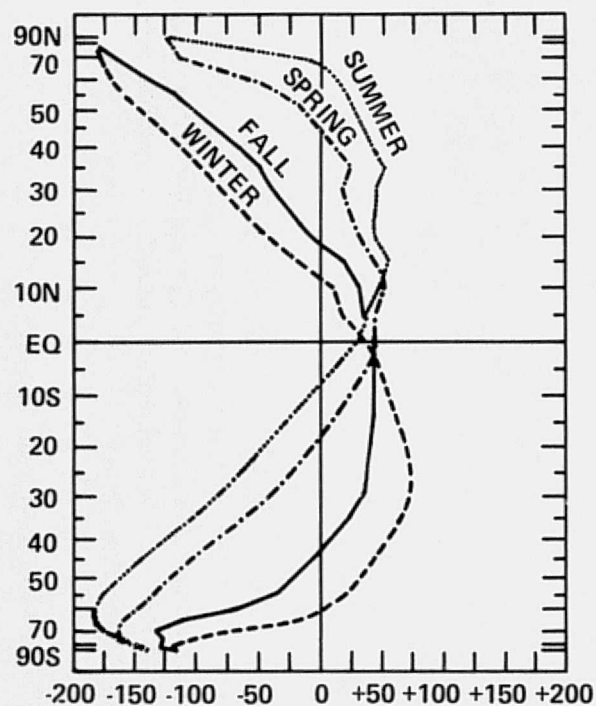
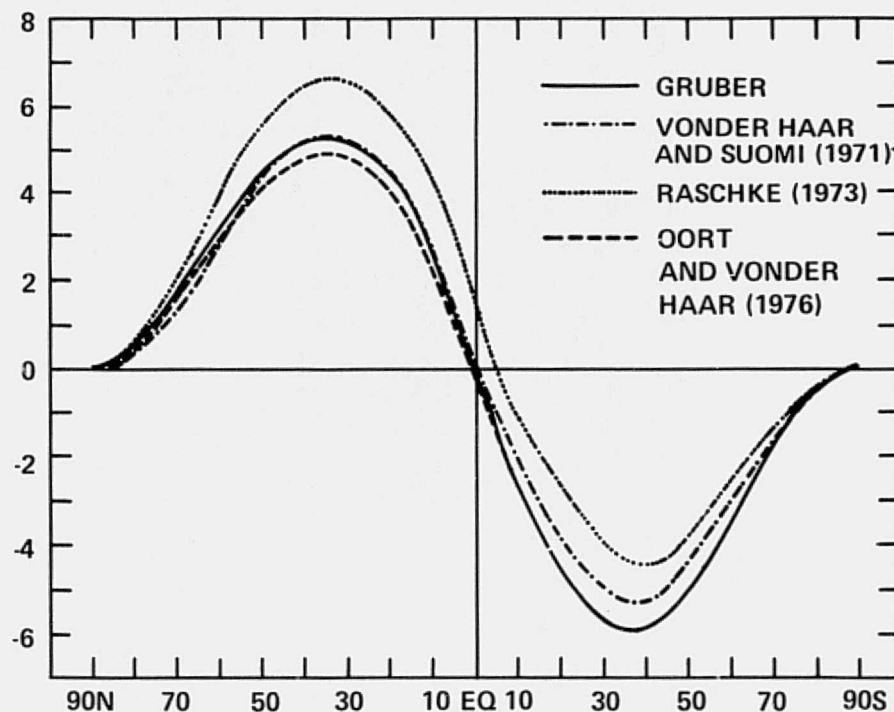


Figure 40. Variation in Global Albedo as Measured by Nimbus 6 ERB from July Through November 1975, Using Solar and Wide Angle Channels



NET RADIATION BALANCE PROFILES



MEAN ANNUAL MERIDIONAL TRANSPORT OF ENERGY

Figure 41. Computed Global Net Radiation Balance Using 2-Channel NOAA-4 SR Data

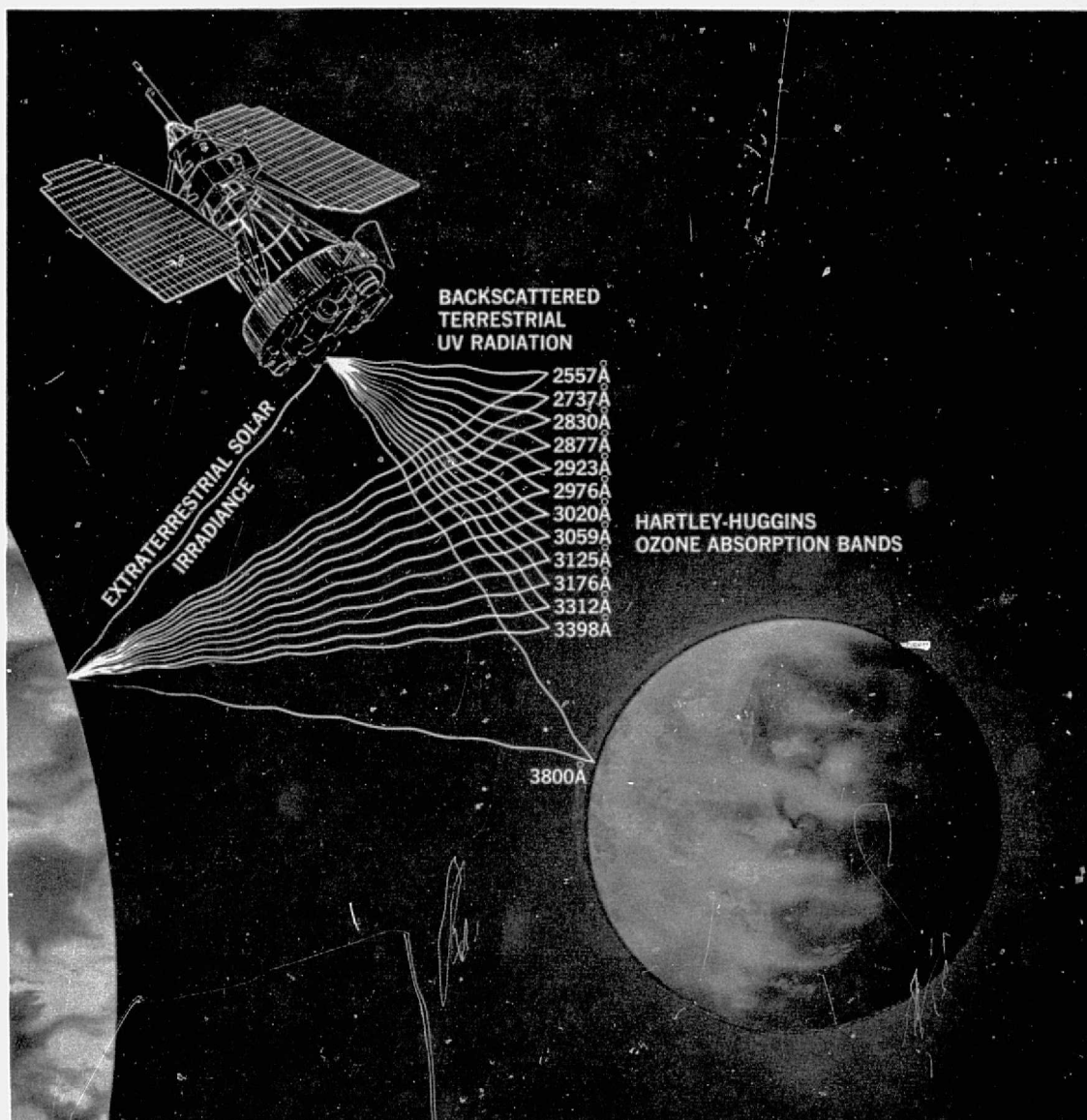
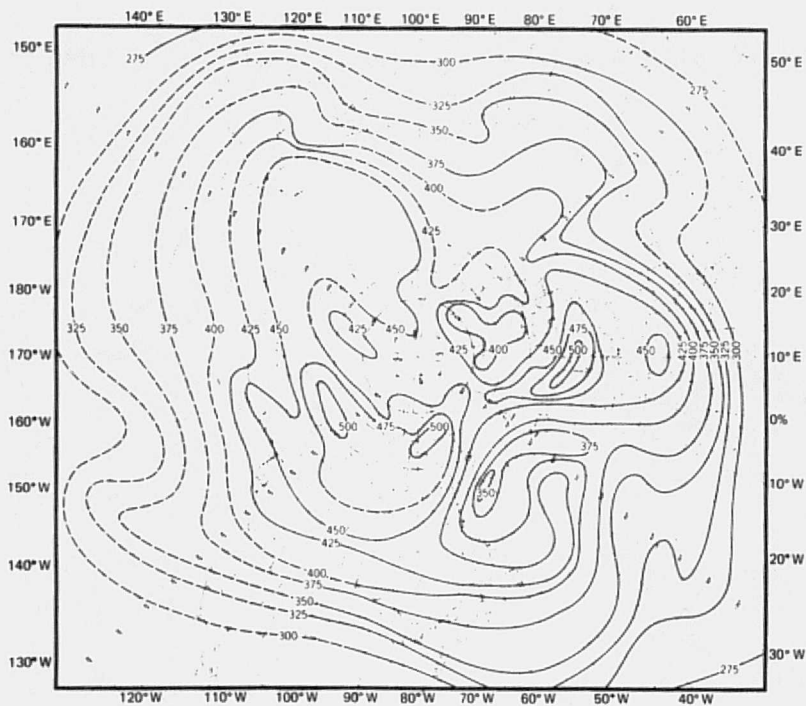


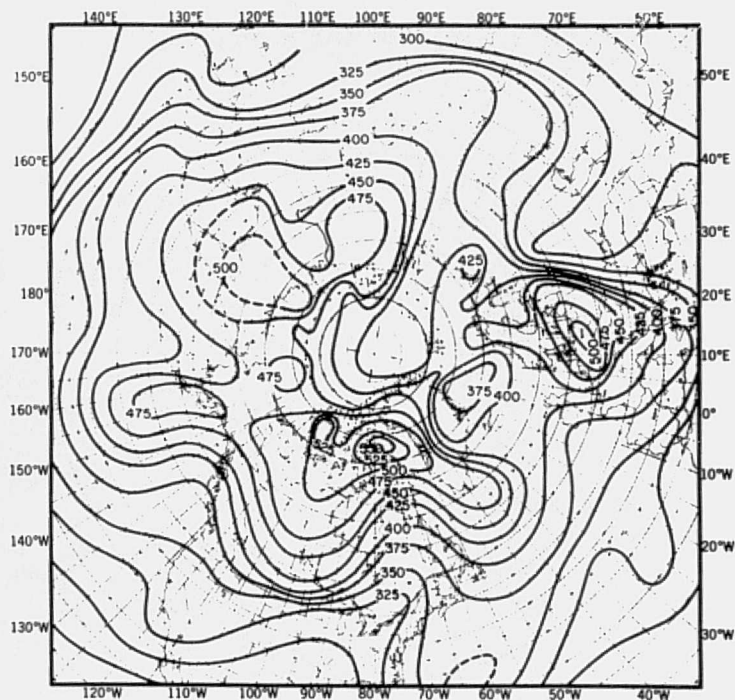
Figure 42. Schematic of Nimbus 4 Backscatter Ultraviolet (BUV) Instrument which Determines Total Ozone Content and Vertical Ozone Distribution by Measuring the Backscattered Ultraviolet Solar Energy at the Satellite Nadir at 12 Wavelengths from 2557 to 3398 Angstroms in the Ozone Absorption Band

(Permission to reprint, courtesy of Beckman Instruments, Inc.)

APRIL 28-29, 1970



APRIL 30 - MAY 1, 1970



NASA HQ ERD77-1375(2)
1-14-77

Figure 43. Global Total Ozone Content Maps (Units; Milli atm-cm) Derived from Nimbus-4 BUW Data on April 28-29, 1970 and April 30-May 1, 1970

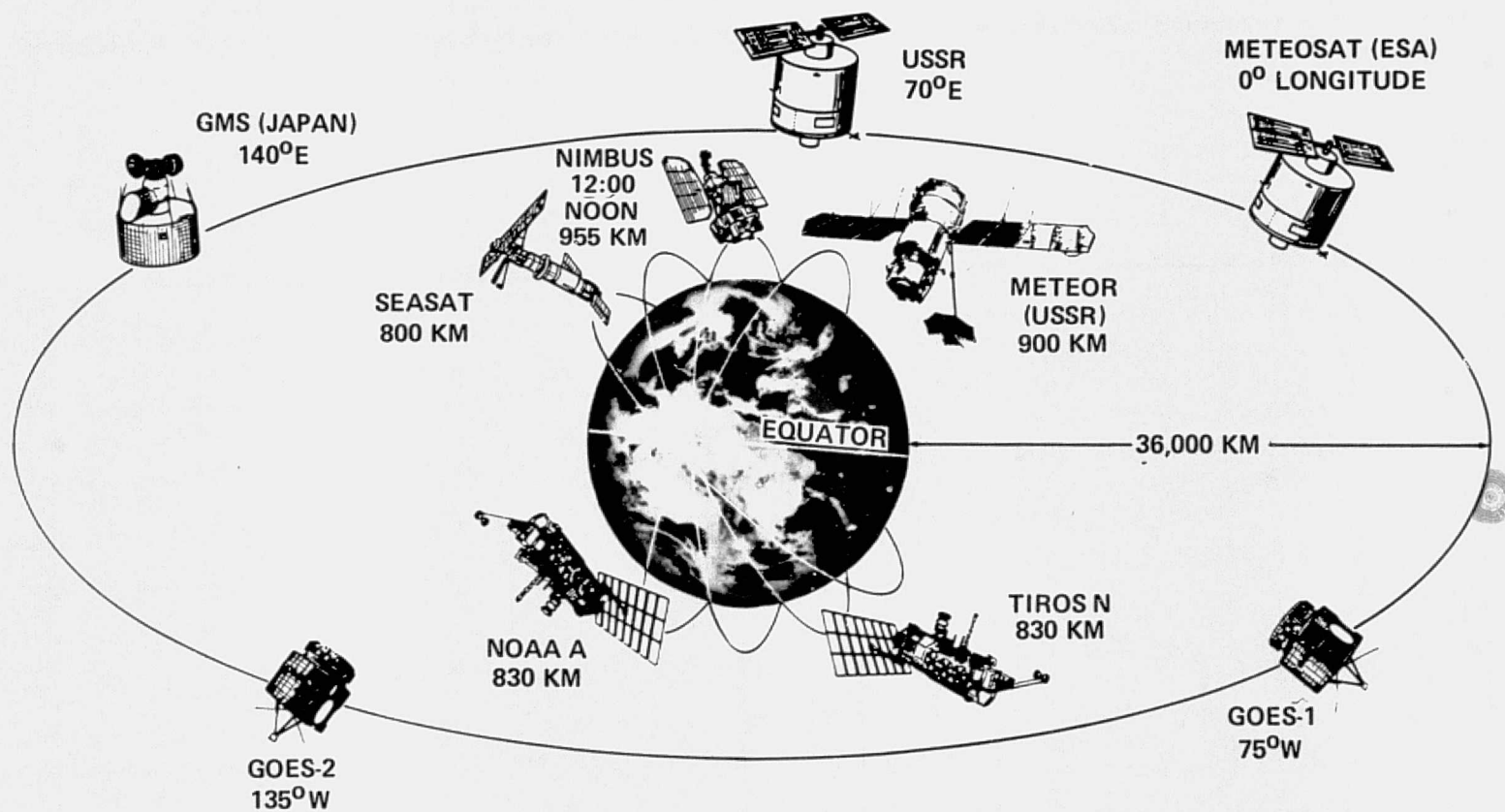


Figure 44. Weather Satellites to be in Orbit During the First GARP Global Experiment (FGGE) 1978-1979

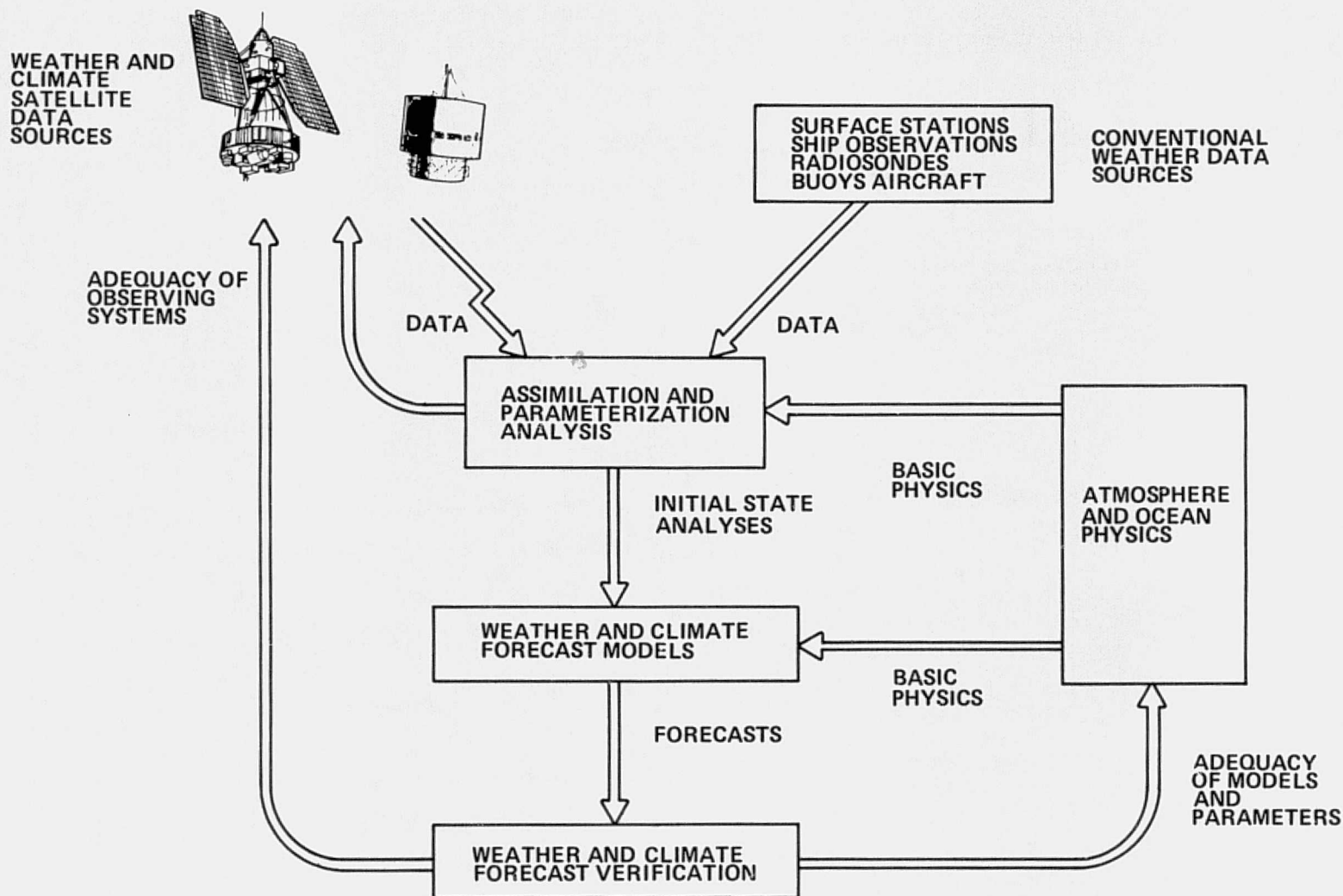


Figure 45. A Schematic of the Global Data Flow and Planned Data Utilization for FGGE Program

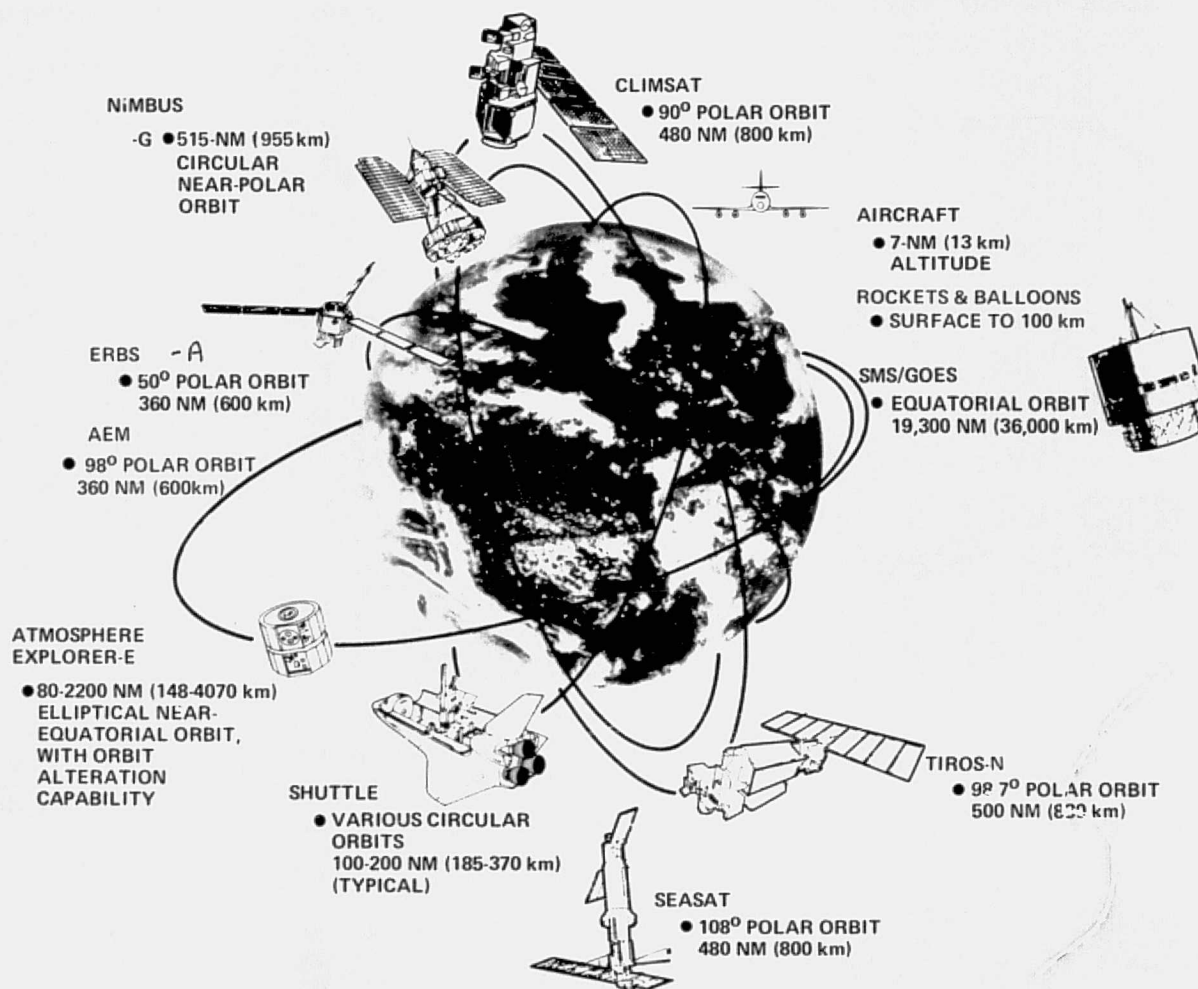


Figure 46. Proposed Weather Satellites and Supporting Research Systems for the U. S. Climate Program

Figure 47. Climatic Cause-and-Effect (Feedback) Linkages (Kellogg and Schneider, 1974)

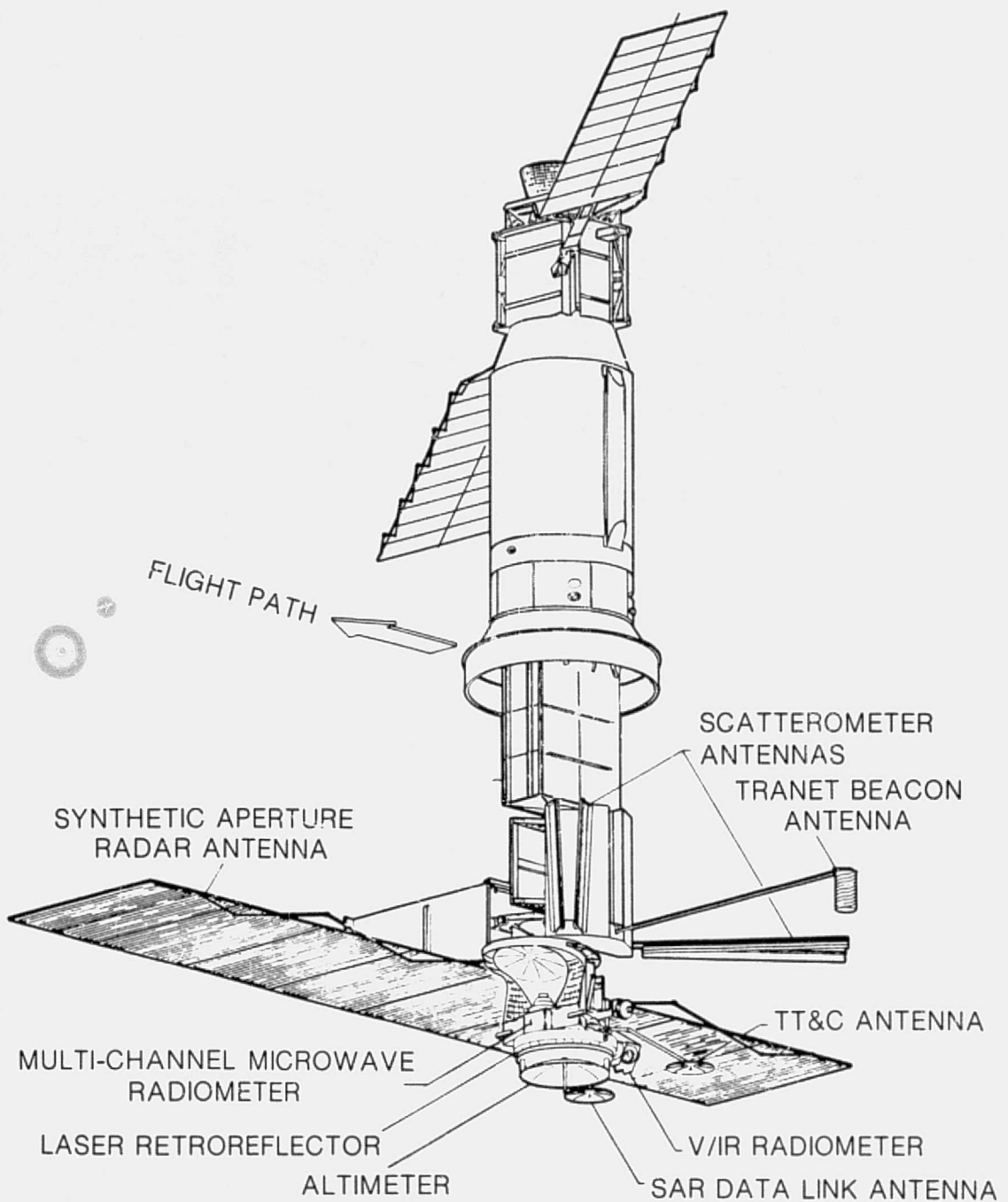


Figure 48. SEASAT-A with Associated Experiments

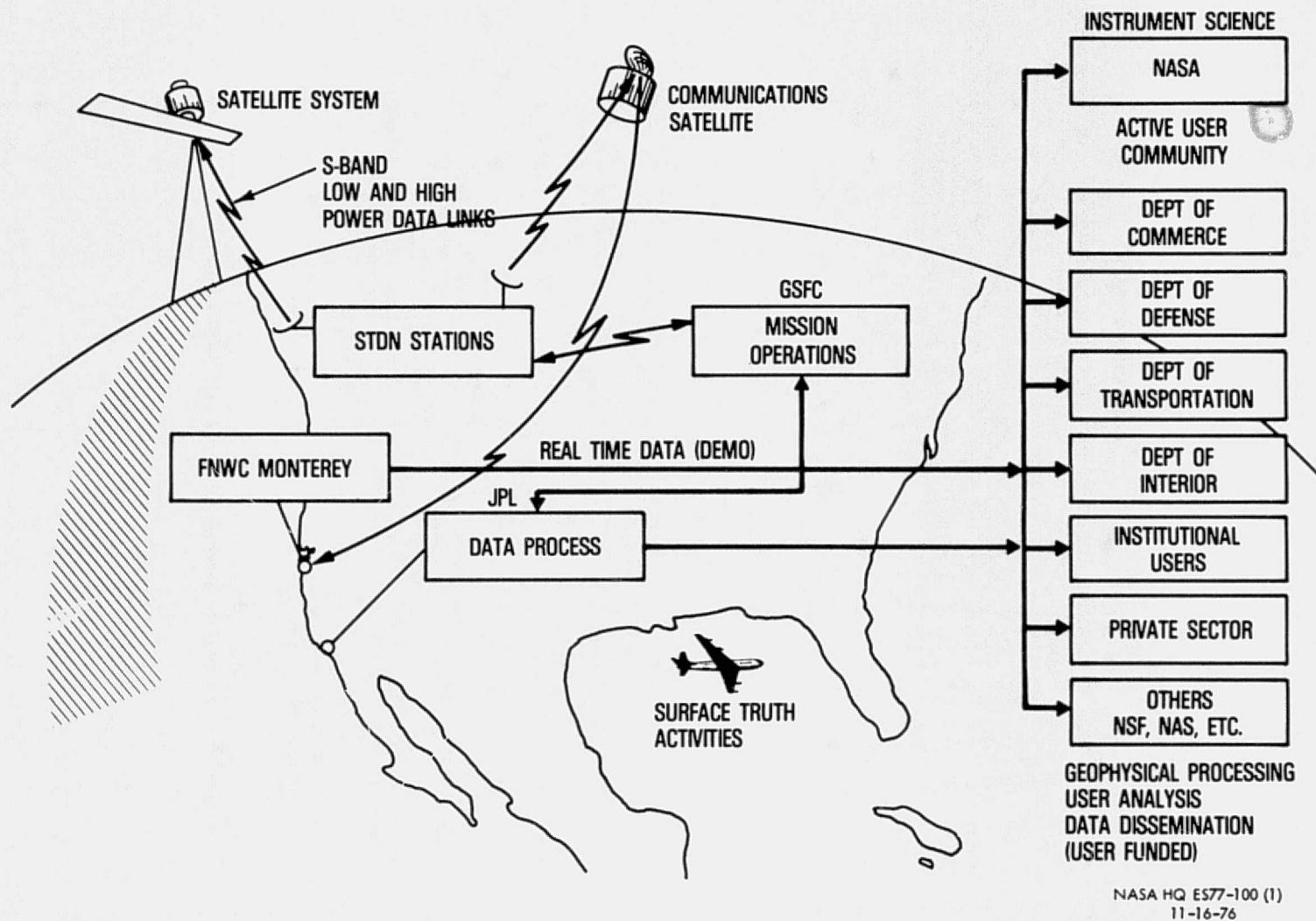


Figure 49. A Schematic of SEASAT-A Ocean Data Distribution Plan

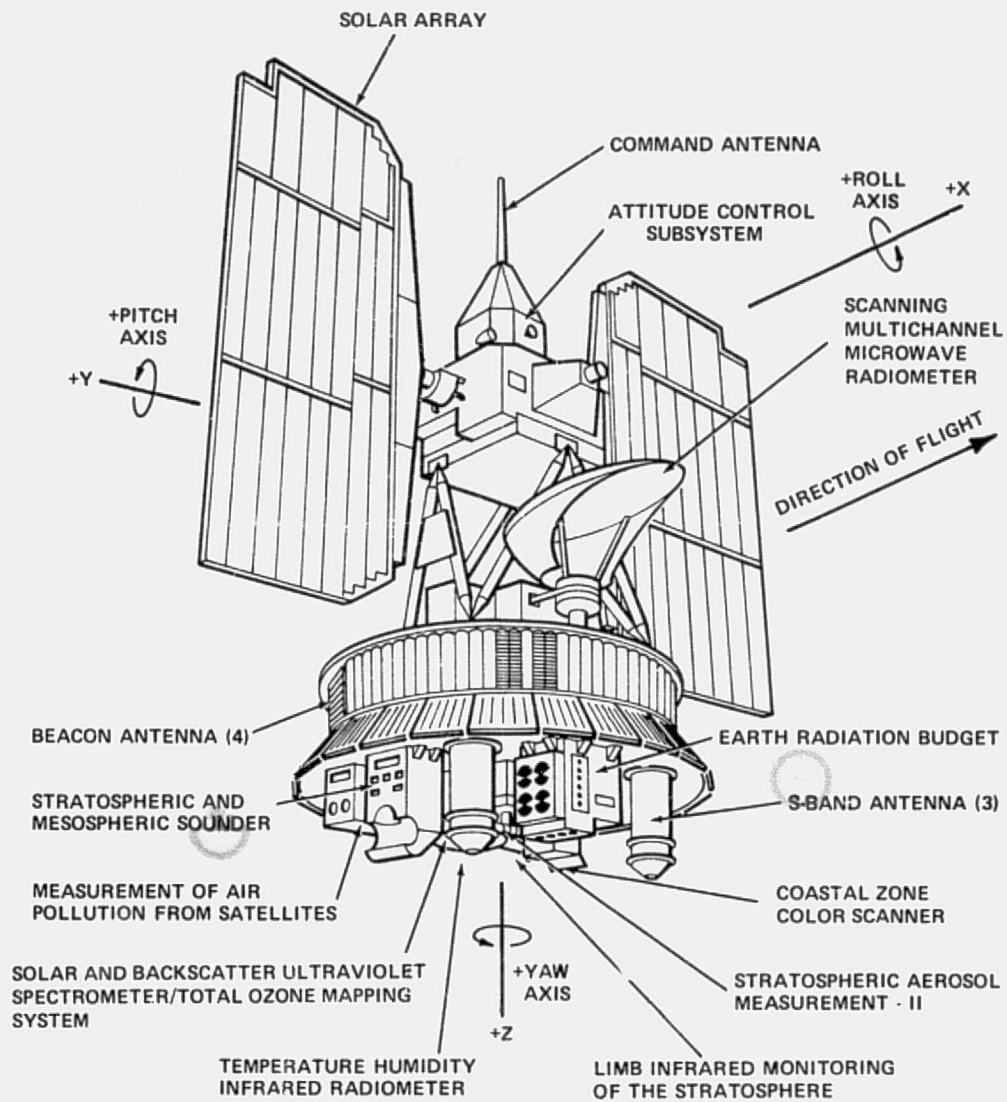


Figure 50. Nimbus-G with Associated Experiments

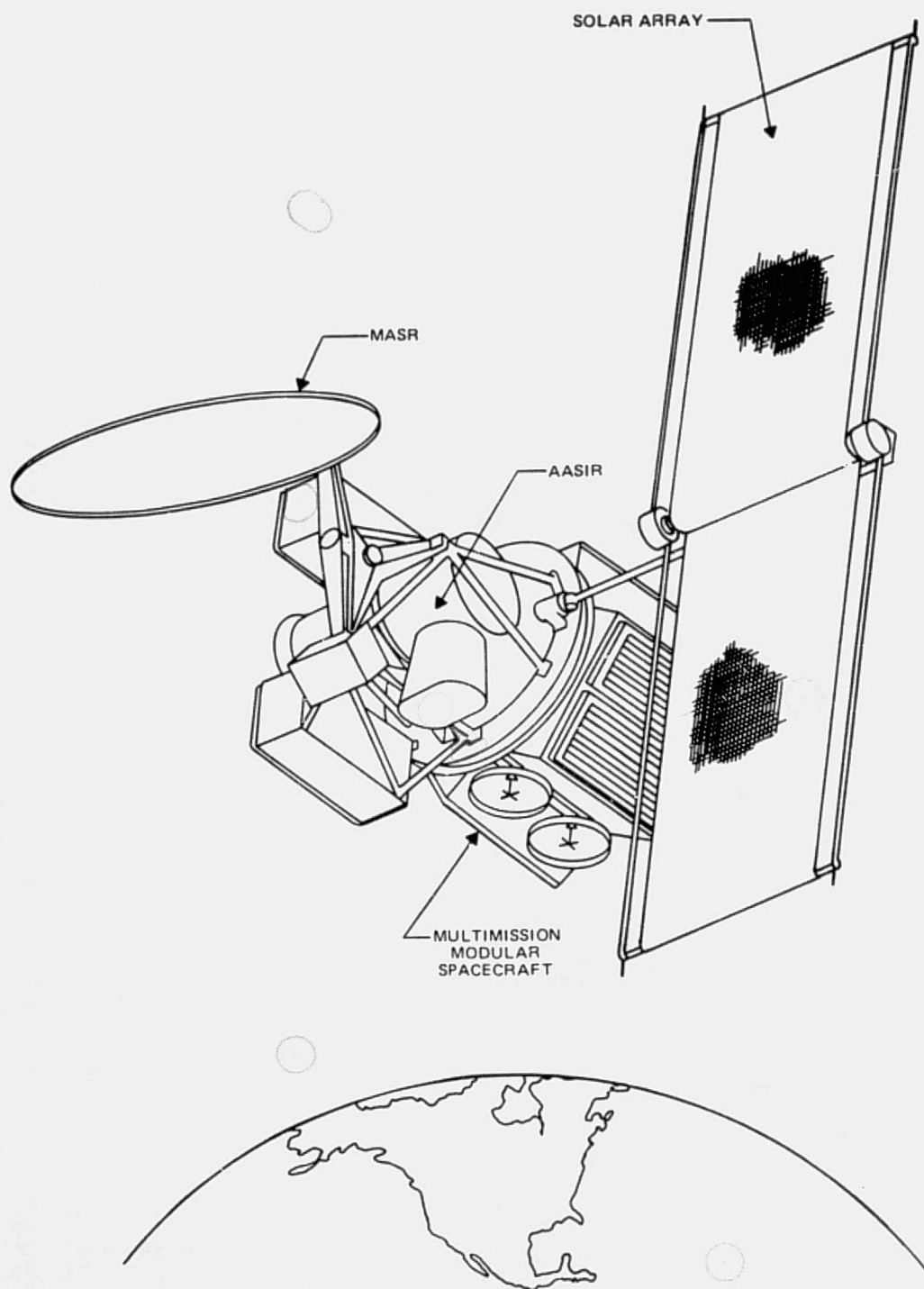


Figure 51. Conceptual STORMSAT Spacecraft with Associated Experiments

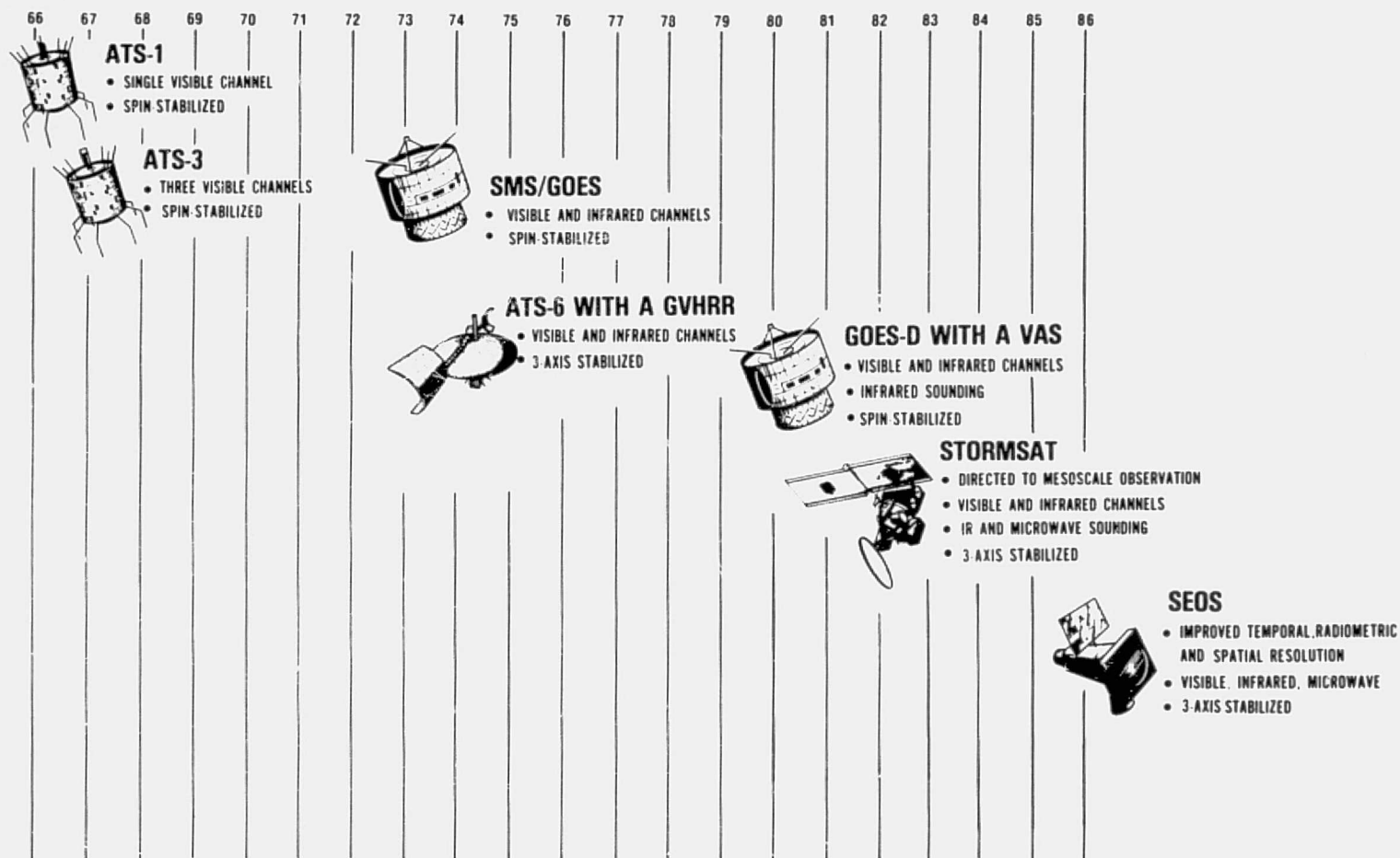
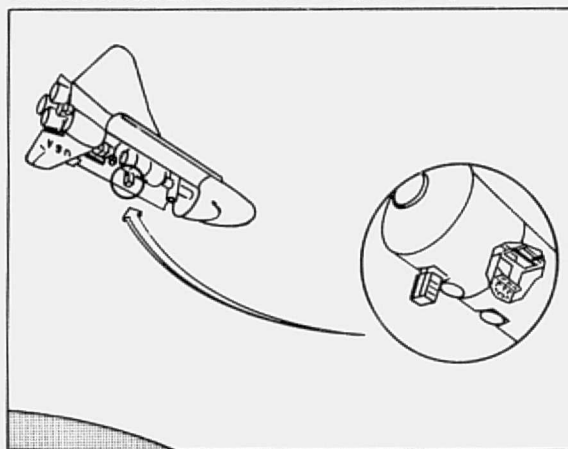


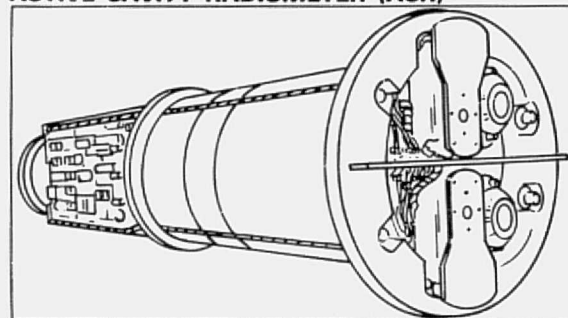
Figure 52. Chronological Development of Geostationary Meteorological Satellites Leading to the STORMSAT and Later SEOS Concept

MARK II INTERFEROMETER (ATOMS)



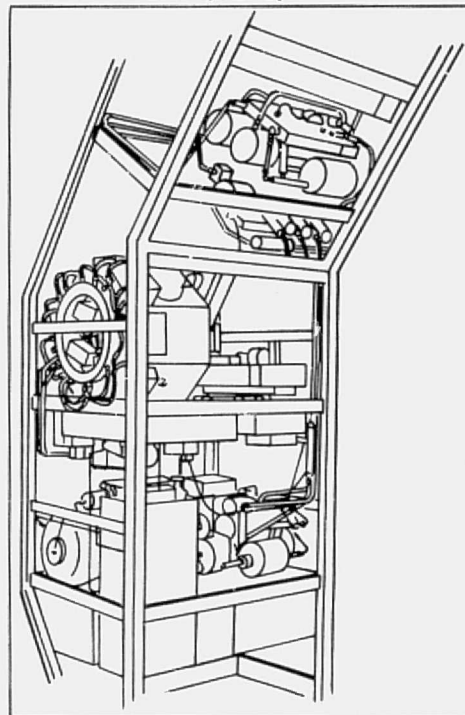
GLOBAL MEASUREMENTS OF MINOR GASES AND
POLLUTION IN THE STRATOSPHERE.

ACTIVE CAVITY RADIOMETER (ACR)



MEASURE THE SUN'S TOTAL RADIATION ARRIVING
AT THE EARTH.

ATMOSPHERIC CLOUD PHYSICS LABORATORY (ACPL)



STUDY CLOUD FORMATION PROCESSES
IN A NEAR-ZERO GRAVITY ENVIRONMENT.

Figure 53. Instrument Development Proposed for Shuttle-Spacelab Use